University of Strathclyde

Department of Naval Architecture, Ocean and Marine Engineering

Fracture Analysis in Marine Batteries by Peridynamic Theory

By

Hanlin Wang

A thesis submitted in fulfilment of the requirements for the degree of Doctor of Philosophy

Glasgow, U.K.

December, 2018

AUTHOR STATEMENT

This thesis is the result of the author's original research. It has been composed by the author and has not been previously submitted for examination which has led to the award of a degree.

Signed: Date:

ACKNOWLEDGEMENTS

I would like to show my greatest respect and gratitude to my supervisor, Dr. Erkan Oterkus, who patiently and meticulously teaches me the knowledge of peridynamic theory throughout my whole PhD study. With his help, I was able suit myself into research in a short time. He has provided me a great opportunities in sharing the ideas and problems with my colleagues but he also encourages me to build up the ability in self-learning and solving the problem by myself. He suggests me to have an optimistic altitude in normal life and be prudent and objective in the research study. Moreover, he also provides the platform, such as research conference and journals, to express my work to the world, which make great contributions to my professional development. I have benefited a lot from his suggestion and support.

I am also grateful to my parents, Sufeng Huo and Kai Wang, for their unconditional love and supports. As a self-funding international student, I not only can get the financial supports, but, more importantly, the psychological supports from them. They would like to share not only my achievements, but also my troubles and unhappiness. They also help me a lot in searching the employment information about possible future jobs. Just like my supervisor in the real life, I can get lots of guidance and skills so that I could take care myself well and fully concentrate on my studies.

I must show my respect to Selda Oterkus, who is also an expert on peridynamic theory. She has gave me some guidance in the study of peridynamic differential operatior.

I show my thanks to Selahattin Celik and Serkan Toros. They kindly shared their model which contributed to the construction of peridynamic model of SOFC electrode plate.

I need to show my thanks to my colleges and staffs in Dept. of Naval Architecture, Ocean and Marine Engineering for their collaborative, helpful supports, which has

produce a friendly research environment. I should also thank to the University of Strathclyde for the cooperative education program with Harbin Engineering University during my undergraduate study, which gives me the opportunity to join the PhD research programs overseas. Besides, the university has also provided various self-development training courses in the post-graduate study which contributes to my daily researches.

Last but not least, I acknowledge the anonymous reviewers of the journal papers and researchers in international conference. Some of their suggestions help me find out the errors and limitations in my study and some suggestions has point out the direction of possible future studies, which benefit a lot in my professional development.

“士不可以不弘毅，任重而道远。”

《论语·泰伯》

"The researcher must be breadth in mind and vigorous in endurance. His burden is heavy and his course is long."

《Taibo chapter, the Analects of Confucius》

ABSTRACT

Hybrid propulsion system (HPS) has become popular in marine industry due to increasingly strict emission control standards. Hence, as one component in the system, marine batteries become attractive in marine design. Solid Oxide Fuel Cells (SOFCs) and lithium ion battery are the most promising energy storage devices in the electric propulsion system or HPS. Since silicon particles expand around 400% in volume during lithation, the battery electrodes will experience large volumetric change during normal battery cycling. As a result, misdistribution of stress may form inside the battery electrode. Therefore, degradation and delamination may occur in the battery electrode after many cycling process of marine battery. Many efforts have been devoted to investigate the damage in the marine battery. Majority of numerical simulation methods nowadays are based on classical continuum mechanics (CCM). Partial differential equations (PDEs) are applied in CCM to describe the motion of material structure. However, due to the limitation of PDEs, most of numerical techniques based on this theory have difficulties in describing the motion of material body with discontinuous fields, such as cracks and kinks. In order to have a better understanding of the fracture mechanics in marine battery, the peridynamic theory is applied in this thesis. Different from classical theory, peridynamic theory has applied spatial integral equations to describe the motion of material structure. Therefore, it has great advantage on fracture analysis of material structure. Based on the nonlocality of peridynamic theory, the peridynamic differential operator is introduced and studied in this thesis. Peridynamic differential operator has transformed the PDE into spatial integral equation under the framework of peridynamic theory. Hence, the governing equations of thermomechanical deformation and the coupled diffusive-mechanical deformation can be reformed in the framework of peridynamic theory which benefit the relative numerical simulations.

In this thesis, the electrode models of SOFC and lithium ion battery in both two and three dimensions are selected. In order to validate the peridynamic theory, some results are compared with CCM. They have shown good agreement with each other. In the fracture analysis of SOFC, we have found out that fracture formation and evolution depend on the strength of interactions between electrode and electrolyte particles. For weak connection, the cracks will propagate along the interface of electrode and electrolyte. For uniform and strong connection, the cracks will start to propagate at regions with high geometrical singularity, such as pores or sharp corner regions. High hydrostatic stress is also located in these regions. In the fracture analysis of lithium ion battery, we have found out that facture formation and evolution depend on the hydrostatic stress and material properties. High hydrostatic stress generally reflects on high bond stretch value. Once the bond stretch value has exceed the critical value, cracks may form and propagate. Lithiated silicon, on the other hand, has decreased the critical bond stretch value. Hence, in some situations, crack propagation may not always be led by hydrostatic stress. Besides, the high hydrostatic stress will also increase the lithium ion concentration.

Finally, peridynamic theory has shown excellent performance in the numerical estimation of damage formation and evolution in the marine batteries without pre-defined crack path or cohesive element as compared with classical techniques. It has provided an efficient and reliable tool in the design, manufacture, failure detection and life prediction of the marine battery in the real life.

TABLE OF CONTENTS

LIST OF FIGURES

LIST OF TABLES

ABBREVIATIONS

Al	Aluminium
AFC	Alkaline fuel cell
BEM	Boundary element method
CCM	Classical continuum mechanics
Co	Cobalt
CZM	Cohesive zone method
DMFC	Direct methanol
e^-	Electron
ECA	Emission control area
FDM	Finite difference method
FEM	Finite element method
FVM	Finite volume method
Ge	Germanium
H^+	Hydrogen ion
H_2	Hydrogen
H_2O	Water
HPS	Hybrid propulsion system

IMO	International Maritime Organization
$LaMnO_3$	Lanthanum manganite
LEFM	Linear elastic fracture mechanics
$Li_{15}Si_4$	Fully lithiated silicon
LiC_6	Lithiated graphite
Li_xSi	Partially lithiated silicon
LSCF	Lanthanum strontium cobalt ferrite
LSM	Lanthanum strontium manganite
MCFC	Molten carbonate fuel cell
Mn	Manganese
Ni	Nickle
NiO	Oxidised nickel
NO_x	Nitrogen oxides
O_2	Oxygen
ODE	Ordinary differential equation
PAFC	Phosphoric acid fuel cell
PCFC	Protonic ceramic fuel cell
PD	Peridynamic theory
PDE	Partial differential equation

PDO	Peridynamic differential operator
PEMFC	Proton-exchange membrane fuel cell
SAFC	Sulfuric acid fuel cell
Sb	Antimony
Si	Silicon
Sn	Tin
SOFC	Solid oxide fuel cell
SO_x	Sulphur oxides
TEM	Transmission electron microscope
TPB	Triple phase boundary
VCCT	Virtual crack closure technique
XFEM	Extended finite element method
YSZ	Yttria-stabilized zirconia

NOMENCLATURE

a_n^p	Elements of peridynamic unkown matrix
A_n^q	Elements of peridynamic shape matrix
$b(\vec{x},t)$	Body force density of material point $\vec{x}$ at time t
b_n^p	Elements of peridynamic known matrix
c	Bond constant
E	Elastic (Young's) Modulus
$\vec{\mathrm{f}}$	Pairwise bond force
$f(x)$	Physical quantities depended on certain problem
G_C	Critical Energy release rate
g_N^P	Peridynamic function
h	Plate thickness
H_x	Horizon of material point $\vec{x}$
K	Fracture toughness
R	Reminder terms
s	Stretch
s_c	Critical bond stretch

scf	Surface correction factor
t	Time
T_{avg}	Average temperature of material points i and j
T_i	Temperature of material point i
$\vec{u}(\vec{x},t);\ \vec{u}$	Displacement of material point $\vec{x}$ at time t
$\vec{u}'(\vec{x}',t);\ \vec{u}'$	Displacement of material point $\vec{x}'$ at time t
$\ddot{\vec{u}}_i^n$	Acceleration of material point i at n^{th} time step
$\dot{\vec{u}}_i^n$	Velocity of material point i at n^{th} time step
$\dot{\vec{u}}_i^{n+1}$	Velocity of material point i at $(n+1)^{th}$ time step
$\vec{u}_i^n$	Displacement of material point i at n^{th} time step
$\vec{u}_i^{n+1}$	Displacement of material point i at $(n+1)^{th}$ time step
V_C	Volume correction factor
V_j	Volume of neighbour point j
W_{CCM}	Strain energy density calculated by classical continuum mechanics
W_{PD}	Strain energy density calculated by peridynamic theory

$\vec{x}$	Location vector of material point *x* under initial configuration
$\vec{x}'$	Location vector of material point *x'* under initial configuration
$\vec{y}$	Location vector of material point *y* after deformation
$\vec{y}'$	Location vector of material point *y'* after deformation
α	Coefficient of thermal expansion
δ	Horizon size
Δt	Time step size
ε	Strain
$\vec{\eta}$	Relative displacement of bond
μ	Failure parameter
ν	Poisson's ratio
ξ	Initial bond length
ρ	Density
σ	Cauchy stress
$\tilde{\sigma}$, σ_{hyd}	Hydrostatic stress
σ_0	First Piola-Kirchoff stress

σ_{dev}	Deviatoric stress
σ_{VM}	Von-Mises stress
ω	Scalar micro-potential energy
ω_{np}	Weight function

1 INTRODUCTION

This chapter, in general, gives the background and layout of this PhD thesis and it is divided by four sections. The basic knowledge about the current marine environment and information about marine batteries are provided in Section 1.1. Section 1.2 shows the motivation of my PhD research and the major objectives of this thesis are listed in Section 1.3. Finally, the structural arrangement of the whole thesis is shown in Section 1.4.

1.1 Background and motivation

Fossil fuel is widely applied in marine industry since the invention of the inner combustion engine at the beginning of the last century. With the high power-rate ratios, the engines have various applications in vessels and marine equipment such as cruise ships, tugboats, icebreakers, yachts and oil rigs. During the burning of fossil fuel, large amount of marine waste gases are emitted into environment. Hence, the emission control in marine industry has become a concerning issue in environmental protection and it is under the restriction of IMO regulations. According to Marpol Annex VI requirement, emission of nitrogen oxides (NO_x) should reduce nearly 80% after 2016 as compared with that in 2000. On the other hand, emission of sulfur oxides (SO_x) in 2020 is enforced to remain below 10% of that in 2012, as shown in Fig. 1.1[1]. The emission standard becomes increasingly strict especially in the emission control area (ECA), such as costal region of North America and part of North Sea.

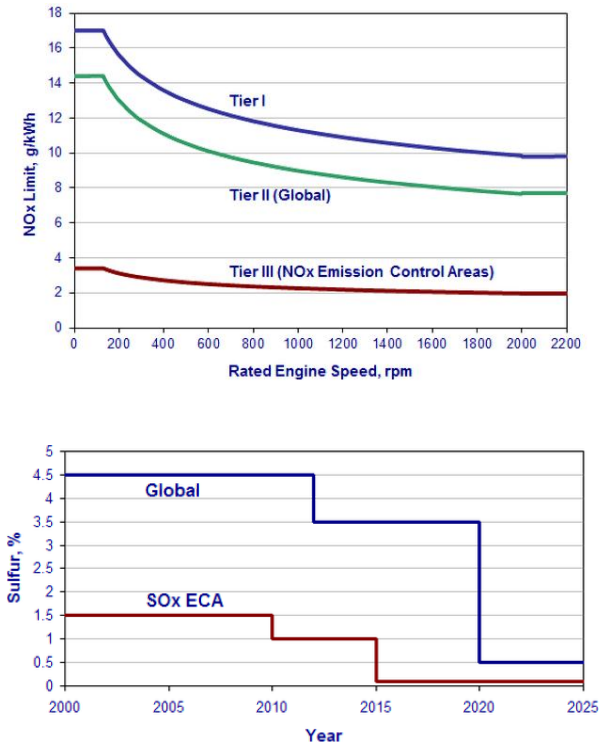

Figure 1.1. Marpol Annex VI requirement about NO_x and SO_x. [1]

As a result, HPS has become more popular in marine industry as one of the solutions in emission reduction [2]. HPS is composed of two or more energy sources (main engine, auxiliary engines, battery, etc.), converter, electric motor, gearbox and propeller, as shown in Fig.1.2. With the advantages of low fuel consumption, low emission, safe and reliable propulsion, high manoeuvrability and high redundancy, HPS has a better performance than the traditional propulsion system in efficiency especially when dealing with various marine operating conditions.

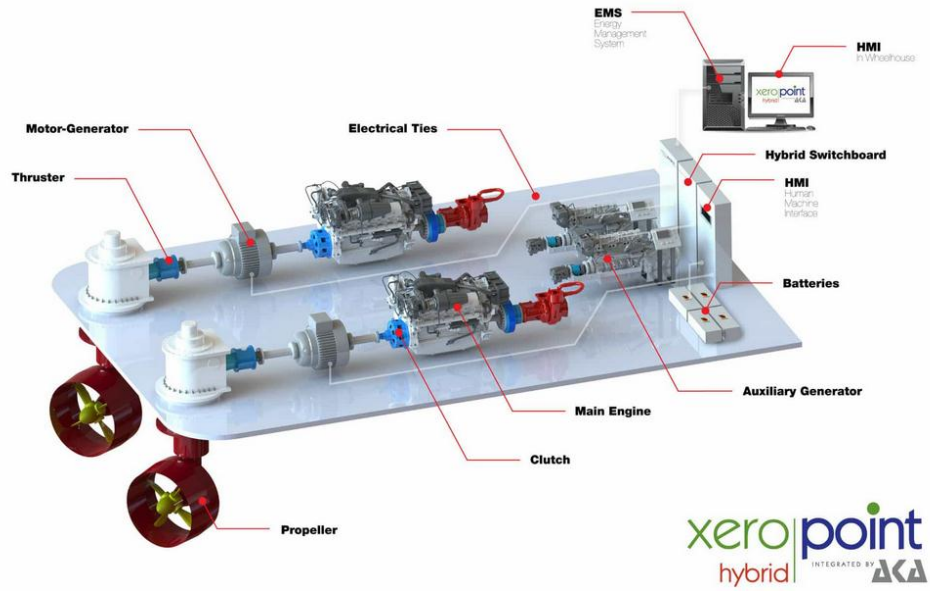

Figure 1.2. Hybrid Propulsion System [3]

Marine batteries, therefore, as one of the components in HPS are under plenty investigations in order to optimise the battery performance and reduce the price [2]. Based on battery applications, marine batteries could be categorised into starting batteries and deep cycle batteries [4]. Starting battery is usually designed to start the marine engine with relatively high power output in a short period. Hence, starting battery is usually composed of series of thin electrode plates to increase electrochemical reaction interface. However, thin electrodes do not have strong mechanical stiffness for high impact operating environment and do not support deep cycle charging. Deep-cycle batteries (or reserve batteries), on the other hand, do not have strong energy output like starting batteries, but have relative large capacity which could discharge for a long time [4], [5]. Therefore, deep-cycle marine batteries are usually applied as the battery banks in auxiliary systems and hybrid propulsion systems. Based on battery chemistry, marine batteries can be categorised in several types. Detailed advantages and disadvantages are shown in Table 1.1. Apart from cost, marine lithium-ion battery is one of the most promising power storage systems due to its high energy to weight ratio, high energy density, low self-discharge and long life cycle [5], [6].

Table 1.1. Comparison of Marine batteries [7]

Battery type	Advantages	Disadvantages
Lead-acid	Low cost Low self-discharge (2-5% per month)	Short life cycle (1200~1800 cycles) Cycle life affected by depth of charge Low energy density (about 40 Wh/kg)
Nickel-based	Can be fully charged (3000 cycles) Higher energy density (50-80 Wh/kg)	High cost, 10 times of lead acid battery High self-discharge (10% per month)
Lithium-ion	High energy density (80~190 Wh/kg) Very high efficiency (90~100%) Low self-discharge (1~3% per month)	Very high cost ($900~1300/kWh) Life cycle severely shorten by deep discharge Require special overcharge protection circuit
Sodium	High efficiency (85~92%)	Be heated in stand-by mode at 325 ℃
Sulphur (NaS)	High energy density(100 Wh/kg) No degradation of deep charge No self-discharge	
Flow batery	Independent energy and power ratings Long service life (10000 cycles) No degradation for deep charge Negligible self-discharge	Medium energy density (40~70 Wh/kg)

The performance of lithium-ion battery mainly depends on the material properties of electrodes and electrolyte. The selection of electrode material components are based on the operating environment of the lithium-ion batteries. In view of cathode

material, Cobalt (Co) compound and Nickel (Ni) compound are highly electrical stable but low thermal stable and toxic. Manganese (Mn) compound has relatively high electrical capacity and high thermal stability but low cycle performance [8]. Silicon (Si) is found to be an excellent cathode material due to its high theoretical capacity (3600 $mAHg^{-1}$). However, lithiated silicon compound formed during lithiation process causes up to about 400% volume expansion [9]. Therefore, frequent cycling will cause stress misdistribution and degradation, delamination of the battery may occur which have negative influence on battery performance.

On the other hand, SOFC is another type of powerful storage equipment with high energy conversion efficiency, high fuel flexibility, low emission and low material cost. As a common fuel cell type, SOFC is composed of solid electrode and electrolyte layers. Ni, Yttria Stabilized Zirconia (YSZ) and perovskite-based $LaMnO_3$ are the most commonly used materials for anode, electrolyte and cathode, respectively [10], [11]. Typically, the electrodes and electrolyte are made into layers and stacked on each other in a certain sequence. In order to increase the efficiency of electrochemical reaction, electrolyte material is added inside the electrode layers [12]. Electrochemical reactions (oxidation of the hydrogen) that are required for generation of the free electrons occur through the Triple Phase Boundaries (TPBs) which are the intersection lines of the metal/non-metal grains and fuel filled pores. The reaction rate and the generated power in the anode and cathode depend on the active TPBs which can be controlled by the amount of the compositions, grain size and porosity ratio. The reactions taking place in a hydrogen fuelled SOFC are given below:

$2H_2 \Rightarrow 4H^+ + 4e^-$ (Anode region; oxidation reaction)

$O_2 + 4H^+ + 4e^- \Rightarrow 2H_2O$ (Cathode region; reduction reaction)

$2H_2 + O_2 \Rightarrow 2H_2O$ (the redox reaction)

In marine environment, SOFC does not only requires hydrogen, but also carbon oxides and some hydrocarbon substance which can be obtained from marine waste gases and marine fuel oil. Fossil fuels like gasoline, natural gas, coal gas and liquid petroleum gas could also be regarded as possible fuel of SOFC [13]. The redox reaction in SOFC generates large amount of heat which rises the operating temperature up to around 800 ℃ [14]. High temperature does not only provides a suitable environment for ion transportation through ceramic electrolyte, but also catalyses side reactions in SOFC. Impurities in marine fuels like hydrogen sulphide, chloride, alkali compounds and tars may react with part of the electrode and electrolyte materials, and form stable and inert by-product on the TPB. This will lead to performance degradation of SOFC and harmful waste gas emission [13], [15]–[17]. Hence, gas purifying equipment is mandatorily installed before SOFC sections [13]. Under large thermal loading, the electrode and electrolyte layers will deform. Since the electrolyte material is added inside the electrode layer, the mechanical properties in each layer are not homogenous. Besides, due to different material properties of electrodes and electrolyte, differences in mechanical deformation are observed at different parts of SOFC [12]. Hence, degradation of SOFC may occur which may cause negative influence on fuel cell performance and even failure.

Overall, the performance of marine batteries strongly relies on the material properties and structural integrity of electrodes and electrolyte. Generally, the electrochemical reaction (redox reaction) inside batteries will increase operating temperature dramatically. Under this working environment, degradation may occur in the electrodes and electrolyte. As a result, unstable voltage, low capacity and cell failure may eventually occur which lead to performance loss of the batteries. Hence, the fracture and fatigue analysis is important in the life span prediction and cell performance optimisation of marine batteries [18]. CCM is a widely used methodology in solid mechanics and it has provided a good framework for finite element method (FEM). However, PDEs in CCM formulation may encounter difficulties in modelling fracture and failure since PDEs do not have definitions over

discontinuous domains. Therefore, standard FEM can not describe the damage formation and propagation accurately. There are various techniques proposed for failure prediction such as FEM by remeshing, virtual crack closure technique (VCCT), cohesive zone model (CZM) and extended finite element method (XFEM). Although these techniques are suitable for the analysis of certain problems, they have several limitations such as requirement of pre-existing damage, mesh dependency, etc. Therefore, a new numerical analysis method, called peridynamics, is introduced by Silling in 2000 [19], which can be a suitable alternative to evaluate the formation and evolution of material fracture and failure. Peridynamic theory (PD) is based on integro-differential equations which are valid along discontinuous domains without any pre-defined condition and criteria. Moreover, pre-existing damage is not required and the crack path is not affected by the discretisation. Detailed information about PD will be illustrated in Chapter 3.

1.2 Objectives of research

Four major objectives are under discussion in this thesis:

- Study the framework of peridynamic differential operator (PDO) in 3 dimensions. PDO has applied an integral equation as a replacement of differential equation which could simplify the numerical simulation in fracture analysis. It has also provided a framework for numerical simulation in mechanical, thermal and coupled field analysis.
- Build up a two-dimensional model based on PD to investigate the fracture formation and evolution in SOFC electrode plate. Since the mechanical stiffness between electrode particles and electrolyte particles is unknown, different stiffness situations are under investigation.
- Build up a two-dimensional model based on PD to investigate the fracture evolution in pre-damaged lithium-ion electrode plate. Based on several damage cases, a series of simulations are provided to illustrate the crack evolution under consideration.

- Build up a three-dimensional model based on PD for the fracture analysis of special structures in lithium ion batteries such as spherical energy storage particles and silicon nanowires.

1.3 Structure of the thesis

This thesis is constructed into following chapters:

- Chapter 1: Some information about marine batteries is provided in this chapter, which include the type of batteries, the fracture in several batteries and methods that are applied to analyse the fracture of batteries. Besides, the main objective and motivation of these researches and the whole arrangement of thesis are mentioned in this chapter.
- Chapter 2: Several numerical implementation methods that are commonly applied today in fracture analysis are under discussion in this chapter. These numerical implementation methods are based on CCM and the advantages and limitations of them will also be provided in this chapter.
- Chapter 3: Basic information about bond-based peridynamics is produced. The bond-based peridynamics is the theoretical basis of all of the simulations in this thesis.
- Chapter 4: The concept of PDO is introduced. PDO will replace a PDE with an integral equation. It has simplified the numerical simulation of fracture analysis dramatically. In this chapter, the 3 dimensional framework based on the PDO will be constructed and the relavant convergence studies are applied to validate the reliability of PDO.
- Chapter 5: In this chapter, a single charging process for two-dimensional SOFC electrode plate is simulated. High thermal loading is applied on the plate and the fracture situations of different mechanical stiffness are under discussion.
- Chapter 6: In this chapter, models of two-dimensional lithium-ion electrode plate with pre-existing cracks are constructed. Under single lithiation process, various pre-damaged situations with pressure gradient effect are under discussion.

- Chapter 7: In this chapter, model of three-dimensional lithium-ion electrode structures are constructed. These models are pre-damaged by a penny shape crack. The evolution of hydrostatic stress and lithium-ion concentration inside these anode structures are under investigation.
- Chapter 8: Review of the whole thesis (objectives, summaries, contributions). The discussion of future works and remarks are also provided.

1.4 Summary

Marine batteries have played important roles in HPS. Since the battery cost is high and the battery life span is short in general, the fracture and failure analysis is of vital importance in life span prediction and battery optimisation. Since fracture and failure analysis may be costly in real experiments, most of the researches rely on the numerical simulations. Traditional numerical simulation methods are based on CCM, which has limitations in simulation of non-continuous problems such as damage and failure. Hence, PD is introduced in this thesis as an alternative approach. PD applies integral equations which has overcame the limitation of non-continuous problems. In this thesis, two most promising marine batteries (lithium-ion and SOFC) are under investigation. The major objective is to build up new numerical simulation frameworks, for the failure and fracture analysis of marine batteries which will be helpful in battery optimisation and life span prediction.

2 LITERATURE REVIEW

2.1 Introduction

The aim of this chapter is to make a summary of researches and experiments in fracture and failure analysis of batteries in history. From the historical overview, the basic information of fracture analysis method, fracture analysis implementations of SOFCs and lithium-ion batteries are discussed in this chapter. The advantages and limitations of numerical simulation methods are provided and the comparison between these methods and PD will also be stated here. This chapter is composed of four parts. The first part states the introduction and main purpose of this chapter. The discussions of traditional numerical methods are listed in Section 2.2. The experiments and simulations that are applied in fracture analysis of SOFC in the history are provided in Section 2.3. The experiments and simulations that are applied in fracture analysis of lithium-ion battery in the history are stated in Section 2.4.

2.2 Historical overview of numerical methods in fracture analysis

Continuum mechanics is a branch of solid mechanics which focuses on mechanical motions of structures under external loading. The deformation, stress and failure of structures are affected by external force, thermal loading, phase change and electrical loading [20]. However, due to the limited computing power in the past, researchers can only obtain analytical solutions for simple geometry and loading conditions [21], [22]. In reality, most of the solid materials are heterogeneous and anisotropic which can not be described simply by analytical solution. In recent years, due to the rapid development in computer technology, numerical analysis of solid mechanics becomes more efficient and accurate. Various numerical methods, such as FEM and boundary element method (BEM), are widely utilised for the solid mechanics analysis.

2.2.1 Finite element method

Finite element method (FEM), as a numerical analysis method, is usually applied to deal with problems with complex geometry and boundaries. The capability of FEM is not only limited to mechanical stress analysis and can be used for other physical fields such as thermal conduction and diffusion [23]. By discretizing the whole geometry into finite number of small elements, the whole structure can be represented and simplified. The behavior of the solid body and structure in terms of displacement, temperature, concentration and pressure are embodied in the nodes by which the elements are connected [24].

FEM is currently the most commonly applied analysis tool. Since a solid body can be expressed by elements in various sizes during the discretization process, FEM can deal with problems with irregular geometries. FEM also have various applications on fracture mechanics based on classical continuum mechanics (CCM) framework. In CCM, the equation of motion is defined by a PDE. However, PDE does not have definition over discontinuous geometries such as cracks. In CCM, there are several methods widely applied for fracture analysis such as stress intensity factor and strain energy release rate [25]. Theoretically, the stress value around crack tip is expressed as $\sigma = K/\sqrt{2\pi r}$. K is the stress intensity factor and r is the distance to the crack tip. Once the stress reaches critical value, crack will propagate. Therefore, in order to increase the accuracy of analysis, mesh around crack tip regions should be refined as much as possible to capture the stress singularity. Although this increases the accuracy, higher computing performance and longer computing time are required. Besides, this expression of stress is inappropriate, since the stress will reach infinite as r tends to 0. Even though small loading is applied on the structure, the stress at the crack tip will still reach infinity, which is impractical in the real world. Moreover, stress intensity factor approach can describe the propagation of a crack, but can not explain the formation of a crack.

Inglis has provided linear elastic solution for stresses around elliptical shape crack tip [26]. He believes that the crack tips will deform and be flattened under loading while stress will increase to infinity. However, there is no such kind of material can resist infinite stress without being damaged. Therefore, Griffith (1921) and Irwin (1957) have introduced the stain energy release rate as the criteria of material fracture [27], [28]. They believe that crack will propagate when the amount of decreased elastic energy is larger than the increased newly formed surface energy. Otherwise, crack should not propagate [29]. The Griffith fracture criterion is introduced for homogeneous, brittle and elastic materials. However, it will lose accuracy when dealing with ductile materials. Hence, an alternative method, J-integral, was proposed by J. Rice to estimate the strain energy release rate for materials with elastic-plastic behavior [30]. FEM has also applied the strain energy release rate as a criterion in determining fracture evolution. However, this method still can not explain the formation of cracks. Besides, once the crack propagates, the entire boundary should change. Madenci and Oterkus have emphasized the importance of remeshing process in modelling crack propagation by FEM [31]. Although there are various remeshing techniques available for FEM, such as node relaxation and convective/stationary formulation [32], the numerical simulation becomes complex and more computing time is required.

Since classical FEM has difficulties in modelling moving boundary problem, XFEM was introduced to increase the accuracy of these simulations. XFEM has applied additional enrichment term based on partition of unity concept [33] to the classical FEM governing equation:

$$u^h(x) = \sum_{i \in I} N_i(x) u_i + \sum_{i \in I^*} M_i(x) a_i \tag{2.1}$$

The second term in Eq. (2.1) is the enrichment function of XFEM which has achieved the approximation of singularities, kinks and jumps under the FEM domain [34]. Hence, mesh of material structure of XFEM does not have to align with discontinuity boundary. In XFEM, the discontinuous boundary can be located at

element interiors. Therefore, remeshing process in fracture analysis by FEM can be avoided. Belytschko et al. believe that XFEM can also be applied for dynamic fracture analysis [35]. The level-set method was introduced to describe the cracks and the loss of hyperbolicity criterion is applied in fracture prediction. However, level-set method can not detect the branching phenomenon in crack propagation. Hence, the XFEM can not provide accurate result in fracture evolution. Besides, the enrichment term of XFEM increases the complexity of simulation.

2.2.2 Boundary element method

BEM, or boundary integral method, was introduced as an alternative method in many engineering applications. The theory was founded by Betti, Somigliana and Lauricella [36], and the numerical implementation was developed by Rizzo [37]. Main difference between BEM and FEM lies on the discretization of material body. BEM applies the boundary integral method to describe the boundary state. Therefore, the discretization of interior body is not necessary [24]. As a result, BEM reduces the problem by one order. Only boundary lines and surfaces are discretized in 2D and 3D problems, respectively. It is a simplified analysis approach which saves large amount of computing resources. Besides, the resolution of stress and displacement of interior material body is improved which leads to an improvement of efficiency.

Although BEM is suitable for material structure with continuous and linear elastic properties [38], it has limitation for fracture mechanics analysis. The pre-existing damage can be regarded as a boundary, but for a newly-formed damage, interior of the material structure must be under consideration and it will bring difficulties for BEM. Moreover, BEM has a low accuracy in analyzing material structures with high boundary surface to volume ratio, such as shell and thin plate structure [38], [39]. It is because of the close distance of nodes on either side of the structure. In recent years, some hybrid BEM/FEM approaches are introduced to solve plastic and nonlinear problem [40]–[43].

2.2.3 Cohesive Zone Method

CZM is one of the commonly applied methods in fracture analysis based on CCM. The origin of CZM goes back to Barenblatt [44], [45] and Dugdale's [46] works. From Barenblatt's view, the upper and lower crack surface is held by molecular cohesive forces located at the crack tip region. Dugdale regards the molecular cohesive forces having a constant value of yield stress, which is the fundamental assumption of Dugdale's strip yield model. According to the application of CZM nowadays, a narrow-band with zero thickness is located in front of crack tip to represent fracture process zone. The cohesive traction based on various cohesive laws [47] in fracture process zone links the upper and lower crack surfaces [48]. As the separation of the crack surfaces take place, the magnitude of traction force will follow a certain traction law and eventually vanish when new crack surface forms.

The cohesive traction in the fracture process zone has solved the singularity problem successfully under the scheme of FEM by introducing an interface element between two elements. However, it will also bring some other problems. Since the interface cohesive element lies between elements, the crack propagation is strongly mesh dependent and the accuracy of the results will also rely on the refinement of mesh. Moreover, it is difficult to predict the cracks which propagate through elements and branching cracks [48]. Xu and Needleman have developed a FEM/CZM model [49]. They have aligned the interface cohesive element with all the element boundaries and therefore, cracks can automatically form and propagate. However, the total stiffness of the whole structure may reduce even in undeformed state and this will lead to the distortion of elastic properties of this material structure [50]. Besides, the insertion of large amount of cohesive surface element will increase the complexity of the structure dramatically and higher computing performance is required.

2.2.4 Peridynamic Theory

As mentioned earlier, FEM, BEM and CZM have certain limitations in fracture analysis, because they are based on CCM. In CCM, a PDE is applied as the equation

of motion to describe the mechanical behavior of material points. However, PDE is valid in continuous domain only and it does not have definition over kinks, cracks and damages which have discontinuous property. Hence, Silling have introduced an alternative numerical method, named peridynamic theory, to solid mechanics especially fracture analysis [19]. PD has applied an integral equation as the equation of motion, hence the continuity of material structure does not have any influence to the numerical model [31]. PD uses the "bond" connection between material points to describe the material fracture and it does not need additional criteria for the definition of damage. Besides, it can also capture the detailed information about crack initiation and propagation such as crack propagation speed and crack branching. PD has various applications on multiple physical fields such as heat conduction, diffusion and coupled field analysis [18], [51]–[54]. Although peridynamic theory is efficient in predicting the crack formation and evolution, it does not shows better efficiency in the analysis without considering damage and failure as compare with classical theories. Currently, for bond-based peridynamic theory, uniform discretization is applied. Hence, it may require more computing resources during numerical simulations. In some areas of a model which has less importance in simulation, uniform discretization may increase the computing time without an obvious accuracy improvement. Therefore, based on this theory, we can have a better understanding of fracture analysis in marine batteries.

2.3 Numerical investigations of SOFC

As a common fuel cell type, SOFC is composed of solid electrodes and electrolyte. Ni, YSZ and perovskite-based LaMnO3 or LSCF are the most commonly used materials for anode, electrolyte and cathode, respectively [10], [11]. Electrode and electrolyte of SOFC are commonly made into layers and stacked on each other in a certain sequence. Besides, some electrolyte material is added inside the electrode layers in order to increase the efficiency of electrochemical reaction [12]. Hence, the

material properties may not be homogeneous. However, redox reaction in SOFC generates large amount of heat which rises the operating temperature up to around 800 ℃ [14]. High thermal load poses challenges for thermal stability of SOFC layers. Moreover, the misdistributed stress after volumetric expansion due to high temperature has become the main factor of structure defection and failure. Oxidised nickel (NiO) has a lower oxygen diffusivity which reduces the efficiency of redox reaction in SOFC layers [55].

Many efforts are devoted to fracture analysis through various numerical simulations and experiments. Since a SOFC layer is composed of different materials, the internal stress depends on different coefficient of thermal expansion of different components on the layer. Celik et al. found out that the stress depends on the percentage of electrode, electrolyte and pores on the layers [56]. They pointed out that stress can be reduced by increasing the percentage of Ni, YSZ and pores. Increasing porosity can significantly increase the efficiency in stress reduction. However, it also decreases the layers strength and reduces the cell performance by the reduction of TPB. Normal cell operation is a cycling of oxidization and reduction of cell electrode. For Ni based electrode, the Ni material experiences large volume change during cycling process. Timurkutluk et al. and Sarantaridis et al. have some detail studies on the volumetric effect by redox reaction [57]–[59]. During oxidization process, Ni particles get oxidized and transformed into NiO particles which leads to around 70% volumetric expansion. However, during reduction process, NiO particles will be reduced and transformed back into Ni particles which lead to around 42% volumetric shrink. Hence, the redox reaction can be regarded as an irreversible process. Since the SOFC layer is constrained by neighbour layers, after many cycling processes, stress will be accumulated in the layer. However, the critical stress for Ni is 317MPa [12]. When stresses exceed this value, damage will likely form and delamination and decomposition can happen in this SOFC layer.

Stress normally rises up during (i) manufacture, (ii) high operating temperature and (iii) anode re-oxidisation processes. For different SOFC structures, such as anode

supported cell and electrolyte supported cell, the failure probability of each layer is different [60]. Laurencin et al. summarised the relationship between cell structure and cell stage [60], [61]. After cell assembly, electrolyte support cell will introduce initial stress on anode which may become a potential for anode cracking, whereas the electrolyte and cathode layers are predicted as undamaged. In anode support cells, the thickness of electrolyte should be around 10 μm in order to avoid any degradation. However, high elastic energy stored in electrolyte causes delamination of electrodes and electrolyte layers. During anode reduction process, operating temperature keeps increasing and ceramic electrolyte will expand. Hence, the stress in electrolyte layer of both cell structures will release. During anode re-oxidisation process, Ni will transfer into NiO which leads to anode expansion. For anode supported structure, 0.12% to 0.15% expansion in volume is predicted to lead to electrolyte and cathode damage. For electrolyte supported structure, anode oxidisation may lead to delamination at the electrode/electrolyte surface.

The operating temperature of SOFC varies from 800℃ to 1000℃, which has provides a good environment for ions diffusing through the ceramic electrolyte and catalyses side reaction in the SOFC layers [62]. As mentioned above, the possible fuels for SOFC are not only hydrogen, but also various types of fossil fuels [63]. In marine environment, the major fuel injected into SOFC modules is marine diesel oil which contains hydrocarbon compound, hydrogen sulphide and chlorine hydride. Papurello et al. and Madi et al. found out that Ni is active to this halogen compounds [13], [15]–[17]. High operating temperature also leads to the degradation of material mechanical properties. Giraud et al. indicate that the elastic modulus of reduced anode plate (Ni-YSZ) keeps reducing as temperature increases until 430℃ and increasing when temperature is above 600℃ [64]. However, Pihlatie et al. show different results [65]. They investigate both Ni-YSZ plate and oxidised anode plate (NiO-YSZ). In their study, the elastic modulus of NiO-YSZ plate keeps constant at low temperature state, followed by a sharp increase up to 133GPa at 240℃. Then as temperature increases, young's modulus decreases and reaches to 110GPa at 1200℃.

For Ni-YSZ plate, elastic modulus keeps reducing through the whole heating up process.

2.4 Numerical investigations of lithium-ion battery

Performance of lithium ion battery mainly depends on material properties of anode, cathode and electrolyte. Several metals and compounds are selected as anode material such as Co, Ni, Mn and iron phosphate due to different performance in thermal stability, capacity, conductivity and safety [8]. Si is also found to be an excellent anode material in conventional lithium ion battery due to its high theoretical charging capacity (3600 ~ 4200mAHg-1) [66], [67]. However, as lithium ions penetrate into Si particles, the Si particles are expected to experience a large volume expansion up to 400% [66], [68]. Frequent cycling of the lithium ion battery will lead to stress misdistribution, degradation and delamination of the components especially electrodes and electrolyte and it will affect the battery performance.

Many efforts are conducted to avoid the defection and fracture of the Si based anode. Chan et al. established a new Si structure named Si nanowires in order to improve the battery performance [66]. Nanowire structures are embedded on metallic current collector. Due to small diameter of nanowire structure, anode will have higher tolerance on volumetric expansion with little defection. Nanowire structure exhibit higher electrical capacity than normal Si structure and it can sustain high capacity in high current situation. Since the nanowire is one dimensionally displaced on current collector, it is not easily smashed into small particles which increase the reliability of lithium ion batteries.

Liu et al. set up a thin Si film model to investigate the lithiation induced tensile stress and surface cracking by analytical technique and FEM [69]. They observed a compression-traction transition located on lithitaion and unlithiation surface zone. From their perspective, large volumetric expansion, plastic deformation and slow charging rate are the main factors which build up this transition and it will lead to

cracks and fracture. They also show that the magnitude and profiles of tensile stress at the surface of lithiated section depend on volumetric misfit strain, yield stress and modulus of unlithiated section.

Stamps and Huang conducted a mix mode fatigue evaluation of lithium ion battery by setting up a pre-cracked electrode model [70]. Stress energy release rate and crack surface energy are the main criteria in crack propagation prediction. The simulation was performed by considering a series of damage situations with crack length over width range from 0.05 to 0.9. They found out that if a crack could propagate under certain loading when the length of pre-existing crack is more than half size of the electrode width, the same loading will also lead propagation of a longer pre-existing crack for the same electrode. Otherwise, the comparison between maximum strain energy release rates and crack surface energy is necessary [29]. Ryu et al., on the other hand, believe that the size of Si nanowire may have influence on fracture of nanowire structure [68]. Maximum possible strain energy release rate and fracture toughness of Si were composed. They concluded that the Si nanowire with a diameter size less than 300 nm can hardly fail during cycling even the nanowire structure is initially damaged. This value also matched well with in-situ TEM experimental observations.

Ryu et al also mentioned that during normal cycling process, pressure gradients always formed along with the large volume changes [68] and it will affect the process of lithium diffusion in the electrode particles and crack evolution. Grantab and Shenoy provided an investigation about pressure gradient factor on crack propagation in Si nanowires [9]. They applied CZM to model fracture in nanowires and J-integral to calculate the stress state around fracture region in order to predict the fracture evolution. In early diffusion stage, since localised stress around the crack tip is lower than surrounding nanowire surface region, a large mass flux toward crack tip region occurs. Hence, large amount of lithium ions move into crack tip region which cause relatively larger volume expansion in this region. Then, the stress around the crack tip should be reduced. Similarly, Zuo and Zhao applied an

alternative method, phase field method, to study the stress evolution and crack propagation [71]. A series of damaged electrode models with different crack numbers and different crack orientations were considered to illustrate the evolution of fracture in electrode. They indicated that pressure gradient factor depends on Young's modulus, partial molar volume, lithium ion concentration, Poisson's ratio and the localised concentration around the crack tip region.

Gao and Zhou have investigated the softening effects caused by lithiation induced fracture in electrode material [72]. They set up a finite element framework and applied J-integral method to investigate the crack propagation. They also observed that large amount of lithium ions accumulate on crack tip regions during charging process, which cause a relaxation of hydrostatic stress. However, standard form of J-integral is no longer path independent due to pressure gradient factor.

2.5 Summary

Several numerical simulation methods in fracture analysis are provided in this chapter. The advantages and limitations of these methods are discussed. Various studies about fracture analysis on SOFC and lithium-ion battery are briefly explained. However, the numerical simulation methods, such as FEM, XFEM, BEM and CZM, are based on CCM, which has limitations in capturing the dynamic performance of fractures in material structure. Hence, PD is introduced in the fracture analysis of marine batteries as an alternative approach. Since PD does have definitions in both continuous and non-continuous domains, it has superiority in fracture prediction. Detailed information and studies about peridynamic theory are provided in the following chapters.

3 PERIDYNAMICS

3.1 Introduction

As mentioned in Chapter 2, classical numerical simulation methods based on FEM, such as FEM, BEM and CZM, have some limitations in fracture analysis. Hence, a new numerical simulation method, called peridynamics, is introduced by Silling in 2000. Generally, PD can be classified into three categories: bond-based PD, ordinary state-based PD and non-ordinary state-based PD. Bond-based PD is a simplified version of ordinary state-based PD by removing the dilatation term. Since all of the simulations in this thesis are based on brittle elastic material assumption, bond-based PD is applied as the numerical method in fracture analysis. In order to provide detailed information about bond-based PD, the nonlocal theory will be discussed in Section 3.2. Based on nonlocal theory, the bond-based PD will be illustrated in Section 3.3. The numerical implementation of this theory is provided in Section 3.4 followed by a summary of this Chapter in Section 3.5.

3.2 Nonlocal Theory

In general, physical variables, such as mass, temperature, voltage and stress, describe the influences among different parts in a material structure and body. In microscopic analysis, such as molecular dynamics, these influences are explained as the interactions among small particles of the material. The investigation of mirco-scale physics contributes to the understanding of various kinds of physical phenomenon [73]. Various theories were applied in the past to numerically simulate the behaviour of the material structure in micro-scale such as CCM. CCM was introduced by Cauchy in 19^{th} century [74]. In CCM, material body is assumed to be continuous throughout the whole structure and it is composed of infinite number of material particles that can only interact with their closest neighbours. Hence, CCM is regarded as a local theory. However, in microscopic analysis, material particles

can interact not only with close neighbours particles but also particles within a certain distance. The interaction between long-range material particles is named as long-range interaction and this interaction is evident in the microscopic analysis, especially in molecular dynamics [73]. Hence, CCM which is based on local theory may not be sufficient enough to describe the motion of each material particle.

Eringen and Edelen [75] and Eringen [76], [77] introduced a nonlocal continuum theory by taking the long-range interaction of elastic solids into consideration. Within the nonlocal theory, the existence of long-range force is evident for small scale problems. Hence, the material particles can build up interaction not only with particles of close neighbours, but also particles in the whole material structure or body. Weight functions are applied to describe the influence or the strength of interactions of the long range interactions. Based on this theory, the analysis of motion on microstructure is available by the continuum mechanics.

In order to increase the performance of batteries, some nanoscale structures, such as Si nanowires, are embedded on the surface of battery electrodes. Hence, nonlocal theory is important for the fracture analysis of these nanostructures. Eringen and Kim have proposed a criterion of crack propagation by calculating the critical stress value around crack tip under the framework of nonlocal continuum mechanics [78]. The results agreed with Griffith criterion for static fracture in linear elastic fracture mechanics (LEFM). In LEFM, according to $\sigma_{ij} = K/\sqrt{2\pi r}$, stresses reach infinitely large at crack tips. However, no material can withstand infinite stresses which make the prediction of stress value at crack tip meaningless. Rice, on the other hand, introduced a path independent method to calculate the strain concentration around cracks and notches [30]. For elastic materials, the J-integral value is identical with the strain energy release rate proposed by Irwin [27]. Since the integral contour stay finite distance to crack tips, it avoids the singularity and the J-integral value shows the average strain energy state within the contour region. As an alternative approach, a new nonlocal theory, called peridynamic theory, is introduced to solve the non-continuous problems in the following sections.

3.3 Bond-based peridynamic theory

3.3.1 Equation of motion

In CCM, the motion of each material particle is defined by the stress and body force, which can be expressed as:

$$\rho \frac{\partial^2 \vec{u}(\vec{x},t)}{\partial t^2} = \nabla \cdot \vec{\sigma} + \vec{b}(\vec{x},t) \tag{3.1}$$

where ρ, $\vec{u}$ and $\vec{b}$ refers to the density, displacement and body force of material particle $\vec{x}$ at time *t*. ∇ is Nabla operator, which shows gradient of stress tensor along the material geometry. Since Nabla operator is composed of a series of derivatives, describing the gradient of stress tensor on the particle $\vec{x}$ at time *t*, it does not have definition over non-continuous material geometries such as cracks. Hence, this has brought limitation for CCM in failure and fracture analysis.

As an alternative approach in dealing with fracture and failure analysis, the PD is first introduced by Silling in 2000 [19]. Particles can build up interactions or material bonds, which weave the whole material structure. Hence, in peridynamics, the equation of motion (Eq. (3.1)) for each particle can be rewritten as follows:

$$\rho \frac{\partial^2 \vec{u}(\vec{x},t)}{\partial t^2} = \int_{H_x} \vec{\mathrm{f}}\left(\vec{u}(\vec{x}',t) - \vec{u}(\vec{x},t), \vec{x}' - \vec{x}\right) dV_{x'} + \vec{b}(\vec{x},t) \tag{3.2}$$

where $\vec{\mathrm{f}}$ refers to the pairwise force functions for each bond between particles $\vec{x}'$ to $\vec{x}$. $V_{x'}$ represents the volume of particle $\vec{x}'$. Material particle $\vec{x}$ can build up interactions with neighbour particles within finite distance (shown as Fig. 3.1) and these neighbour particles have built up the horizon of the material particle $\vec{x}$ (H_x). It is assumed that particle $\vec{x}$ can not build up interaction beyond the horizon, because the contribution of the particles outside horizon for particle $\vec{x}$ is so weak that can be ignored. Horizon size, δ, is manually defined. Larger horizon size can lead to more

accurate result but requires longer computing time. As horizon size tends to 0, the Eq. (3.2) converge to Eq. (3.1). In this thesis, the horizon size is selected as 3 times of grid space in all simulations. Hence, material particles can build up long-range interaction with other particles which shows that PD is a nonlocal theory.

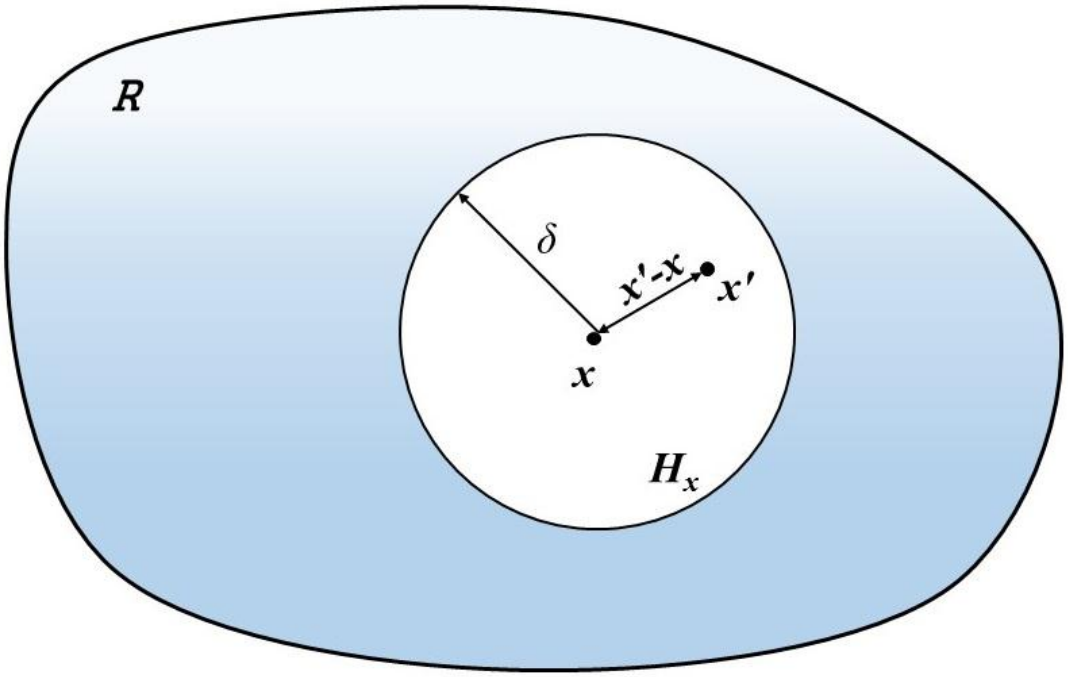

Figure 3.1. Horizon of material point *i*

The pairwise force function f is derived from strain energy density. In bond-based PD, the pairwise force function can be expressed by the reference configuration, deformed configuration (shown as Fig. 3.2) and material properties. In reference configuration, the relative position of two material particles is denoted by $\vec{\xi}$, where

$$\vec{\xi} = \vec{x}' - \vec{x} \tag{3.3}$$

and the relative displacement after deformation can be expressed as:

$$\vec{\eta} = \vec{u}\left(\vec{x}',t\right) - \vec{u}\left(\vec{x},t\right) \tag{3.4}$$

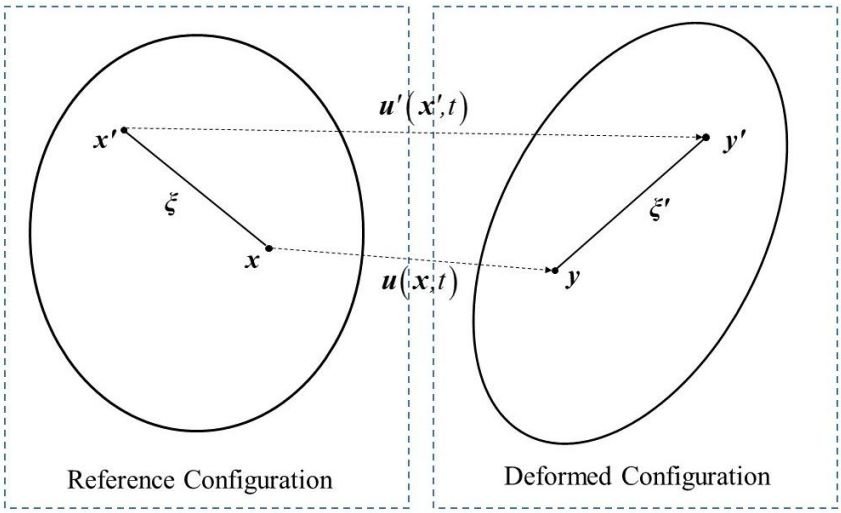

Figure 3.2. Reference and deformed configurations

Hence, $\vec{\xi}+\vec{\eta}$ shows the relative position after deformation and the stretch of the bond after deformation can be expressed as:

$$s=\frac{\left|\vec{\xi}+\vec{\eta}\right|-\left|\vec{\xi}\right|}{\left|\vec{\xi}\right|}-\alpha T_{avg} \tag{3.5}$$

where α refers to the coefficient of diffusive expansion and T_{avg} refers to the average concentration value of the bond. In thermal conduction analysis, α represents the coefficient of thermal expansion and T_{avg} refers to the average temperature value of the bond.

Material bond constant c does also affect the pairwise force function $\vec{f}$. In bond-based PD, the value of constant c depends on the horizon, elastic (Young's) modulus and structure geometry. There are different bond constants are applied for different dimensions which are listed in detail as follows:

Table 3.1. Material bond constant for three dimensions [31]

	Bond constants
one-dimension	$c = \frac{2E}{A\delta^2}$
two-dimension	$c = \frac{9E}{\pi h\delta^3}$
three-dimension	$c = \frac{12E}{\pi\delta^4}$

where E refers to elastic modulus of the material. A represents the cross-sectional area and h refers to the thickness of the two-dimension plate. Therefore the pairwise force function in bond-based PD can be expressed as:

$$\vec{f} = cs\frac{\vec{\xi} + \vec{\eta}}{\left|\vec{\xi} + \vec{\eta}\right|} \tag{3.6}$$

3.3.2 Failure definition

Crack formation and propagation in a material body will increase the crack surface area, but reduce the elastic energy of material particles [79]. Therefore, by comparing the strain energy release rate with crack surface energy, the dynamic motion of crack can be captured. In FEM, the VCCT is one of the most applied methods in calculating the energy release rate of the structure with fractures [80]. VCCT is derived from the Irwin's crack closure integral [79] and it is commonly used for mix-mode fracture analysis. However, as mentioned in Chapter 2, new surfaces (elements and nodes) should be manually introduced in the implementation of fracture formation and evolution, which is a computationally difficult process.

In PD, material particles build up interactions through bonds with each other in their horizons. Hence, the failure of material structure is reflected on the invalidation of

interaction, or “bond break”. If the material is brittle and the stretch of a material bond exceeds a certain value s_c, the bond will break (Fig. 3.3). Once the bond breaks, there is no longer interaction between the material points associated with this bond. Hence, the failure parameter can be defined to describe the state of a bond as:

$$\mu\left(t,\vec{\xi}\right)=\begin{cases}1 & , \quad s<s_c\\ 0 & , \quad s>s_c\end{cases} \tag{3.7}$$

where s_c represents the critical stretch. The bond force and bond stretch are linear related for brittle elastic material. Therefore, the local damage of the material point $\vec{x}$ can be expressed as:

$$\varphi\left(\vec{x},t\right)=1-\frac{\int_{H_x}\mu\left(\vec{x},t\right)dV_{\vec{x}'}}{\int_{H_x}dV_{\vec{x}'}} \tag{3.8}$$

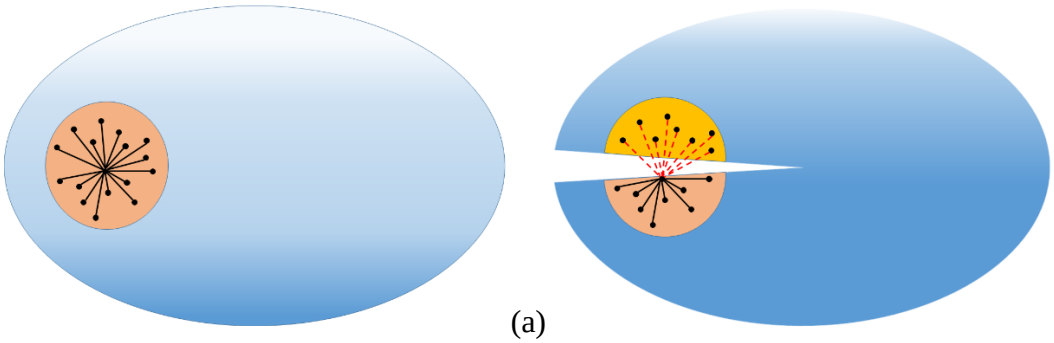

(a) (b)

Figure 3.3. Crack nucleation and propagation

Local damage is the percentage of the invalid (broken) bonds of material point $\vec{x}$. φ = 0 means particle $\vec{x}$ is undamaged and φ = 1 refers to particles $\vec{x}$ losing all of its interactions and becoming fully damaged. As more material points being damaged, crack forms and propagate automatically in the material structure as shown in Fig. 3.3.

The value of critical stretch depends on critical energy release rate, G_c [19]. G_c can be expressed according to peridynamics for two-dimensional plate as:

$$G_c = \frac{1}{4} c s_c^2 h \delta^4 \tag{3.9}$$

where h is the thickness of two-dimensional model. On the other hand, G_c can also be calculated from fracture toughness K [81] as:

$$G_c = \frac{K^2}{E} \tag{3.10}$$

By substituting Eqs. (3.3 ~ 3.10) into Eq. (3.2), the displacement of each material point can be calculated.

3.3.3 Pressure

The pressure state and stresses can also be evaluated as part of post-processing operation. Hydrostatic pressure can be derived from Cauchy stress and first Piola-Kirchoff stress. The first Piola-Kirchoff stress can be obtained in peridynamics [82], in two-dimension for example, as:

$$\sigma_0 = \int_{H_x} \vec{f} \otimes \left(\vec{x}' - \vec{x} \right) dV_{\vec{x}'} \tag{3.11}$$

Then, Cauchy stress can be calculated by the first Piola-Kirchoff stress and deformation gradient $\vec{F}$ as:

$$\sigma = J \sigma_0 F^T = \begin{bmatrix} \sigma_{11} & \sigma_{12} \\ \sigma_{21} & \sigma_{22} \end{bmatrix} \tag{3.12}$$

where

$$J = det\left(F \right) \tag{3.13}$$

and

$$F = \frac{2}{\pi h \delta^2} \int_{H_x} \frac{1}{\left|\vec{\xi}\right|^2} \left(\vec{\xi} + \vec{\eta}\right) \otimes \vec{\xi} dV_{x'} \tag{3.14}$$

Hence, the two-dimensional hydrostatic stress of the material point $\vec{x}$ can be expressed as:

$$\sigma_{hyd} = \frac{1}{2}\left(\sigma_{11} + \sigma_{22}\right) \tag{3.15}$$

Moreover, the pressure (P) of material point $\vec{x}$ can be defined as:

$$P = -\sigma_{hyd} \tag{3.16}$$

Since any stress tensor is the summation of hydrostatic stress and deviatoric stress, the deviatoric stress can be obtained as:

$$\sigma_{dev} = \sigma - \sigma_{hyd} I \tag{3.17}$$

where $\boldsymbol{I}$ is the identity matrix. Hence, the two-dimensional von-Mises stress can be calculated as:

$$\sigma_{VM} = \sqrt{2\sigma_{dev} : \sigma_{dev}} \tag{3.18}$$

3.4 Numerical implementation of peridynamic theory

Analytical solution of Eq. (3.1) is generally not possible for complex geometrical structures. Hence, numerical simulation methods are important to approximate the solution. In peridynamic theory, material structure is discretized by finite number of material particles. Each particle is represented by a material point as shown in Fig 3.4 with certain volume. The points inside horizon are marked as yellow, while outside horizon are marked as white. Material points inside the horizon can build up interaction with central particles via bonds, while the interaction is too weak for

points outside the horizon that can be ignored. The discretisation of the material structure is usually uniform and the shape of the horizon is not necessarily to be symmetric either.

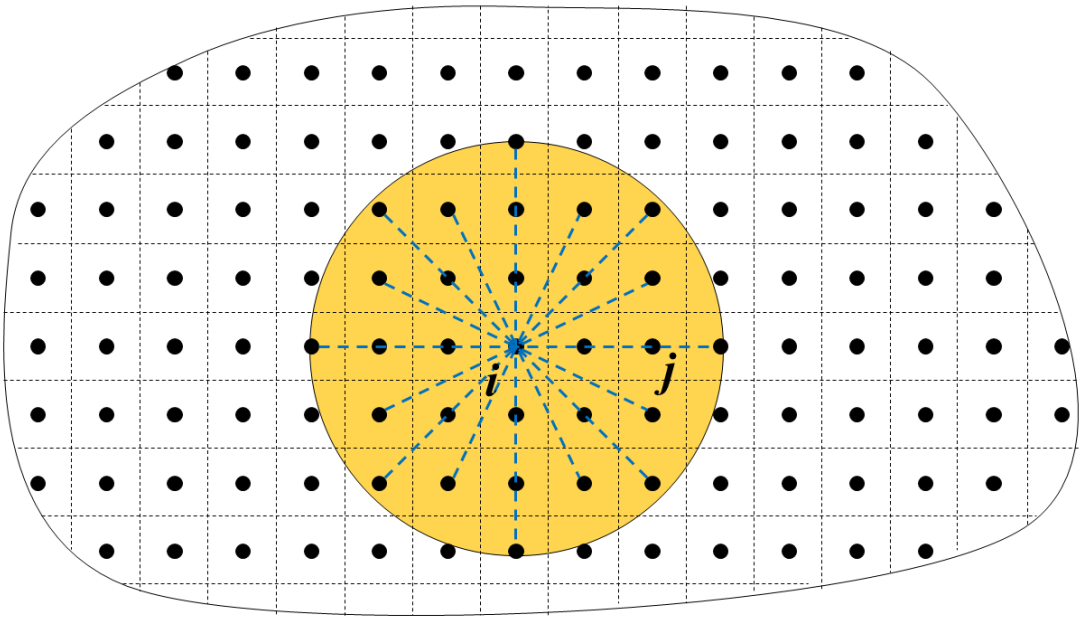

Figure 3.4. PD domain discretisation

In this thesis, the uniform discretisation and symmetric horizon are applied for simplicity. Therefore, Δ is used to represent the grid space or the distance between two close neighbour material particles. Hence, the discretised form of equation of motion of particle ***x*** (Eq. (3.2)) can be expressed as:

$$\rho\ddot{\vec{u}}\left(\vec{x}_i,t\right)=\sum_{j=1}^{n}\vec{f}\left(u\left(\vec{x}_j,t\right)-u\left(\vec{x}_i,t\right),\vec{x}_j-\vec{x}_i\right)V_j+\vec{b}\left(\vec{x}_j,t\right) \tag{3.19}$$

where *n* is the number of particles inside the horizon of material particle $\boldsymbol{x_i}$.

3.4.1 Volume correction factor

In order to simplify the numerical programming process, the spherical horizon is utilised in this thesis. Due to uniform discretisation, the particle volumes are usually

in cube shape for three-dimension, square shape for two-dimension and line shape for one-dimension. Therefore, volume of some particles, especially for those close to horizon boundary, can not be fully enclosed inside the horizon. In order to increase the accuracy of numerical simulation, a volume correction factor V_c is applied as a parameter to describe the real volume of these material particles.

As explain in [19], the horizon size depends on the characteristic length dimensions. For nanoscale model, the horizon may represent the maximum distance of physical interaction between atoms or molecules. For macroscale model, the horizon does not have a physical correspondence. The value of horizon in macroscale analysis can be manually selected for convenience. Rao has established benchmark studies of one-dimensional bar with six different horizon sizes (δ = 1, 3, 5, 10, 25, 50 times grid space) [83]. The model is discretized by very fine grid in order to minimize the numerical error. By comparing with analytical solution, he has found out that the highest accuracy is achieved for horizon size of δ = 1 and 3 times grid space. Furthermore, large horizon size requires better computing performance and more computing time. In this thesis, 3 times grid space horizon size are selected as horizon sizes due to its good accuracy. 1 time grid space can only capture crack propagation behavior and not applicable to crack branching behaviour [31]. For those particles, whose entire volume are fully enclosed inside the horizon, the volume correction factor is set as 1, i.e. V_c = 1. For those particles, whose entire volume is partially enclosed inside the horizon, the volume correction factor depends on bond length:

$$Vc = \frac{\delta - \left|\vec{\xi}\right|}{dx} + \frac{1}{2} \tag{3.20}$$

3.4.2 Surface correction factor

The motion of material particles is determined by numerical integration through their horizon members inside the horizon. For particles close to free surfaces, such as boundaries and crack surfaces (shown as Fig. 3.5), they may not have horizons in

full size. Since the free surface effect is problem dependent, it is difficult to get analytical solutions. Hence, surface correction factors are determined based on numerical implementation [31].

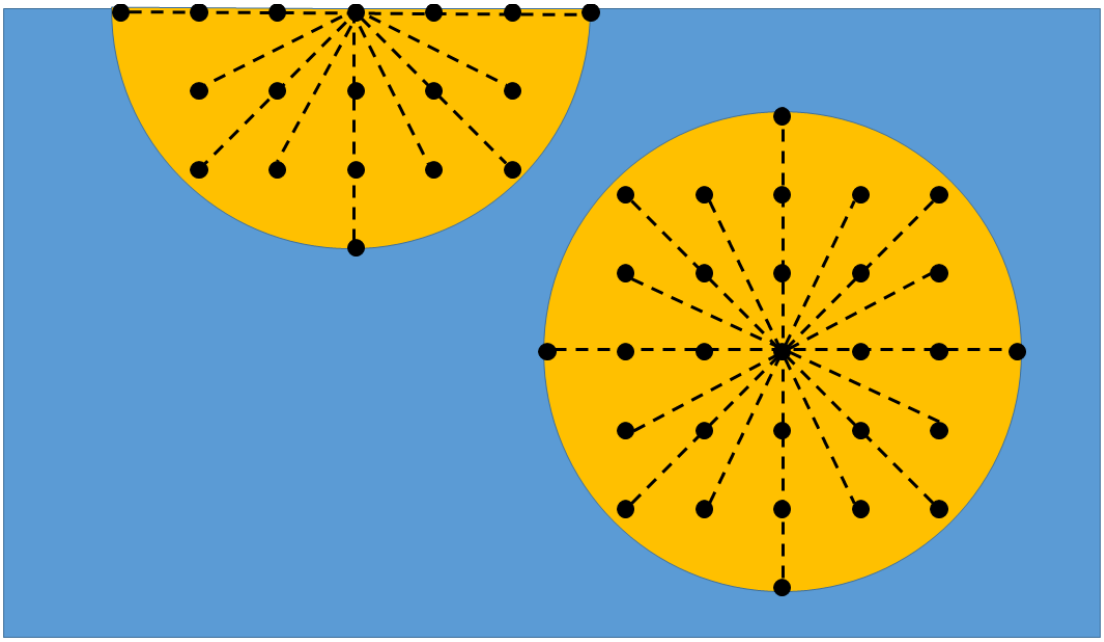

Figure 3.5. Surface effect in material structure

In bond-based PD, the surface correction factor is derived from the integration of strain energy density inside the material structure for simple loading conditions. By comparing the value of strain energy density by CCM and PD, the surface correction factor for material particles can be calculated.

In bond-based PD, the strain energy density for material particles relies on bond constant ***c*** and bond stretch *s*. The scalar micro-potential *w* can be represented as:

$$w = \frac{1}{2} c s^2 \xi \tag{3.21}$$

Since the micro-potential is associated with a bond, each material particle shares half of the micro-potential. By integrating the micro-potential through the whole horizon,

the numerical expression of total strain energy density of material particle $\boldsymbol{x}$ is shown as:

$$W_{PD} = \frac{1}{2}\sum_{i=1}^{n} w_{ij} V_j \tag{3.22}$$

In CCM, strain energy density is composed of the stress and strain state of material particle ($W_{CCM} = \frac{1}{2}\sigma\varepsilon$). The detailed expression of strain energy density varies according to the dimension of the problem. Hence, surface correction factor for each material point can be expressed as:

$$scf = \frac{W_{CCM}}{W_{PD}} \tag{3.23}$$

The components of surface correction factors in x, y and z directions, $\boldsymbol{g}(g_x, g_y, g_z)$, are derived from average values of surface correction factors of material particles on bond. They can build up the principal values of an ellipsoid, as shown in Fig. 3.6.

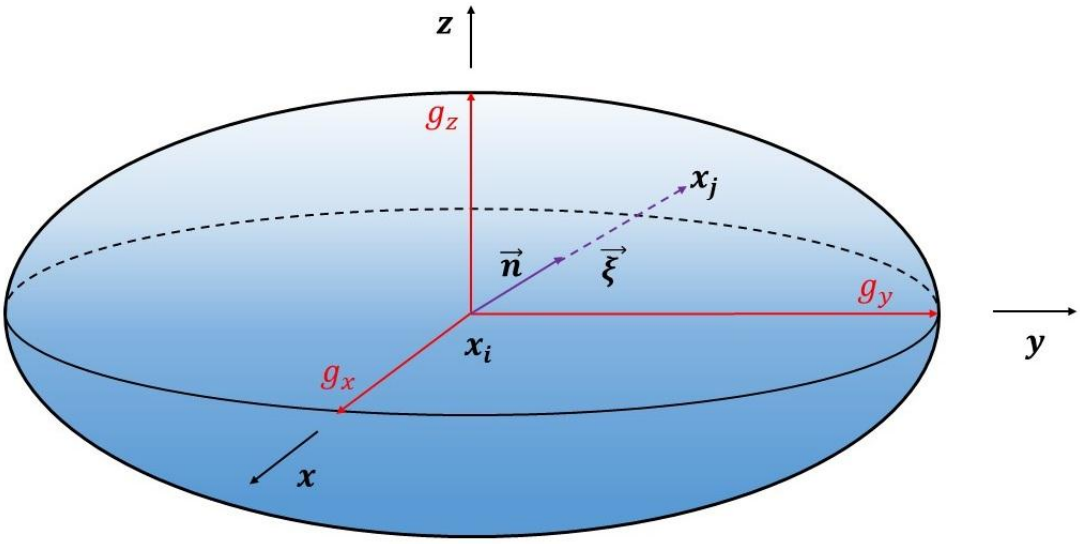

Figure 3.6. Construction of an ellipsoid for surface correction factors

Hence, the intersection of ellipsoid and direction vector, $\vec{n} = \left(\vec{x}_j - \vec{x}_i\right) \Big/ \left|\vec{x}_j - \vec{x}_i\right|$, builds up the correction factors of each bond as:

$$G = \left(\left[\frac{n_x}{g_x}\right]^2 + \left[\frac{n_y}{g_y}\right]^2 + \left[\frac{n_z}{g_z}\right]^2 \right)^{-\frac{1}{2}} \tag{3.24}$$

3.4.3 Numerical stability

3.4.3.1 Time convergence study

The explicit time integration is generally applied in the bond-based PD. For material particle $\boldsymbol{x_i}$, the acceleration is calculated from Eq. (3.2). Hence, the velocity and displacement can be calculated as:

$$\dot{\vec{u}}_i^{n+1} = \dot{\vec{u}}_i^{n} + \ddot{\vec{u}}_i^{n} \cdot \Delta t \tag{3.25a}$$

$$\vec{u}_i^{n+1} = \vec{u}_i^{n} + \dot{\vec{u}}_i^{n} \cdot \Delta t \tag{3.25b}$$

where $\vec{u}_i^{n+1}$ and $\vec{u}_i^{n}$ represent the displacement vectors of the material point $\boldsymbol{x_i}$ for the next and the current time step respectively. $\dot{\vec{u}}_i^{n+1}$ and $\dot{\vec{u}}_i^{n}$ refer to the velocity vectors of the material point $\boldsymbol{x_i}$ for the next and the current time step, respectively. $\ddot{\vec{u}}_i^{n}$ is the acceleration vector of the material point $\boldsymbol{x_i}$ for the current time step and Δt represents the time step length. Since the explicit time integration is applied in numerical simulations, results are sensitive to time step length Δt. The stability condition is determined by material properties and discretisation, as shown in Eq. (3.26) [19], [31], derived from von Neumann stability analysis [84]

$$\Delta t < \beta \sqrt{\frac{2\rho}{\sum_p V_p C_{ip}}} \tag{3.26}$$

where $C_{ip} = |\partial f / \partial \eta|$. A safety factor β (varies from 0 to 1) is applied in Eq. 3.26 to improve the stability condition.

A square plate with pre-existing single crack is selected as the specimen of time convergence study as shown in Fig. 3.7. The size of the plate sides is 5cm and the size of the crack length is 20% of the side length. The plate is uniformly discretised into 200 points in both x and y directions. Hence, the total number of the discretisation is 40000 particles. This plate suffers from velocity boundary loading (50m/s) on the top and bottom edges and this process last for 1.6667e-5 second. If we assume that the critical time step size for mechanical deformation is $t_c = \sqrt{\frac{2\rho}{\sum_p V_p C_{ip}}}$, simulations with different time step sizes, $\Delta t = \left(0.05 \quad 0.1 \quad 0.2 \quad 0.4 \quad 0.5 \quad 0.8 \quad 1.0 \quad 1.5 \quad 2.0 \quad 2.5\right) \times t_c$, are considered.

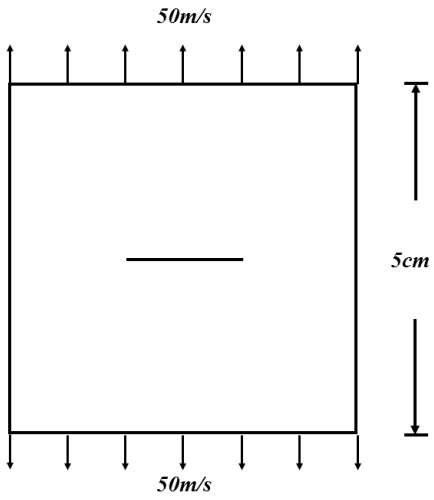

Figure 3.7. Initial damage plot of square plate specimen with pre-existing crack

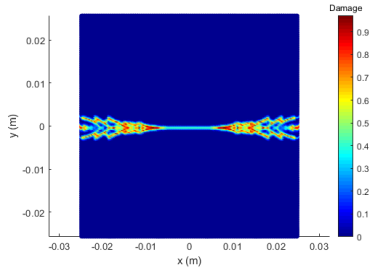
Damage
y (m)
x (m)

(a)

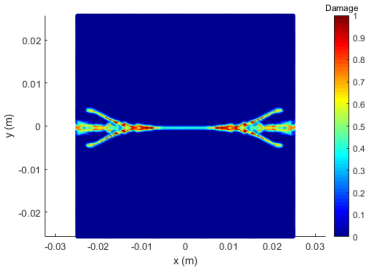
Damage
y (m)
x (m)

(b)

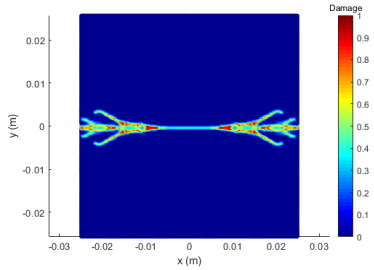
Damage
y (m)
x (m)

(c)

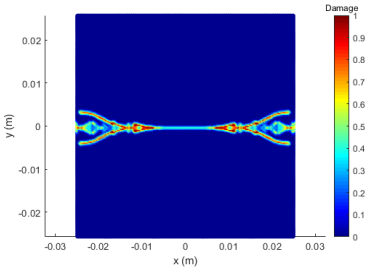
Damage
y (m)
x (m)

(d)

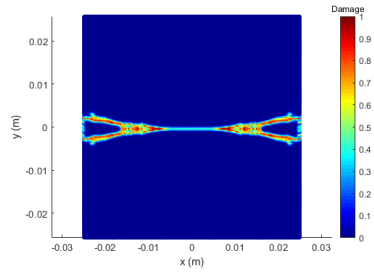
Damage
y (m)
x (m)

(e)

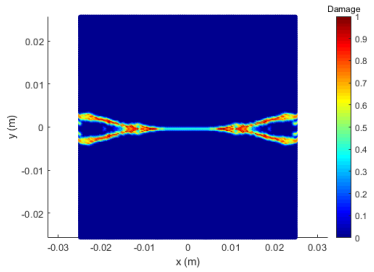
Damage
y (m)
x (m)

(f)

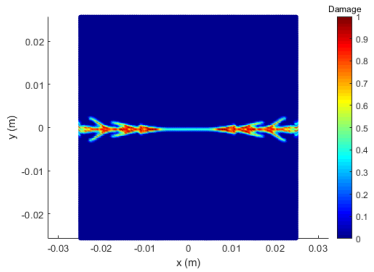
Damage
y (m)
x (m)

(g)

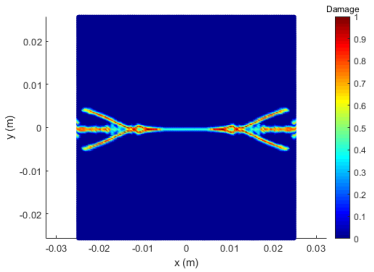
Damage
y (m)
x (m)

(h)

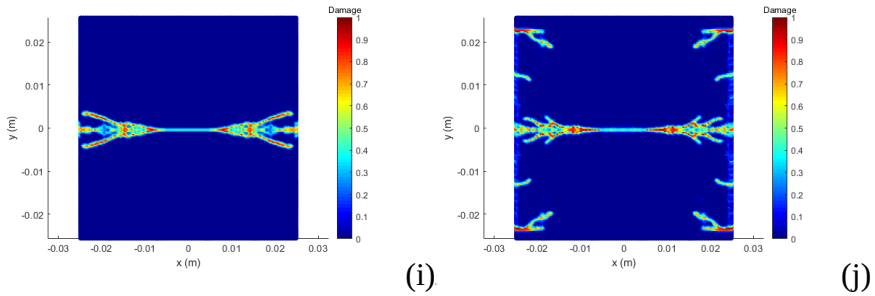

Figure 3.8. Results of time convergence study: (a) $0.05t_c$ (b) $0.1t_c$ (c) $0.2t_c$ (d) $0.4t_c$ (e) $0.5t_c$ (f) $0.8t_c$ (g) $1.0t_c$ (h) $1.5t_c$ (i) $2.0t_c$ (j) $2.5t_c$

According to Fig. 3.8, simulation with $0.05t_c$ time step size is the most refined case which can capture crack propagation and multiple branching cracks. As time step size increase, the results become coarse and fuzzy. In the cases of $0.5t_c$ and $0.8t_c$, only two branching cracks can captured. After $1.0t_c$, results become fluctuate and unstable. Results shows serious distortion at $2.5t_c$, since unwanted cracks emerge on the boundary region of the plate. For the cases with time step sizes larger than $2.5t_c$, results is fully distorted and there has no stable result that can be plotted.

However, the cases with most refined result requires larger amount computing times depends on the computing performance. In some situations, the most refined result is impractical. Hence, we need negotiation between time refinement and computing performance. Within the critical time step size t_c, the results follows the similar trend in terms of the way of crack propagation and crack branching. Usually, we set the safety factor $\beta=(0.5\sim0.8)\times t_c$ to keep relative good accuracy, save computing resource and avoid destroying stability.

3.4.3.2 Size Convergence study

Apart from time step size, the grid size or size of discretization can also have influence on accuracy and stability of numerical simulation. Similar to meshing process by nodes and element in FEM, PD apply material points with finite volume to discretized material body. Therefore the analytical solution can be explained by

integrating the material points. In this study, the same numerical model is selected as shown in Fig. 3.7. Several discretization with 25×25 50×50 80×80 100×100 200×200 500×500 particles are discussed. The time step size is selected as 1.3367e-8 second and this process will last 1250 steps.

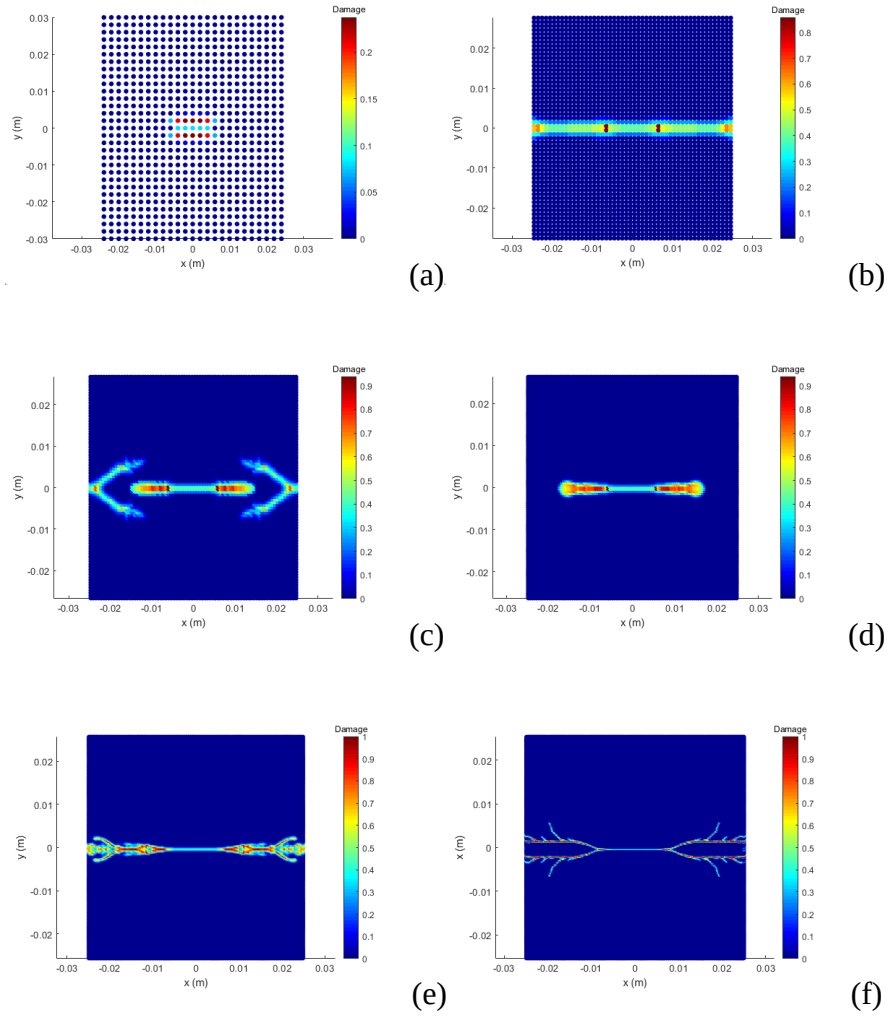

Figure 3.9. Results for size convergence study: (a) 25×25 points (b) 50×50 points (c) 80×80 points (d) 100×100 points (e) 200×200 points (f) 500×500 points

Fig. 3.9 shows results of crack propagation with different discretisation under velocity boundary condition. For the cases of 25×25 points, 50×50 points and

80×80 points, we can observe fluctuating results like no crack propagation, crack over propagation and abnormal crack propagation, respectively. For the cases of 100×100 points, 200×200 points and 500×500 points, crack propagation and crack branching is stable.

In general, as the number of material points increase, numerical model will become more refined and the numerical results will be more accurate. However, more computing time and higher computing performance are required at the same time. In order to optimise computing resource and keep relative high accuracy and high stability, heterogeneous discretisation scheme is commonly applied in numerical simulation. However, the heterogeneous discretisation is currently not available in bond-based PD due to some issues such as horizon, volume correction factor, weight function, etc. Therefore uniform discretisation has to be applied in this thesis. The number of material points that selected during discretisation does not have a clear rule and it depends on the complexity of the models and problems.

3.5 Adaptive Dynamic Relaxation

Although PD is based on the equation of motion in dynamic form, it can also solve static problem. The static solution is regarded as a special situation in transient response of the solution, as explained by [85]. The fluctuating results will converge to a certain value by introducing a damping factor to the dynamic motion of the system, and then the static solution can be obtained. The damping factor is an artificial value which may not always converge to the results efficiently. Hence, the adaptive dynamic relaxation scheme is applied by Underwood [86].

The equation of motion by peridynamics can be rewritten as a series of ordinary differential equations (ODE) by introducing new fictitious inertia and damping terms as:

$$D\ddot{\vec{U}}\left(\vec{X},t\right)+c^{n}D\dot{\vec{U}}\left(\vec{X},t\right)=F\left(\vec{U},\vec{U}',\vec{X},\vec{X}'\right) \tag{3.27}$$

where D is the fictitious diagonal density matrix and c^n is the damping coefficient determined by Greschgorin's theorem [86] and Rayleigh's quotient, respectively. $\boldsymbol{F}$ is the vector which depends on the initial position ($\vec{X}$) and displacement ($\vec{U}$) and it is composed of peridynamic interaction and body forces. The components of force vector for material point ***i*** can be expressed as:

$$\vec{F}_i = \sum_{j=1}^{N} \left(\vec{t}_{(i)(j)} - \vec{t}_{(j)(i)} \right) V_{(j)} + \vec{b}_{(i)} \tag{3.28}$$

where V_j shows the actual volume of material point ***j*** (the horizon member of point ***i***), hence it should be multiplied by a volume correction factor. $\vec{t}$ is the force vector represented based on ordinary peridynamic theory. In Eq. (3.27), the density matrix, D, the damping coefficient c and time step size (Δt) do not have physical quantities and they can be manually defined in order to get a fast convergence in numerical analysis. Therefore, in adaptive dynamic relaxation technique, the explicit time integration scheme can be applied in numerical simulations. In general, the time step size can be manually selected as 1 for a convenient calculation. According to Greschgorin's theorem, the diagonal elements of the density matrix, D, can be expressed as:

$$\lambda_{ii} \geq \frac{1}{4} \Delta t^2 \sum_j \left| K_{ij} \right| \tag{3.29}$$

where K_{ij} is the stiffness matrix of the system and it is derived from the peridynamic interaction force with respect to the relative displacement vector, $\vec{\eta}$. The elements of the stiffness matrix, K_{ij}, can be calculated by applying the small displacement assumption as:

$$\sum_j^N \left| K_{ij} \right| = \sum_{j=1}^{N} \frac{\partial \left(\vec{t}_{(i)(j)} - \vec{t}_{(j)(i)} \right)}{\partial \left(\left| \vec{u}_{(j)} - \vec{u}_{(i)} \right| \right)} \cdot \vec{e} = \sum_{j=1}^{N} \frac{\left| \vec{\xi}_{(i)(j)} \cdot \vec{e} \right|}{\left| \vec{\xi}_{(i)(j)} \right|} \frac{4\delta}{\left| \vec{\xi}_{(i)(j)} \right|} \left(\frac{1}{2} \frac{a d^2 \delta}{\left| \vec{\xi}_{(i)(j)} \right|} \left(v_{c(i)} V_{(i)} + v_{c(j)} V_{(j)} \right) + \vec{b} \right)$$

(3.30)

where $\vec{e}$ is the unit vector along the x, y and z coordinates in Cartesian coordinate system.

Since the elements of the density matrix given in Eq. (3.29) may have large numerical values, which can lead to numerical, Then, Eq. (3.27) can be rewritten at the n^{th} iteration as:

$$\ddot{\vec{U}}^n\left(\vec{X},t^n\right)+c^n\dot{\vec{U}}^n\left(\vec{X},t^n\right)=D^{-1}\vec{F}^n\left(\vec{U}^n,\vec{U}'^n,\vec{X},\vec{X}'\right) \tag{3.31}$$

Damping coefficient can be calculated by applying the lowest frequency of the system. The lowest frequency can be derived by using Rayleigh's quotient as:

$$\omega=\sqrt{\frac{U^TKU}{U^TDU}} \tag{3.32}$$

Hence, the damping coefficient c^n can be expressed by Eq. (3.31) and Eq. (3.32) as:

$$c^n=2\sqrt{\left(\left(U^n\right)^T\,{}^lK^nU^n\right)/\left(\left(U^n\right)^TU^n\right)} \tag{3.33}$$

in which ${}^lK^n$ is the diagonal "local" stiffness matrix which is given as:

$${}^lK_{ii}^n=-\left(F_i^n/\lambda_{ii}-F_i^{n-1}/\lambda_{ii}\right)\Big/\left(\Delta t\dot{u}_i^{n-1/2}\right) \tag{3.34}$$

Recalling the Eq. (3.31) and by applying central-difference scheme, displacements and velocities for the next time step can be obtained as:

$$\dot{\vec{U}}^{n+1/2}=\frac{\left(\left(2-c^n\Delta t\right)\dot{\vec{U}}^{n-1/2}+2\Delta tD^{-1}\vec{F}^n\right)}{\left(2+c^n\Delta t\right)} \tag{3.35a}$$

and

$$\vec{U}^{n+1} = \vec{U}^{n} + \Delta t \vec{\dot{U}}^{n+1/2} \tag{3.35b}$$

where n represents the n^{th} iteration. However, at first iteration, the physical values at $t^{-1/2}$ does not have physical meanings. Then the initial displacement field and initial velocity field are assumed as $U^0 \neq 0$ and $\dot{U} = 0$. Hence, the integration can be started by:

$$\dot{U}^{1/2} = \frac{\Delta t D^{-1} F^0}{2} \tag{3.36}$$

3.6 Summary

In this chapter, basic information about peridynamics is provided. PD has shown as an alternative method in solving both dynamic and static problems. Without meshing, the material body or structure is discretised into finite amount of material particles. Each particle is represented by a material point with finite volume. Each pair of material particles, within a certain distance can build up interaction via "bond". The fracture and failure can be easily represented by "bond breakage". It is the major convenience and advantage of peridynamic theory over other kind of finite element analysis in fracture analysis. PD equations can be solved by using the explicit time integration scheme which is sensitive to the time step size. Large time size may not lead to convergent results. Therefore, a stability condition, which is derived from material properties and discretisation, is necessary in the simulations.

4 PERIDYNAMIC DIFFERENTIAL OPERATOR

4.1 Introduction

Generally, PDEs are applied to describe most kind of physical phenomena, such as thermal conduction, ion diffusion and mechanical deformation. Unlike ODEs, PDEs contain functions with multiple unknown variables and partial derivatives. They are usually applied to model multi-physical problems. For some complicated PDEs, it is impractical to get the analytical solution. With the help of computer power, the numerical approximation of PDEs becomes a feasible method. The FEM, finite volume method (FVM) and finite difference method (FDM) are the most widely used in numerical approximation of PDEs. However, as discussed in previous chapters, the FEM, FVM and FDM may encounter difficulties in solving discontinuous problems. Hence, based on peridynamic theory, a new numerical differential scheme, PDO, is provided in this chapter.

4.2 Peridynamic differential operator

PDO is introduced by Madenci [87] by transferring the local form PDEs into non-local form. The concept of "Horizon" is applied to the PDO. In other words, the value of PDEs on material particles depends on their horizon members. The numerical expression of PDO depends on dimensions of the problem and it will be presented respectively in following sections.

4.2.1 One-dimensional peridynamic differential operator

The PDO can be derived from the Taylor Series. For the one-dimensional case, the Taylor series can be expressed as:

$$f\left(\vec{x}_j\right) = f\left(\vec{x}_i\right) + \vec{\xi}\frac{\partial f\left(\vec{x}_i\right)}{\partial x} + \frac{1}{2!}\vec{\xi}^2\frac{\partial^2 f\left(\vec{x}_i\right)}{\partial x^2} + R \tag{4.1}$$

Eq. (4.1) shows the one dimensional second order Tayler Series. *R* represents the remainder terms which are small enough to be neglected. $f\left(\vec{x}\right)$ is the physical variable depending on the problem of interest. $\vec{x}_j$ is one of the horizon members of the material point $\vec{x}_i$ and $\vec{\xi}$ refers to the distance between these points. By moving the first term on the right hand side of Eq. (4.1) to the left hand side, the Eq. (4.1) can be rewritten as:

$$f\left(\vec{x}_j\right) - f\left(\vec{x}_i\right) = \xi\frac{\partial f\left(\vec{x}_i\right)}{\partial x} + \frac{1}{2!}\xi^2\frac{\partial^2 f\left(\vec{x}_i\right)}{\partial x^2} + R \tag{4.2}$$

Multiplying each term in Eq. (4.2) by a peridynamic function, $g_1^p\left(\vec{\xi}\right)$, with *p* = 1, 2 and integrating over the horizon of material point $\boldsymbol{x_i}$, Eq.(4.2) will become:

$$\int_{H_x}\left(f\left(\vec{x}_j\right) - f\left(\vec{x}_i\right)\right)g_1^p\left(\vec{\xi}\right)dV = \frac{\partial f\left(\vec{x}_i\right)}{\partial x}\int_{H_x}\xi g_1^p\left(\vec{\xi}\right)dV + \frac{\partial^2 f\left(\vec{x}_i\right)}{\partial x^2}\int_{H_x}\frac{1}{2!}\vec{\xi}^2 g_1^p\left(\vec{\xi}\right)dV \tag{4.3}$$

By considering the orthogonality property of peridynamic functions:

$$\frac{1}{n!}\int_{H_x}\vec{\xi}^n g_1^p\left(\vec{\xi}\right)dV = \delta_{np} \tag{4.4}$$

where *n*, *p* = 0, 1, 2 and δ_{np} represents the Kronecker Delta. Substituting the Eq. (4.4) in Eq. (4.3), we have:

$$\begin{Bmatrix} \dfrac{\partial f\left(\vec{x}_i\right)}{\partial x} \\ \dfrac{\partial^2 f\left(\vec{x}_i\right)}{\partial x^2} \end{Bmatrix} = \int_{H_x}\left(f\left(\vec{x}_j\right) - f\left(\vec{x}_i\right)\right)\begin{Bmatrix} g_1^1\left(\vec{\xi}\right) \\ g_1^2\left(\vec{\xi}\right) \end{Bmatrix}dV \tag{4.5}$$

The one-dimensional peridynamic functions g_1^P contains weight function ω and unknown coefficients a_i^p which can be constructed as [87]:

$$g_1^p\left(\vec{\xi}\right) = a_1^p \omega\left(\vec{\xi}\right)\vec{\xi} + a_2^p \omega\left(\vec{\xi}\right)\vec{\xi}^2 \tag{4.6}$$

The weight function $\boldsymbol{\omega}$ is a manually defined function which describes the strength of the bond interaction. Generally, for most kind of materials, longer bonds should have weaker interactions. For bonds longer than horizon size, the interaction strength is so much weak which can be ignored. The exponential functions are usually applied for the weight function. However, for simple numerical simulation and relatively high accuracy, the weight function in this thesis is represented by:

$$\omega_p\left(\vec{\xi}\right) = \left(\frac{\delta}{\left|\vec{\xi}\right|}\right)^{p+1} \tag{4.7}$$

The orthogonality property of the PD functions requires that:

$$\sum_{q=1}^{2-q} A_{nq} a_q^p = b_n^p \tag{4.8}$$

in which q = 1 or 2 and

$$b_n^p = n!\delta_{np} \tag{4.9}$$

Eq.(4.8) can be written in matrix form by using the shape matrix $\boldsymbol{A}$, the unknown matrix $\boldsymbol{a}$ and the known matrix $\boldsymbol{b}$ and they can be expressed as:

$$A_{nq} = \int_H \omega_q\left(\vec{\xi}\right)\vec{\xi}^{n+q} dV \tag{4.10}$$

where

$$A_{11} = \sum_{j=1}^{n} \omega_1\left(\vec{\xi}\right)\vec{\xi}^2 V_j \tag{4.11a}$$

$$A_{12} = \sum_{j=1}^{n} \omega_2\left(\vec{\xi}\right)\vec{\xi}^3 V_j \tag{4.11b}$$

$$A_{21} = \sum_{j=1}^{n} \omega_1\left(\vec{\xi}\right)\vec{\xi}^3 V_j \tag{4.11c}$$

$$A_{22} = \sum_{j=1}^{n} \omega_2\left(\vec{\xi}\right)\vec{\xi}^4 V_j \tag{4.11d}$$

By calculating Eqs. (4.11)Eq. (4.10) can be rewritten as:

$$A = \begin{bmatrix} A_{11} & A_{12} \\ A_{21} & A_{22} \end{bmatrix} = \begin{bmatrix} 2A\delta^3 & 0 \\ 0 & A\delta^5 \end{bmatrix} \tag{4.12}$$

According to Eq. (4.9), $b_1^1 = 1 \text{and} b_2^2 = 2$. Therefore the unknown matrix ***a*** can be obtained as:

$$a = \begin{bmatrix} a_1^1 & a_1^2 \\ a_2^1 & a_2^2 \end{bmatrix} = \begin{bmatrix} \frac{1}{2A\delta^3} & 0 \\ 0 & \frac{1}{A\delta^5} \end{bmatrix} \begin{bmatrix} b_1^1 & 0 \\ 0 & b_2^2 \end{bmatrix} = \begin{bmatrix} \frac{1}{2A\delta^3} & 0 \\ 0 & \frac{2}{A\delta^5} \end{bmatrix} \tag{4.13}$$

Substituting Eq. (4.7) and Eq. (4.13) in Eq. (4.6), the one dimensional peridynamic functions can be expressed as:

$$g_1^1 = \frac{1}{2A\delta\left|\vec{\xi}\right|} \tag{4.14a}$$

$$g_1^2 = \frac{2}{A\delta^2\left|\vec{\xi}\right|} \tag{4.14b}$$

By substituting Eqs. (4.14) in Eq. (4.5), the one dimensional PDEs can be written in terms of peridynamic form.

4.2.2 Two-dimensional peridynamic differential operator

Recalling the Taylor Series, the physical variables $f\left(\vec{x}_j\right)$ can be expressed as:

$$f\left(\vec{x}_j\right)=f\left(\vec{x}_i\right)+\xi_1\frac{\partial f\left(\vec{x}_i\right)}{\partial x_1}+\xi_2\frac{\partial f\left(\vec{x}_i\right)}{\partial x_2}+\frac{1}{2!}\xi_1^2\frac{\partial^2 f\left(\vec{x}_i\right)}{\partial x_1^2}+\frac{1}{2!}\xi_2^2\frac{\partial^2 f\left(\vec{x}_i\right)}{\partial x_2^2}+\xi_1\xi_2\frac{\partial^2 f\left(\vec{x}_i\right)}{\partial x_1\partial x_2}+R \tag{4.15}$$

where. ξ_1 and x_1 refer to the *x* component of the bond $\vec{\xi}$ and material point position $\vec{x}_i$ respectively. ξ_2 and x_2 refer to the *y* component of material bond $\vec{\xi}$ and material point position $\vec{x}_i$ respectively. *R*, as remainder terms, is small enough to be neglected. By moving the first term on the right hand side of Eq. (4.15) to the left hand side, multiplying each term with a peridynamic function $g_2^{p_1p_2}\left(\vec{\xi}\right)$ (with p_1, p_2 = 0, 1, 2 except $p_1 = p_2 = 0$) and integrating through the horizon, Eq. (4.15) can be expressed as:

$$\begin{aligned}&\int_{H_x}\left(f\left(\vec{x}_j\right)-f\left(\vec{x}_i\right)\right)g_2^{p_1p_2}\left(\vec{\xi}\right)dV=\\&\frac{\partial f\left(\vec{x}_i\right)}{\partial x_1}\int_{H_x}\xi_1 g_2^{p_1p_2}\left(\vec{\xi}\right)dV+\frac{\partial f\left(\vec{x}_i\right)}{\partial x_2}\int_{H_x}\xi_2 g_2^{p_1p_2}\left(\vec{\xi}\right)dV+\\&\frac{\partial^2 f\left(\vec{x}_i\right)}{\partial x_1^2}\int_{H_x}\frac{1}{2!}\xi_1^2 g_2^{p_1p_2}\left(\vec{\xi}\right)dV+\frac{\partial^2 f\left(\vec{x}_i\right)}{\partial x_2^2}\int_{H_x}\frac{1}{2!}\xi_2^2 g_2^{p_1p_2}\left(\vec{\xi}\right)dV+\frac{\partial^2 f\left(\vec{x}_i\right)}{\partial x_1\partial x_2}\int_{H_x}\xi_1\xi_2 g_2^{p_1p_2}\left(\vec{\xi}\right)dV\end{aligned} \tag{4.16}$$

The orthogonality property of the peridynamic function can be shown as:

$$\frac{1}{n_1!n_2!}\int_{H_x}\xi_1^{n_1}\xi_2^{n_2}g_2^{p_1p_2}\left(\vec{\xi}\right)dV=\delta_{n_1p_1}\delta_{n_2p_2}\ \text{with } n_1, n_2 = 0\ ,\ 1\ ,\ 2 \tag{4.17}$$

where δ_{np} is the Kronecker delta. By substituting Eq. (4.17) into Eq. (4.16), relations between partial derivatives and peridynamic functions can be expressed as:

$$\begin{Bmatrix} \dfrac{\partial f(\vec{x}_i)}{\partial x_1} \\ \dfrac{\partial f(\vec{x}_i)}{\partial x_2} \\ \dfrac{\partial^2 f(\vec{x}_i)}{\partial x_1^2} \\ \dfrac{\partial^2 f(\vec{x}_i)}{\partial x_2^2} \\ \dfrac{\partial^2 f(\vec{x}_i)}{\partial x_1 \partial x_2} \end{Bmatrix} = \int_{H_x} \left(f(\vec{x}_j) - f(\vec{x}_i) \right) \begin{Bmatrix} g_2^{10}(\vec{\xi}) \\ g_2^{01}(\vec{\xi}) \\ g_2^{20}(\vec{\xi}) \\ g_2^{02}(\vec{\xi}) \\ g_2^{11}(\vec{\xi}) \end{Bmatrix} dV \tag{4.18}$$

The two-dimensional peridynamic functions $g_2^{p_1 p_2}(\vec{\xi})$ are constructed by polynomials which contains weight function $\boldsymbol{\omega}$ and coefficients of unknown matrix $\boldsymbol{a}$ as:

$$\begin{aligned} g_2^{p_1 p_2}(\vec{\xi}) = {} & a_{10}^{p_1 p_2} \omega_{10}(\vec{\xi}) \xi_1 + a_{01}^{p_1 p_2} \omega_{01}(\vec{\xi}) \xi_2 + a_{20}^{p_1 p_2} \omega_{20}(\vec{\xi}) \xi_1^2 + \\ & a_{02}^{p_1 p_2} \omega_{02}(\vec{\xi}) \xi_2^2 + a_{11}^{p_1 p_2} \omega_{11}(\vec{\xi}) \xi_1 \xi_2 \end{aligned} \tag{4.19}$$

The unknown coefficient matrix $\boldsymbol{a}$ above depends on peridynamic shape matrix $\boldsymbol{A}$ and known coefficient matrix $\boldsymbol{b}$ with a relationship shown below:

$$\sum_{q_1=0}^{2} \sum_{q_2=0}^{2-q_1} A_{(n_1 n_2)(q_1 q_2)} a_{q_1 q_2}^{p_1 p_2} = b_{n_1 n_2}^{p_1 p_2} \tag{4.20}$$

In which q_1, q_2 = 0, 1, 2 and q_1 and q_2 can not be both equal to 0. The peridynamic shape matrix $\boldsymbol{A}$ depends on the weight functions $\boldsymbol{\omega}$ and relative position of interacting material particles associated with the bond. The relationship between these factors is shown as follow:

$$A_{(n_1n_2)(p_1p_2)} = \int_{H_x} \omega_{q_1q_2}\left(\vec{\xi}\right)\xi_1^{n_1+p_1}\xi_2^{n_2+p_2}dV \tag{4.21}$$

The known coefficient matrix ***b*** can be constructed as:

$$b_{n_1n_2}^{p_1p_2} = n_1!n_2!\delta_{n_1p_1}\delta_{n_2p_2} \tag{4.22}$$

and the weight function is:

$$\omega_{q_1q_2} = \left(\frac{\delta}{\left|\vec{\xi}\right|}\right)^{q_1+q_2+1} \tag{4.23}$$

The peridynamic shape matrix ***A*** can be written based on Eq. (4.21) as:

$$\begin{bmatrix} A_{(10)(10)} & A_{(10)(01)} & A_{(10)(20)} & A_{(10)(02)} & A_{(10)(11)} \\ A_{(01)(10)} & A_{(01)(01)} & A_{(01)(20)} & A_{(01)(02)} & A_{(01)(11)} \\ A_{(20)(10)} & A_{(20)(01)} & A_{(20)(20)} & A_{(20)(02)} & A_{(20)(11)} \\ A_{(02)(10)} & A_{(02)(01)} & A_{(02)(20)} & A_{(02)(02)} & A_{(02)(11)} \\ A_{(11)(10)} & A_{(11)(01)} & A_{(11)(20)} & A_{(11)(02)} & A_{(11)(11)} \end{bmatrix} = \begin{bmatrix} \frac{1}{2}\pi h\delta^4 & 0 & 0 & 0 & 0 \\ 0 & \frac{1}{2}\pi h\delta^4 & 0 & 0 & 0 \\ 0 & 0 & \frac{1}{4}\pi h\delta^6 & \frac{1}{12}\pi h\delta^6 & 0 \\ 0 & 0 & \frac{1}{12}\pi h\delta^6 & \frac{1}{4}\pi h\delta^6 & 0 \\ 0 & 0 & 0 & 0 & \frac{1}{12}\pi h\delta^6 \end{bmatrix} \tag{4.24}$$

The unknown coefficient matrix ***a*** can be expressed as:

$$[a] = \begin{bmatrix} a_{10}^{10} & a_{10}^{01} & a_{10}^{20} & a_{10}^{02} & a_{10}^{11} \\ a_{01}^{10} & a_{01}^{01} & a_{01}^{20} & a_{01}^{02} & a_{01}^{11} \\ a_{20}^{10} & a_{20}^{01} & a_{20}^{20} & a_{20}^{02} & a_{20}^{11} \\ a_{02}^{10} & a_{02}^{01} & a_{02}^{20} & a_{02}^{02} & a_{02}^{11} \\ a_{11}^{10} & a_{11}^{01} & a_{11}^{20} & a_{11}^{02} & a_{11}^{11} \end{bmatrix} \tag{4.25}$$

According to Eq. (4.20), the relationship between the elements of the shape coefficient matrix ***A***, unknown coefficient matrix ***a*** and known coefficient matrix ***b*** can be expressed as:

$$A_{(10)(10)}a_{10}^{10} = b_{10}^{10} \tag{4.26a}$$

$$A_{(01)(01)}a_{01}^{01} = b_{01}^{01} \tag{4.26b}$$

$$A_{(20)(02)}a_{20}^{20} + A_{(20)(02)}a_{02}^{20} = b_{20}^{20} \tag{4.26c}$$

$$A_{(02)(20)}a_{20}^{02} + A_{(02)(02)}a_{02}^{02} = b_{02}^{02} \tag{4.26d}$$

$$A_{(11)(11)}a_{11}^{11} = b_{11}^{11} \tag{4.26e}$$

According to Eq. (4.22), the known coefficient matrix ***b*** can be expressed as:

$$[b] = \begin{bmatrix} b_{10}^{10} & 0 & 0 & 0 & 0 \\ 0 & b_{01}^{01} & 0 & 0 & 0 \\ 0 & 0 & b_{20}^{20} & 0 & 0 \\ 0 & 0 & 0 & b_{02}^{02} & 0 \\ 0 & 0 & 0 & 0 & b_{11}^{11} \end{bmatrix} = \begin{bmatrix} 1 & 0 & 0 & 0 & 0 \\ 0 & 1 & 0 & 0 & 0 \\ 0 & 0 & 2 & 0 & 0 \\ 0 & 0 & 0 & 2 & 0 \\ 0 & 0 & 0 & 0 & 1 \end{bmatrix} \tag{4.27}$$

Hence, substituting Eq. (4.24) and Eq. (4.27) into Eq. (4.26), the unknown coefficient matrix ***a*** can be obtained as:

$$[a]=\begin{bmatrix} \frac{2}{\pi h\delta^4} & 0 & 0 & 0 & 0 \\ 0 & \frac{2}{\pi h\delta^4} & 0 & 0 & 0 \\ 0 & 0 & \frac{9}{\pi h\delta^6} & -\frac{3}{\pi h\delta^6} & 0 \\ 0 & 0 & -\frac{3}{\pi h\delta^6} & \frac{9}{\pi h\delta^6} & 0 \\ 0 & 0 & 0 & 0 & \frac{12}{\pi h\delta^6} \end{bmatrix} \tag{4.28}$$

Substituting Eq. (4.28) back to Eq. (4.19), the two dimensional peridynamic function can be calculated as:

$$g_2^{10}\left(\vec{\xi}\right)=\frac{2}{\pi h\left|\vec{\xi}\right|\delta^2}\cos\theta \tag{4.29a}$$

$$g_2^{01}\left(\vec{\xi}\right)=\frac{2}{\pi h\left|\vec{\xi}\right|\delta^2}\sin\theta \tag{4.29b}$$

$$g_2^{20}\left(\vec{\xi}\right)=\frac{9}{\pi h\left|\vec{\xi}\right|\delta^3}\cos^2\theta-\frac{3}{\pi h\left|\vec{\xi}\right|\delta^3}\sin^2\theta \tag{4.29c}$$

$$g_2^{02}\left(\vec{\xi}\right)=-\frac{3}{\pi h\left|\vec{\xi}\right|\delta^3}\cos^2\theta+\frac{9}{\pi h\left|\vec{\xi}\right|\delta^3}\sin^2\theta \tag{4.29d}$$

$$g_2^{11}\left(\vec{\xi}\right)=\frac{12}{\pi h\left|\vec{\xi}\right|\delta^3}\cos\theta\sin\theta \tag{4.29e}$$

where θ is the angle between bond and horizontal axis. By substituting Eqs. (4.29) into Eq. (4.18), the two dimensional partial derivatives in both first and second order can be calculated.

4.2.3 Three-dimensional peridynamic differential operator

Similar to one-dimensional and two-dimensional PDO, the three-dimensional PDO can also be derived from Taylor Series. The three-dimensional Taylor Series can be expressed as:

$$f\left(\vec{x}_j\right)=f\left(\vec{x}_i\right)+\xi_1\frac{\partial f\left(\vec{x}_i\right)}{\partial x_1}+\xi_2\frac{\partial f\left(\vec{x}_i\right)}{\partial x_2}+\xi_3\frac{\partial f\left(\vec{x}_i\right)}{\partial x_3}+\frac{1}{2!}\frac{\partial^2 f\left(\vec{x}_i\right)}{\partial x_1^2}+\frac{1}{2!}\frac{\partial^2 f\left(\vec{x}_i\right)}{\partial x_2^2}+$$
$$\frac{1}{2!}\frac{\partial^2 f\left(\vec{x}_i\right)}{\partial x_3^2}+\xi_1\xi_2\frac{\partial^2 f\left(\vec{x}_i\right)}{\partial x_1\partial x_2}+\xi_1\xi_3\frac{\partial^2 f\left(\vec{x}_i\right)}{\partial x_1\partial x_3}+\xi_2\xi_3\frac{\partial^2 f\left(\vec{x}_i\right)}{\partial x_2\partial x_3}+R \tag{4.30}$$

where ξ_3 represents length along z-direction of the bond $\vec{\xi}$ and R is the remainder terms, which is small enough to be neglected. Moving $f\left(\vec{x}_i\right)$ to left hand side, multiplying each term in Eq. (4.30) with a peridynamic function $g_3^{p_1p_2p_3}\left(\vec{\xi}\right)$ and integrating through the horizon of material particle $\boldsymbol{x}$, in which p_1, p_2, p_3 = 0, 1, 2 and can not be equal to 0 at the same time.

$$\int_{Hx}\left(f\left(\vec{x}_j\right)-f\left(\vec{x}_i\right)\right)g_3^{p_1p_2p_3}\left(\vec{\xi}\right)dV=\frac{\partial f\left(\vec{x}_i\right)}{\partial x_1}\int_{Hx}\xi_1 g_3^{p_1p_2p_3}\left(\vec{\xi}\right)dV+\frac{\partial f\left(\vec{x}_i\right)}{\partial x_2}\int_{Hx}\xi_2 g_3^{p_1p_2p_3}\left(\vec{\xi}\right)dV$$
$$+\frac{\partial f\left(\vec{x}_i\right)}{\partial x_3}\int_{Hx}\xi_3 g_3^{p_1p_2p_3}\left(\vec{\xi}\right)dV+\frac{\partial^2 f\left(\vec{x}_i\right)}{\partial x_1^2}\int_{Hx}\frac{1}{2!}\xi_1^2 g_3^{p_1p_2p_3}\left(\vec{\xi}\right)dV+\frac{\partial^2 f\left(\vec{x}_i\right)}{\partial x_2^2}\int_{Hx}\frac{1}{2!}\xi_2^2 g_3^{p_1p_2p_3}\left(\vec{\xi}\right)dV$$
$$+\frac{\partial^2 f\left(\vec{x}_i\right)}{\partial x_3^2}\int_{Hx}\frac{1}{2!}\xi_2^2 g_3^{p_1p_2p_3}\left(\vec{\xi}\right)dV+\frac{\partial^2 f\left(\vec{x}_i\right)}{\partial x_1\partial x_2}\int_{Hx}\xi_1\xi_2 g_3^{p_1p_2p_3}\left(\vec{\xi}\right)dV$$
$$+\frac{\partial^2 f\left(\vec{x}_i\right)}{\partial x_1\partial x_3}\int_{Hx}\xi_1\xi_3 g_3^{p_1p_2p_3}\left(\vec{\xi}\right)dV+\frac{\partial^2 f\left(\vec{x}_i\right)}{\partial x_2\partial x_3}\int_{Hx}\xi_2\xi_3 g_3^{p_1p_2p_3}\left(\vec{\xi}\right)dV \tag{4.31}$$

The orthogonality property of peridynamic functions $g_3^{p_1p_2p_3}\left(\vec{\xi}\right)$ can be written as:

$$\frac{1}{n_1!n_2!n_3!}\int_{H_x}\xi_1^{n_1}\xi_2^{n_2}\xi_3^{n_3}g_2^{p_1p_2p_3}\left(\vec{\xi}\right)dV=\delta_{n_1p_1}\delta_{n_2p_2}\delta_{n_3p_3} \tag{4.32}$$

where n_1, n_2, n_3 = 0, 1, 2 and δ represents the Kronecker Delta. Substituting Eq. (4.32) into Eq. (4.31), the relationships between partial derivatives and peridynamic functions $g_3^{p_1p_2p_3}\left(\xi\right)$ can be expressed as:

$$\begin{Bmatrix}\frac{\partial f\left(\vec{x}_i\right)}{\partial x_1}\\ \frac{\partial f\left(\vec{x}_i\right)}{\partial x_2}\\ \frac{\partial f\left(\vec{x}_i\right)}{\partial x_3}\\ \frac{\partial^2 f\left(\vec{x}_i\right)}{\partial x_1^2}\\ \frac{\partial^2 f\left(\vec{x}_i\right)}{\partial x_2^2}\\ \frac{\partial^2 f\left(\vec{x}_i\right)}{\partial x_3^2}\\ \frac{\partial^2 f\left(\vec{x}_i\right)}{\partial x_1\partial x_2}\\ \frac{\partial^2 f\left(\vec{x}_i\right)}{\partial x_1\partial x_3}\\ \frac{\partial^2 f\left(\vec{x}_i\right)}{\partial x_2\partial x_3}\end{Bmatrix}=\int_{Hx}\left(f\left(\vec{x}_j\right)-f\left(\vec{x}_i\right)\right)\begin{Bmatrix}g_3^{100}\\ g_3^{010}\\ g_3^{001}\\ g_3^{200}\\ g_3^{020}\\ g_3^{002}\\ g_3^{110}\\ g_3^{101}\\ g_3^{011}\end{Bmatrix}dV \tag{4.33}$$

In Eq. (4.33), the peridynamic functions $g_3^{p_1p_2p_3}\left(\vec{\xi}\right)$ can be constructed by:

$$
\begin{aligned}
g_3^{p_1p_2p_3}\left(\vec{\xi}\right) &= a_{100}^{p_1p_2p_3}\omega_{100}\left(\left|\vec{\xi}\right|\right)\xi_1 + a_{010}^{p_1p_2p_3}\omega_{010}\left(\left|\vec{\xi}\right|\right)\xi_2 + a_{001}^{p_1p_2p_3}\omega_{001}\left(\left|\vec{\xi}\right|\right)\xi_3 \\
&+ a_{200}^{p_1p_2p_3}\omega_{200}\left(\left|\vec{\xi}\right|\right)\xi_1^2 + a_{020}^{p_1p_2p_3}\omega_{020}\left(\left|\vec{\xi}\right|\right)\xi_2^2 + a_{002}^{p_1p_2p_3}\omega_{002}\left(\left|\vec{\xi}\right|\right)\xi_3^2 \\
&+ a_{110}^{p_1p_2p_3}\omega_{110}\left(\left|\vec{\xi}\right|\right)\xi_1\xi_2 + a_{101}^{p_1p_2p_3}\omega_{101}\left(\left|\vec{\xi}\right|\right)\xi_1\xi_3 + a_{011}^{p_1p_2p_3}\omega_{011}\left(\left|\vec{\xi}\right|\right)\xi_2\xi_3
\end{aligned}
\tag{4.34}
$$

The weight function $\omega_{\boldsymbol{q_1q_2q_3}}\left(\left|\vec{\xi}\right|\right)$ can be expressed as:

$$
\omega_{\boldsymbol{q_1q_2q_3}}\left(\left|\vec{\xi}\right|\right) = \left(\frac{\delta}{\left|\vec{\xi}\right|}\right)^{\boldsymbol{q_1+q_2+q_3+1}} \tag{4.35}
$$

where q_1, q_2, q_3 = 0, 1, 2 and they can not be equal to zero at the same time. As shown in Eq. (4.34) the peridynamic functions $g_3^{p_1p_2p_3}\left(\vec{\xi}\right)$ is composed of elements of unknown coefficient matrix ***a***, weight function $\boldsymbol{\omega}$ and bond length in *x*, *y* and *z* directions. The unknown coefficient matrix ***a*** can be derived from peridynamic shape matrix ***A*** and known coefficient matrix ***b*** as:

$$
\sum_{q_1=0}^{2}\sum_{q_2=0}^{2-q_1}\sum_{q_3=0}^{2-q_1-q_2} A_{(n_1n_2n_3)(q_1q_2q_3)}a_{q_1q_2q_3}^{p_1p_2p_3} = b_{n_1n_2n_3}^{p_1p_2p_3} \tag{4.36}
$$

In which q_1, q_2, q_3 = 0, 1, 2 and can not equal to 0 at same time. The elements in peridynamic shape matrix ***A*** can be expressed as:

$$
\boldsymbol{A}_{(\boldsymbol{n_1n_2n_3})(\boldsymbol{q_1q_2q_3})} = \int_{\boldsymbol{Hx}} \omega_{\boldsymbol{q_1q_2q_3}}\left(\left|\vec{\xi}\right|\right)\xi_1^{n_1+q_2}\xi_2^{n_2+q_2}\xi_3^{n_3+q_3}dV \tag{4.37}
$$

Hence, by substituting Eq. (4.35) into Eq. (4.37), the peridynamic shape matrix ***A*** can be written as:

$$A=\begin{bmatrix}
\frac{4}{9}\pi\delta^5 & 0 & 0 & 0 & 0 & 0 & 0 & 0 & 0 \\
0 & \frac{4}{9}\pi\delta^5 & 0 & 0 & 0 & 0 & 0 & 0 & 0 \\
0 & 0 & \frac{4}{9}\pi\delta^5 & 0 & 0 & 0 & 0 & 0 & 0 \\
0 & 0 & 0 & \frac{1}{5}\pi\delta^7 & \frac{1}{15}\pi\delta^7 & \frac{1}{15}\pi\delta^7 & 0 & 0 & 0 \\
0 & 0 & 0 & \frac{1}{15}\pi\delta^7 & \frac{1}{5}\pi\delta^7 & \frac{1}{15}\pi\delta^7 & 0 & 0 & 0 \\
0 & 0 & 0 & \frac{1}{15}\pi\delta^7 & \frac{1}{15}\pi\delta^7 & \frac{1}{5}\pi\delta^7 & 0 & 0 & 0 \\
0 & 0 & 0 & 0 & 0 & 0 & \frac{1}{15}\pi\delta^7 & 0 & 0 \\
0 & 0 & 0 & 0 & 0 & 0 & 0 & \frac{1}{15}\pi\delta^7 & 0 \\
0 & 0 & 0 & 0 & 0 & 0 & 0 & 0 & \frac{1}{15}\pi\delta^7
\end{bmatrix} \tag{4.38}$$

The elements of known matrix ***b*** can be expressed as:

$$b_{n_1n_2n_3}^{p_1p_2p_3}=n_1!n_2!n_3!\delta_{n_1p_1}\delta_{n_2p_2}\delta_{n_3p_3} \tag{4.39}$$

Hence, the known coefficient matrix ***b*** can be written as:

$$b=\begin{bmatrix}
1 & 0 & 0 & 0 & 0 & 0 & 0 & 0 & 0 \\
0 & 1 & 0 & 0 & 0 & 0 & 0 & 0 & 0 \\
0 & 0 & 1 & 0 & 0 & 0 & 0 & 0 & 0 \\
0 & 0 & 0 & 2 & 0 & 0 & 0 & 0 & 0 \\
0 & 0 & 0 & 0 & 2 & 0 & 0 & 0 & 0 \\
0 & 0 & 0 & 0 & 0 & 2 & 0 & 0 & 0 \\
0 & 0 & 0 & 0 & 0 & 0 & 1 & 0 & 0 \\
0 & 0 & 0 & 0 & 0 & 0 & 0 & 1 & 0 \\
0 & 0 & 0 & 0 & 0 & 0 & 0 & 0 & 1
\end{bmatrix} \tag{4.40}$$

Substituting Eq. (4.38) and Eq. (4.40) into Eq. (4.36), the unknown coefficient matrix ***a*** can be calculated as:

$$a=\begin{bmatrix} \frac{9}{4\pi\delta^5} & 0 & 0 & 0 & 0 & 0 & 0 & 0 & 0 \\ 0 & \frac{9}{4\pi\delta^5} & 0 & 0 & 0 & 0 & 0 & 0 & 0 \\ 0 & 0 & \frac{9}{4\pi\delta^5} & 0 & 0 & 0 & 0 & 0 & 0 \\ 0 & 0 & 0 & \frac{12}{\pi\delta^7} & \frac{-3}{\pi\delta^7} & \frac{-3}{\pi\delta^7} & 0 & 0 & 0 \\ 0 & 0 & 0 & \frac{-3}{\pi\delta^7} & \frac{12}{\pi\delta^7} & \frac{-3}{\pi\delta^7} & 0 & 0 & 0 \\ 0 & 0 & 0 & \frac{-3}{\pi\delta^7} & \frac{-3}{\pi\delta^7} & \frac{12}{\pi\delta^7} & 0 & 0 & 0 \\ 0 & 0 & 0 & 0 & 0 & 0 & \frac{15}{\pi\delta^7} & 0 & 0 \\ 0 & 0 & 0 & 0 & 0 & 0 & 0 & \frac{15}{\pi\delta^7} & 0 \\ 0 & 0 & 0 & 0 & 0 & 0 & 0 & 0 & \frac{15}{\pi\delta^7} \end{bmatrix} \tag{4.41}$$

By substituting Eq. (4.41) and Eq. (4.35) into Eq. (4.34), the three-dimension peridynamic functions, $g_3^{p_1p_2p_3}(\xi)$, can be calculated as:

$$g_3^{100}=\frac{9}{4\pi\delta^3}\frac{1}{|\vec{\xi}|}\sin\theta\cos\phi \tag{4.42a}$$

$$g_3^{010}=\frac{9}{4\pi\delta^3}\frac{1}{|\vec{\xi}|}\sin\theta\sin\phi \tag{4.42b}$$

$$g_3^{001}=\frac{9}{4\pi\delta^3}\frac{1}{|\vec{\xi}|}\cos\theta \tag{4.42c}$$

$$g_3^{200}=\frac{12}{\pi\delta^4}\frac{1}{|\vec{\xi}|}\sin^2\theta\cos^2\phi-\frac{3}{\pi\delta^4}\frac{1}{|\vec{\xi}|}\sin^2\theta\sin^2\phi-\frac{3}{\pi\delta^4}\frac{1}{|\vec{\xi}|}\cos^2\theta \tag{4.42d}$$

$$g_3^{020} = \frac{-3}{\pi\delta^4}\frac{1}{|\vec{\xi}|}\sin^2\theta\cos^2\phi + \frac{12}{\pi\delta^4}\frac{1}{|\vec{\xi}|}\sin^2\theta\sin^2\phi - \frac{3}{\pi\delta^4}\frac{1}{|\vec{\xi}|}\cos^2\theta \tag{4.42e}$$

$$g_3^{002} = \frac{-3}{\pi\delta^4}\frac{1}{|\vec{\xi}|}\sin^2\theta\cos^2\phi - \frac{3}{\pi\delta^4}\frac{1}{|\vec{\xi}|}\sin^2\theta\sin^2\phi + \frac{12}{\pi\delta^4}\frac{1}{|\vec{\xi}|}\cos^2\theta \tag{4.42f}$$

$$g_3^{110} = \frac{15}{\pi\delta^4}\frac{1}{|\vec{\xi}|}\sin^2\theta\cos\phi\sin\phi \tag{4.42g}$$

$$g_3^{101} = \frac{15}{\pi\delta^4}\frac{1}{|\vec{\xi}|}\sin\theta\cos\theta\cos\phi \tag{4.42h}$$

$$g_3^{011} = \frac{15}{\pi\delta^4}\frac{1}{|\vec{\xi}|}\sin\theta\cos\theta\sin\phi \tag{4.42i}$$

where θ refers to the angle between bond and z axis. ϕ represents the angle between the projection of bond on x-y plane and x axis as shown in Fig. 4.1. Substituting Eqs. (4.42) into Eq. (4.33), the three-dimensional partial derivatives can be calculated.

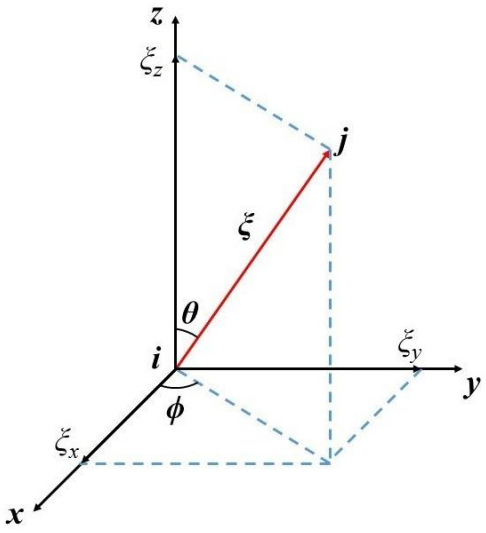

Figure 4.1. Three dimensional bond orientation

4.3 Transforming CCM equations to PD equations by using peridynamic differential operator

The basic information of PDO has been provided in section 4.2. By applying the concept of "Horizon", the PDEs can be transformed into spatial integral equations. Hence, the limitation of PDEs in describing discontinuous problem can be overcome. In order to validate the reliability of PDO, the convergence studies of PD to the CCM in three dimensions are shown in the following sections.

4.3.1 One-dimensional formulation

Based on Hooke's Law, the one-dimensional stress-strain relationship for linear, isotropic, elastic body, is presented as [74]:

$$\sigma = E\varepsilon = E\frac{\partial u}{\partial x} \tag{4.43}$$

where E refers to the elastic modulus of the material. In CCM the motion of material particles can be described by Newton's Second Law (or equation of motion) as:

$$\rho\ddot{u} = \nabla \cdot \sigma + b \tag{4.44}$$

where u refers to the displacement of material particles and b refers to body force density. Without considering body force for simple calculation and substituting Eq. (4.43) into Eq. (4.44), the equation of motion can be expressed as:

$$\rho\frac{\partial^2 u}{\partial t^2} = E\frac{\partial^2 u}{\partial x^2} \tag{4.45}$$

Eq. (4.45) is the one-dimensional equation of motion based on CCM. The partial differential term in this equation can be replaced by a spatial integral term by considering Eq. (4.5) as:

$$\rho \ddot{u}_i = E \int_{H_x} \left(u_j - u_i \right) g_1^2 dV \tag{4.46}$$

Substituting Eq. (4.14) into Eq. (4.46) and simplifying this equation, we get:

$$\rho \ddot{u}_i = \frac{2E}{A\delta^2} \int_{H_x} \frac{\left(u_j - u_i \right)}{\left| \xi \right|} dV \tag{4.47}$$

Recalling the one-dimensional bond constants in Table 3.1 in Section 3.3.1, Eq. (4.47) becomes:

$$\rho \ddot{u}_i = \int_{H_x} c \frac{\left(u_j - u_i \right)}{\left| \vec{\xi} \right|} dV \tag{4.48}$$

$\frac{\left(u_j - u_i \right)}{\left| \vec{\xi} \right|}$ refers to the stretch of a bond associated with the material points ***i*** and ***j***.

Hence, Eq. (4.48) has recovered the expression of equation of motion in one-dimensional bond-based PD from CCM.

4.3.2 Two-dimensional formulation

Under the plane stress assumptions, the two-dimensional stress-strain relationship for linear, isotropic, elastic body is presented as:

$$\begin{Bmatrix} \sigma_{xx} \\ \sigma_{yy} \\ \tau_{xy} \end{Bmatrix} = \frac{E}{1-\nu^2} \begin{bmatrix} 1 & \nu & 0 \\ \nu & 1 & 0 \\ 0 & 0 & \frac{1-\nu}{2} \end{bmatrix} \begin{Bmatrix} \varepsilon_{xx} \\ \varepsilon_{yy} \\ \gamma_{xy} \end{Bmatrix} \tag{4.49}$$

where E refers to the elastic modulus and ν refers to the Poisson's Ratio. Recalling back Eq. (4.44), the two-dimensional equation of motion based on CCM can be expressed as:

$$\rho\ddot{u}_i = \frac{E}{2(1-\nu)}\left[2\frac{\partial^2 u_i}{\partial x^2} + (1+\nu)\frac{\partial^2 v_i}{\partial x \partial y} + (1-\nu)\frac{\partial^2 u_i}{\partial y^2}\right] \tag{4.50a}$$

$$\rho\ddot{v}_i = \frac{E}{2(1-\nu)}\left[2\frac{\partial^2 v_i}{\partial y^2} + (1+\nu)\frac{\partial^2 u_i}{\partial x \partial y} + (1-\nu)\frac{\partial^2 v_i}{\partial x^2}\right] \tag{4.50b}$$

The PDEs in Eqs. (4.51) can be replaced by spatial integral equations as shown in Eq. (4.18). Substituting Eqs. (4.29) and Eq. (4.18) into Eqs. (4.51), the equations of motion can be rewritten as:

$$\rho\ddot{u}_i = \frac{E}{2(1-\nu^2)}\frac{3}{\pi h\delta^3}\begin{pmatrix} 2\int_0^\delta\int_0^{2\pi}\frac{u_j-u_i}{|\xi|}\left(3\cos^2\theta-\sin^2\theta\right)h\xi d\xi d\theta + \\ (1+\nu)\int_0^\delta\int_0^{2\pi}\frac{v_j-v_i}{|\xi|}4\cos\theta\sin\theta h\xi d\xi d\theta + \\ (1-\nu)\int_0^\delta\int_0^{2\pi}\frac{u_j-u_i}{|\xi|}\left(3\sin^2\theta-\cos^2\theta\right)h\xi d\xi d\theta \end{pmatrix} \tag{4.51a}$$

$$\rho\ddot{v}_i = \frac{E}{2(1-\nu^2)}\frac{3}{\pi h\delta^3}\begin{pmatrix} 2\int_0^\delta\int_0^{2\pi}\frac{v_j-v_i}{|\xi|}\left(-\cos^2\theta+3\sin^2\theta\right)h\xi d\xi d\theta + \\ (1+\nu)\int_0^\delta\int_0^{2\pi}\frac{u_j-u_i}{|\xi|}4\cos\theta\sin\theta h\xi d\xi d\theta + \\ (1-\nu)\int_0^\delta\int_0^{2\pi}\frac{v_j-v_i}{|\xi|}\left(-\sin^2\theta+3\cos^2\theta\right)h\xi d\xi d\theta \end{pmatrix} \tag{4.51b}$$

After simplification, Eq. (4.51a) and Eq. (4.51b) can be expressed as:

$$\rho\ddot{u}_i = \frac{E}{2(1-\nu^2)}\frac{3}{\pi h\delta^3}\begin{pmatrix} \int_0^\delta\int_0^{2\pi}\frac{u_j-u_i}{|\xi|}\left((5+\nu)\cos^2\theta+(1-3\nu)\sin^2\theta\right)+ \\ 4(1+\nu)\frac{v_j-v_i}{|\xi|}\cos\theta\sin\theta \end{pmatrix} h\xi d\xi d\theta \tag{4.51c}$$

$$\rho\ddot{v}_i = \frac{E}{2\left(1-\nu^2\right)}\frac{3}{\pi h\delta^3}\left(\begin{array}{l}\int_0^{\delta}\int_0^{2\pi}\frac{v_j - v_i}{|\xi|}\left(\left(5+\nu\right)\cos^2\theta+\left(1-3\nu\right)\sin^2\theta\right)+\\ 4\left(1+\nu\right)\frac{u_j-u_i}{|\xi|}\cos\theta\sin\theta\end{array}\right)h\xi d\xi d\theta$$

(4.51d)

where *h* refers to the two-dimensional plate thickness. If we assume the Poisson's Ratio is 1/3, the Eqs. (4.51) can be reformed as:

$$\rho\ddot{u}_i = \frac{9E}{\pi\delta^3}\left(\int_0^{\delta}\int_0^{2\pi}\frac{\left(u_j-u_i\right)\cos^2\theta+\left(v_j-v_i\right)\cos\theta\sin\theta}{|\xi|}\right)\xi d\xi d\theta \tag{4.52a}$$

$$\rho\ddot{v}_i = \frac{9E}{\pi\delta^3}\left(\int_0^{\delta}\int_0^{2\pi}\frac{\left(v_j-v_i\right)\sin^2\theta+\left(u_j-u_i\right)\cos\theta\sin\theta}{|\xi|}\right)\xi d\xi d\theta \tag{4.52b}$$

For two-dimensional isotropic plate, the equation of motion expressed by bond-based PD is:

$$\rho\ddot{u}_i = h\left(\int_0^{\delta}\int_0^{2\pi}\frac{c\left(\left(u_j-u_i\right)\cos^2\theta+\left(v_j-v_i\right)\cos\theta\sin\theta\right)}{|\xi|}\right)\xi d\xi d\theta \tag{4.53a}$$

$$\rho\ddot{v}_i = h\left(\int_0^{\delta}\int_0^{2\pi}\frac{c\left(\left(v_j-v_i\right)\sin^2\theta+\left(u_j-u_i\right)\cos\theta\sin\theta\right)}{|\xi|}\right)\xi d\xi d\theta \tag{4,53b}$$

By comparing Eqs. (4.53) with Eqs. (4.52), we can find out that

$$c = \frac{9E}{\pi h\delta^3} \text{ and } \nu = \frac{1}{3} \tag{4.54}$$

which matches with the bond constant in Table. 3.1. Hence, Eqs. (4.50) transforms to the equation of motion of two-dimensional bond-based PD by using PDO.

4.3.3 Three-dimensional formulation

Recalling the stress-strain relationship for three-dimensional linear, isotropic, elastic body as:

$$\begin{Bmatrix} \sigma_{xx} \\ \sigma_{yy} \\ \sigma_{zz} \\ \sigma_{xy} \\ \sigma_{xz} \\ \sigma_{yz} \end{Bmatrix} = \frac{E}{(1+\nu)(1-2\nu)} \begin{bmatrix} 1-\nu & \nu & \nu & 0 & 0 & 0 \\ \nu & 1-\nu & \nu & 0 & 0 & 0 \\ \nu & \nu & 1-\nu & 0 & 0 & 0 \\ 0 & 0 & 0 & \frac{1-2\nu}{2} & 0 & 0 \\ 0 & 0 & 0 & 0 & \frac{1-2\nu}{2} & 0 \\ 0 & 0 & 0 & 0 & 0 & \frac{1-2\nu}{2} \end{bmatrix} \begin{Bmatrix} \varepsilon_{xx} \\ \varepsilon_{yy} \\ \varepsilon_{zz} \\ 2\varepsilon_{xy} \\ 2\varepsilon_{xz} \\ 2\varepsilon_{yz} \end{Bmatrix} \tag{4.55}$$

The equations of motion for three-dimensional material particles based on CCM without considering body force for simple calculation are shown as:

$$\rho \frac{\partial^2 u}{\partial t^2} = \frac{\partial \sigma_{xx}}{\partial x} + \frac{\partial \sigma_{xy}}{\partial y} + \frac{\partial \sigma_{xz}}{\partial z} \tag{4.56a}$$

$$\rho \frac{\partial^2 v}{\partial t^2} = \frac{\partial \sigma_{yx}}{\partial x} + \frac{\partial \sigma_{yy}}{\partial y} + \frac{\partial \sigma_{yz}}{\partial z} \tag{4.56b}$$

$$\rho \frac{\partial^2 w}{\partial t^2} = \frac{\partial \sigma_{zx}}{\partial x} + \frac{\partial \sigma_{zy}}{\partial y} + \frac{\partial \sigma_{zz}}{\partial z} \tag{4.56c}$$

Substituting Eq. (4.55) into Eqs. (4.56), the equation of motion can be rewritten in terms of displacement component as:

$$\rho \ddot{u}_i = \frac{E}{(1+\nu)(1-2\nu)} \left[(1-\nu) \frac{\partial^2 u_i}{\partial x^2} + \frac{1-2\nu}{2} \frac{\partial^2 u_i}{\partial y^2} + \frac{1-2\nu}{2} \frac{\partial^2 u_i}{\partial z^2} + \frac{1}{2} \frac{\partial^2 v_i}{\partial x \partial y} + \frac{1}{2} \frac{\partial^2 w_i}{\partial x \partial z} \right]$$

(4.57a)

$$\rho\ddot{v}_i = \frac{E}{(1+\nu)(1-2\nu)}\left[\frac{1-2\nu}{2}\frac{\partial^2 v_i}{\partial x^2} + (1-\nu)\frac{\partial^2 v_i}{\partial y^2} + \frac{1-2\nu}{2}\frac{\partial^2 v_i}{\partial z^2} + \frac{1}{2}\frac{\partial^2 u_i}{\partial x \partial y} + \frac{1}{2}\frac{\partial^2 w_i}{\partial y \partial z}\right]$$

(4.57b)

$$\rho\ddot{w}_i = \frac{E}{(1+\nu)(1-2\nu)}\left[\frac{1-2\nu}{2}\frac{\partial^2 w_i}{\partial x^2} + \frac{1-2\nu}{2}\frac{\partial^2 w_i}{\partial y^2} + (1-\nu)\frac{\partial^2 w_i}{\partial z^2} + \frac{1}{2}\frac{\partial^2 u_i}{\partial x \partial z} + \frac{1}{2}\frac{\partial^2 v_i}{\partial y \partial z}\right]$$

(4.57c)

The partial derivatives in Eqs. (4.57) can be replaced by spatial integral equation as shown in Eq. (4.33). Therefore the equation of motion can be reformed as:

$$\rho\ddot{u}_i = \frac{E}{(1+\nu)(1-2\nu)}$$
$$\left[\begin{array}{l}(1-\nu)\int_{H_x}(u_j-u_i)g_3^{200}dV + \frac{1-2\nu}{2}\int_{H_x}(u_j-u_i)g_3^{020}dV + \frac{1-2\nu}{2}\int_{H_x}(u_j-u_i)g_3^{002}dV \\ +\frac{1}{2}\int_{H_x}(v_j-v_i)g_3^{110}dV + \frac{1}{2}\int_{H_x}(w_j-w_i)g_3^{101}dV\end{array}\right]$$

(4.58a)

$$\rho\ddot{v}_i = \frac{E}{(1+\nu)(1-2\nu)}$$
$$\left[\begin{array}{l}\frac{1-2\nu}{2}\int_{H_x}(v_j-v_i)g_3^{200}dV + (1-\nu)\int_{H_x}(v_j-v_i)g_3^{020}dV + \frac{1-2\nu}{2}\int_{H_x}(v_j-v_i)g_3^{002}dV \\ +\frac{1}{2}\int_{H_x}(u_j-u_i)g_3^{110}dV + \frac{1}{2}\int_{H_x}(w_j-w_i)g_3^{011}dV\end{array}\right]$$

(4.58b)

$$\rho\ddot{w}_i = \frac{E}{(1+\nu)(1-2\nu)}$$
$$\left[\begin{array}{l} \frac{1-2\nu}{2}\int_{H_x}(w_j-w_i)g_3^{200}dV + \frac{1-2\nu}{2}\int_{H_x}(w_j-w_i)g_3^{020}dV + (1-\nu)\int_{H_x}(w_j-w_i)g_3^{002} \\ +\frac{1}{2}\int_{H_x}(u_j-u_i)g_3^{101}dV + \frac{1}{2}\int_{H_x}(v_j-v_i)g_3^{011}dV \end{array}\right]$$

(4.58c)

Substituting Eqs. (4.43) into Eqs. (4.59), the equations of motion can be rewritten as:

$$\rho\ddot{u}_i = \frac{E}{(1+\nu)(1-2\nu)}$$
$$\left\{\begin{array}{l} \frac{3}{\pi\delta^4}\int_{H_x}\frac{u_j-u_i}{|\vec{\xi}|}\left[(3-2\nu)sin^2\theta cos^2\varphi + \left(\frac{1}{2}-2\nu\right)sin^2\theta sin^2\varphi + \left(\frac{1}{2}-2\nu\right)cos^2\theta\right]dV \\ +\frac{3}{\pi\delta^4}\int_{H_x}\frac{v_j-v_i}{|\vec{\xi}|}\left[\frac{5}{2}sin^2\theta cos\varphi sin\varphi\right]dV + \frac{3}{\pi\delta^4}\int_{Hx}\frac{w_j-w_i}{|\vec{\xi}|}\left[\frac{5}{2}sin\theta cos\theta cos\varphi\right]dV \end{array}\right\}$$

(4.59a)

$$\rho\ddot{v}_i = \frac{E}{(1+\nu)(1-2\nu)}$$
$$\left\{\begin{array}{l} \frac{3}{\pi\delta^4}\int_{H_x}\frac{v_j-v_i}{|\vec{\xi}|}\left[\left(\frac{1}{2}-2\nu\right)\sin^2\theta\cos^2\varphi + (3-2\nu)\sin^2\theta\sin^2\varphi + \left(\frac{1}{2}-2\nu\right)\cos^2\theta\right]dV \\ +\frac{3}{\pi\delta^4}\int_{H_x}\frac{u_j-u_i}{|\vec{\xi}|}\left[\frac{5}{2}\sin^2\theta\cos\varphi\sin\varphi\right]dV + \frac{3}{\pi\delta^4}\int_{H_x}\frac{w_j-w_i}{|\vec{\xi}|}\left[\frac{5}{2}\sin\theta\cos\theta\sin\varphi\right]dV \end{array}\right\}$$

(4.59b)

$$\rho\ddot{w}_i = \frac{E}{(1+\nu)(1-2\nu)}$$
$$\frac{3}{\pi\delta^4}\int_{H_x}\frac{w_j-w_i}{|\vec{\xi}|}\left[\left(\frac{1}{2}-2\nu\right)\sin^2\theta\cos^2\varphi+\left(\frac{1}{2}-2\nu\right)\sin^2\theta\sin^2\varphi+(3-2\nu)\cos^2\theta\right]dV$$
$$+\frac{3}{\pi\delta^4}\int_{H_x}\frac{u_j-u_i}{|\vec{\xi}|}\left[\frac{5}{2}\sin\theta\cos\theta\cos\varphi\right]dV+\frac{3}{\pi\delta^4}\int_{H_x}\frac{v_j-v_i}{|\vec{\xi}|}\left[\frac{5}{2}\sin\theta\cos\theta\sin\varphi\right]dV$$

(4.59c)

If we assume the Poisson's ratio to be 1/4, the equations of motion can be simplified as:

$$\rho\ddot{u}_i = \frac{12E}{\pi\delta^4}\int_{Hx}\frac{(u_j-u_i)sin^2\theta cos^2\varphi+(v_j-v_i)sin^2\theta cos\varphi sin\varphi+(w_j-w_i)sin\theta cos\theta cos\varphi}{|\vec{\xi}|}dV$$

(4.60a)

$$\rho\ddot{v}_i = \frac{12E}{\pi\delta^4}\int_{Hx}\frac{(v_j-v_i)sin^2\theta sin^2\varphi+(u_j-u_i)sin^2\theta cos\varphi sin\varphi+(w_j-w_i)sin\theta cos\theta sin\varphi}{|\vec{\xi}|}dV$$

(4.60b)

$$\rho\ddot{w}_i = \frac{12E}{\pi\delta^4}\int_{Hx}\frac{(w_j-w_i)\cos^2\theta+(u_j-u_i)\sin\theta\cos\theta\cos\varphi+(v_j-v_i)\sin\theta\cos\theta\sin\varphi}{|\vec{\xi}|}dV$$

(4.60c)

Recalling Eq. (3.2), the three-dimensional equations of motion in PD can be shown as:

$$\rho\ddot{u}_i = \int_{Hx} c\frac{(u_j-u_i)sin^2\theta cos^2\varphi+(v_j-v_i)sin^2\theta cos\varphi sin\varphi+(w_j-w_i)sin\theta cos\theta cos\varphi}{|\vec{\xi}|}dV$$

(4.61a)

$$\rho\ddot{v}_i = \int_{Hx} c\frac{\left(v_j - v_i\right)sin^2\theta sin^2\varphi + \left(u_j - u_i\right)sin^2\theta cos\varphi sin\varphi + \left(w_j - w_i\right)sin\theta cos\theta sin\varphi}{\left|\vec{\xi}\right|}dV$$

(4.61b)

$$\rho\ddot{w}_i = \int_{Hx} c\frac{\left(w_j - w_i\right)cos^2\theta + \left(u_j - u_i\right)sin\theta cos\theta cos\varphi + \left(v_j - v_i\right)sin\theta cos\theta sin\varphi}{\left|\vec{\xi}\right|}dV$$

(4.61c)

By comparing Eqs. (4.61) with Eqs. (4.60), the value of *c* can be calculated as:

$$c = \frac{12E}{\pi\delta^4} \text{ with } \nu = \frac{1}{4} \tag{4.62}$$

Eq. (4.62) satisfies the three-dimensional bond constant in Table 3.1 in Section 3.3.1, which means Eqs. (4.57) transforms to the equations of motion in three-dimension bond-based PD by PDO.

4.4 Numerical validation of peridynamic differential operator

For infinitely small discretisation and horizon size, the behaviour described by CCM should converge to those described by peridynamics as shown in Section 4.3. In this section, some numerical applications about PDO are provided. By comparing the results with analytical solutions or FEM solutions, the accuracy of the PDO can be validated.

4.4.1 Numerical validation of 1st order PDEs

Imagine a one-dimensional bar with 2 meter in length as shown in Fig. 4.2. The temperature of the bar varies along the length of the bar with the following relationship:

$$T(x) = 100(x-1)^2 \tag{4.63}$$

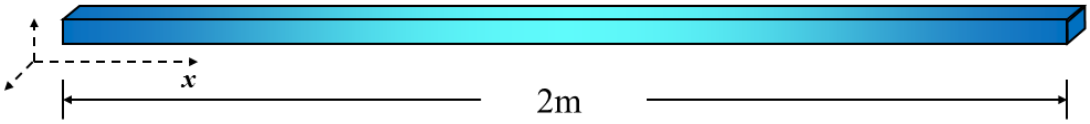

Figure 4.2. One-dimensional bar with varying temperature

where T refers to the temperature and x represents the location along the bar. Then the analytical solution of the temperature gradient on this bar can be expressed as:

$$grad(T) = \frac{\partial T}{\partial x} = 200(x-1) \tag{4.64a}$$

In peridynamics, the bar was uniformly discretised into 100 material particles with a volume of (0.02^3) m^3. The PDE in Eq. (4.54a) can be represented by PDO according to Eq. (4.5) as:

$$grad(T) = \frac{\partial T}{\partial x} = \sum_{j=1}^{n}\left(T_j - T_i\right) g_1^1(\xi) V_j \tag{4.64b}$$

Hence the temperature gradient results by analytical solution and peridynamics are shown in Fig. (4.3):

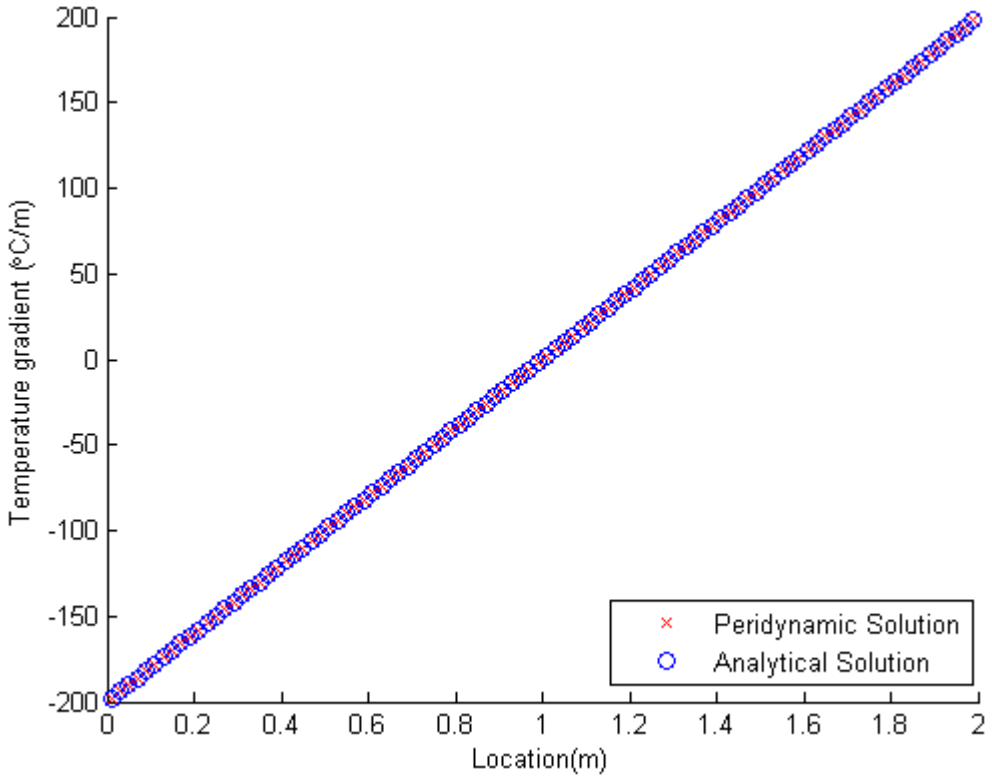

Figure 4.3. Linear temperature gradient along the bar

If the temperature along the bar has a different distribution, such as:

$$T(x) = 100\cos\left(\frac{\pi}{2}x\right) \tag{4.65a}$$

The analytical solution of gradient of temperature can be expressed as:

$$grad(T) = \frac{\partial T}{\partial x} = -50\pi\sin\left(\frac{\pi}{2}x\right) \tag{4.65b}$$

Replacing the PDE by PDO, the gradient of temperature can be shown as:

$$grad(T) = \frac{\partial T}{\partial x} = \sum_{j=1}^{n}\left(T_j - T_i\right)g_1^1(\xi)V_j \tag{4.65c}$$

Hence, the temperature gradient results by analytical solution and peridynamics are shown in Fig. (4.4):

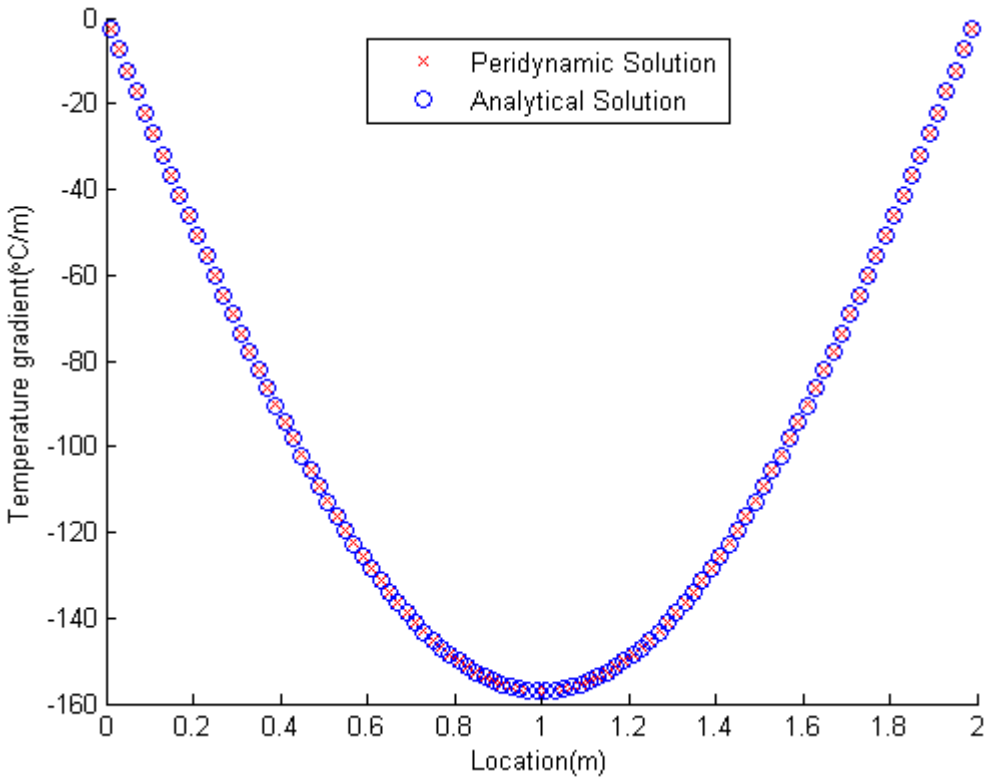

Figure 4.4. Temperature gradient along the bar

The results generated by PDO method are marked as “red cross”, while the results generated by analytical method are marked as “blue circle” The solutions by these two methods has agree very well with each other. Hence, the PDO is reliable in solving 1st order PDEs.

4.4.2 Numerical validation of 2nd order PDEs

In this section, one-dimensional thermal conduction and two-dimensional lithium ion diffusion are taken as examples to validate the accuracy of PDO for 2nd order PDEs. Since both of the simulations are dynamic analysis which require large amount of calculation, it is impractical to get analytical solutions manually. Therefore, in these two cases, two different methods, FEM and PDO method, are

applied to simulate the thermomechanical process. The commercially available software, ANSYS, was used to implement the FEM analysis due to its sophisticated thermal-structural analysis capability. For thermal expansion analysis, 8 nodes coupled thermal mechanical element PLANE223 was selected as element type with plane stress assumption. Peridynamic analysis is performed by using a personal code and calculated by using MATLAB.

Imagine a bar with initial temperature (0 ℃) is subjected to a static temperature loading of 0 ℃ at left end and 100 ℃ at right end. The material properties of the bar are given in Table 4.1.

Table 4.1. Material properties of the bar

Length	Thermal Conductivity	Density	Specific Heat Capacity
L	k	ρ	c_v
(m)	(W/m ℃)	(kg/m^3)	(J/kgK)
2	233	10	3

W/m ℃ (watt per meter per Celsius degree) is the same with corresponding standard SI unit W/mK (watt per meter per Kelvin). In this thesis, the unit of thermal conductivity is W/m ℃ for consistency. The bar structure is meshed/discretised into 100 elements/particles. Different discretisation schemes in both ANSYS and MATLAB are shown in Fig. 4.5. The governing equation of the thermal conduction can be expressed as:

$$\rho c_v \dot{T} = k\nabla^2 T \tag{4.66a}$$

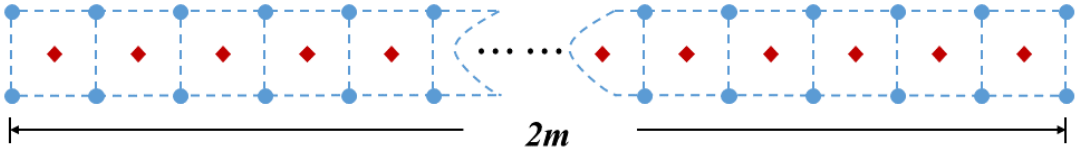

Figure 4.5. Difference in discretisation between FEM and PD: ANSYS discretisation are marked in blue while MATLAB discretisation are marked in red

where ρ is the material density, c_v refers to specific heat capacity and K refers to thermal conductivity. Blue dash-line and dots represent the discretisation in FEM (ANSYS) whereas red dot represents the discretisation by PD. According to Eq. (4.18), Eq. (4.66a) can be reformed as:

$$\rho c_v \dot{T} = k \int_{H_x} \left(T_j - T_i \right) g_2^{20} \left(\vec{\xi} \right) dV \tag{4.66b}$$

Substituting Eqs. (4.29) into Eq. (4.66b), the numerical solution by PDO can be calculated. After 5 seconds of diffusion, the results derived from ANSYS have been exported into MATLAB to provide a clear comparison as shown in Fig. 4.6:

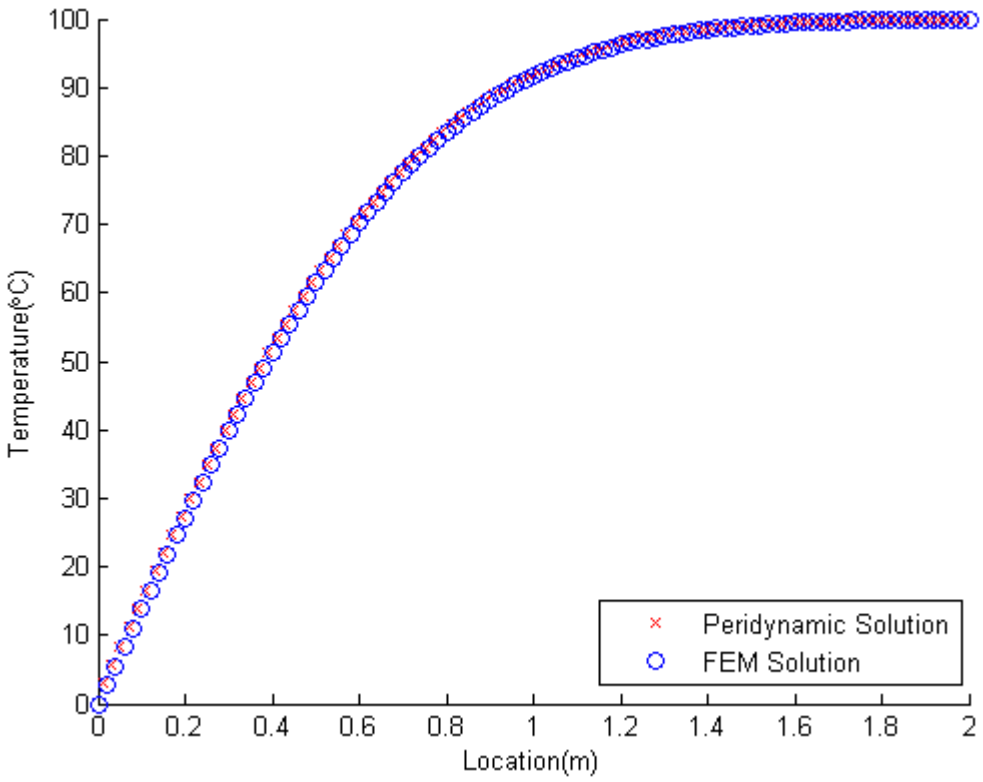

Figure 4.6. Temperature distribution at 5s along the bar

Due to different discretisation methods, there is a minor difference between FEM and PDO method. Overall, the results generated by two methods show good agreement with each other.

For two-dimensional problems, a simulation of lithium-ion diffusion inside a thin plate is provided below as the validation test. Hence, a simple lithium-ion diffusion model is shown in Fig. 4.7 and the governing equation of lithium ion diffusion can be described as:

$$\dot{C} = D\nabla^2 C = D\left(\frac{\partial^2 C}{\partial x^2} + \frac{\partial^2 C}{\partial y^2}\right) \tag{4.67a}$$

where C refers to the lithium ion concentration and D represents the diffusivity of the lithium ion in the plate. Replacing the partial derivatives with integral terms according to Eq. (4.18), Eq. (4.67a) can be rewritten as:

$$\dot{C} = D\nabla^2 C = D\left(\int_{H_x}\left(C_j - C_i\right)g_2^{20}dV + \int_{H_x}\left(C_j - C_i\right)g_2^{02}dV\right) \tag{4.67b}$$

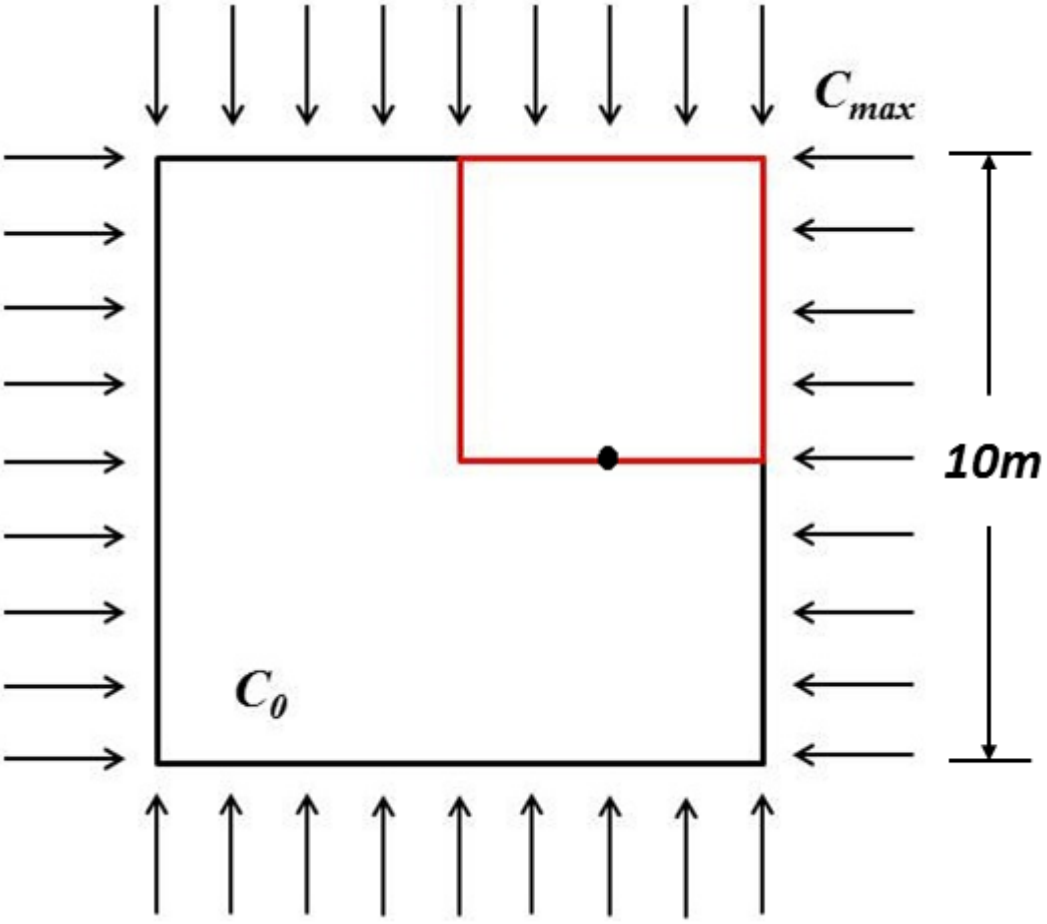

Figure 4.7. Two-dimensional plate

Before the charging process starts, the square plate is free from lithium ions. Therefore, the initial lithium ion concentration of plate is C_0 (0 mol/m^3). Then, the plate is subjected to a maximum lithium ion concentration, C_{max} (0.15 mol/m^3), at all the boundaries of the plate. The material properties of the plate are given in Table 4.2. Similar to the last thermal diffusion validation test, the results from FEM by ANSYS is compared to PDO method by MATLAB in order to validate the accuracy of the simulation.

Table 4.2. Material properties of the plate

Elastic modulus	Poisson's ratio	Coefficient of expansion	Density	Diffusivity
E	v	α	ρ	D
(GPa)		(m^3/mol)	(kg/m^3)	(m^2/s)
200	$\frac{1}{3}$	50×10^{-6}	1	1000

Since the plate geometry and loading conditions are symmetric, only a quarter of the plate is modelled (as shown in red contour in Fig. 4.7). A sample point (black point on red contour) is selected to record the lithium ion concentration change as the time progresses. The results plots during the lithiation process is given in Fig. 4.8.

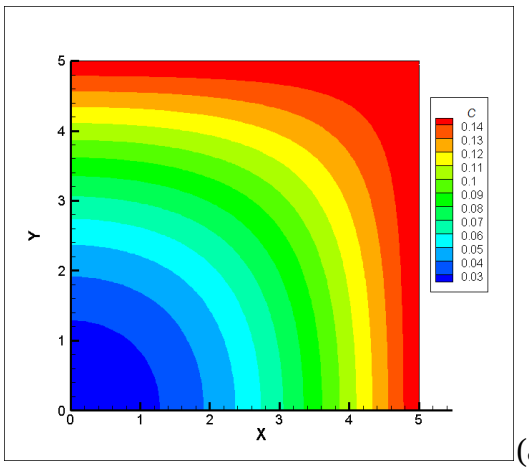

(a)

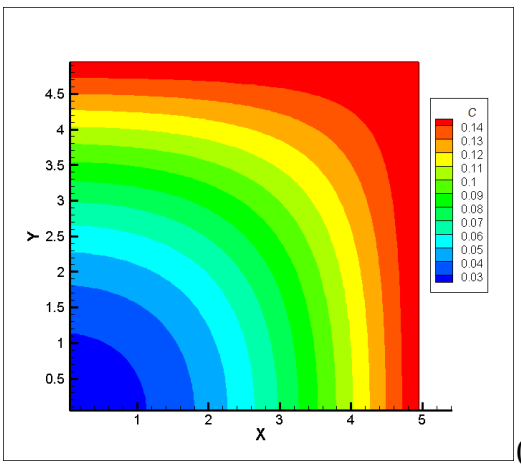

(b)

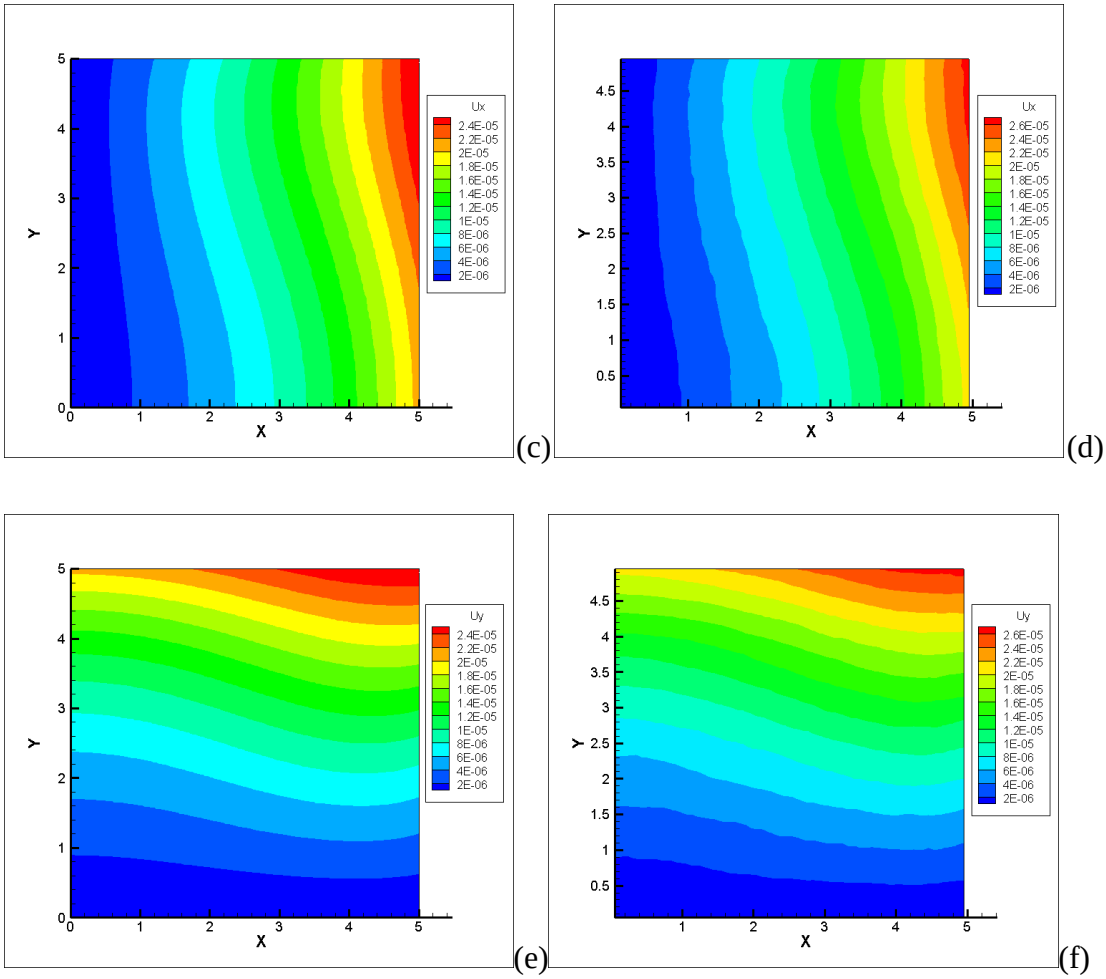

Figure 4.8. Results of thermal expansion: (a) Concentration distribution by FEM (b) Concentration distribution by PD (c) Displacement in *x* direction by FEM (d) Displacement in *x* direction by PD (e) Displacement in *y* direction by FEM (f) Displacement in *y* direction by PD

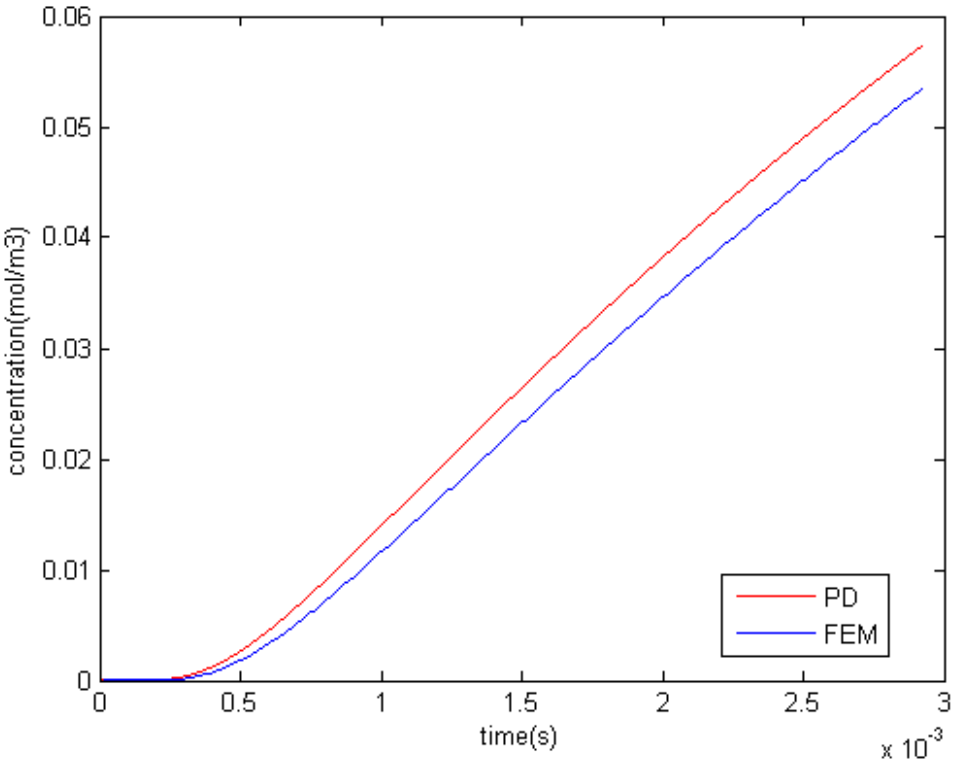

Figure 4.9. Time history of lithium-ion concentration on sample point

After the diffusion process for 2.92×10^{-3} seconds, the plate starts to expand from boundary region in both *x* and *y* direction. However, the central region remains undeformed. Maximum of displacements in FEM are 2.45e-5 meter and 2.45e-5 meter in x and y direction respectively, while maximum of displacements in PD are 2.65e-5 meter and 2.65e-5 meter in x and y direction respectively. The displacement fields and lithium ion concentration field in Fig. 4.8 show a good agreement between FEM and PD method. The lithium-ion concentration on sample point starts increasing at 0.25×10^{-3} second and reaches 0.0572 mol/m^3. Unlike the FEM, there is no material point locates on the contour in the discretisation of PD. Therefore, the material point next to the sample point is selected. Moreover, the FEM uses the implicit time integration scheme while the PD applies the explicit time integration scheme in numerical calculations. Hence, the results show a minor gap between these two methods in Fig. 4.8 and Fig. 4.9.

4.5 Summary

As a useful tool in solving the PDEs, PDO, is introduced in this chapter. In section 4.3, the equations of motion by CCM converge to bond-based peridynamics by applying PDO. In section 4.4, it was shown that the PDO method has a good accuracy in solving PDEs. The PDO uses the concept of "Horizon". Unlike traditional methods in solving PDEs, such as FEM, FVM and FDM, the material points are influenced by the situation of its horizon members in PDO method. Since the PDEs have transformed into spatial integral equations, there is no limitation in solving problems with non-continuous material structures such as cracks and kinks. Besides, the material properties, such as thermal conductivity and ion diffusivity, can be directly applied to numerical simulations without transferring into micro-diffusivity as in bond-based PD as shown in chapter 3. In following numerical simulations, the PDO is applied along with the bond-based PD.

5 THERMOMECHANICAL FRACTURE ANALYSIS

5.1 Introduction

In this chapter, the coupled field thermomechanical model of SOFC based on bond-based PD is presented. An anode plate specimen is selected in the simulation, which is derived from [12] in the literature. The anode plate is mixed with electrolyte material in order to increase the TPBs. As a result, the efficiency of the electrochemical reaction increases. In this study, a bond-based peridynamic model is applied to describe the thermomechanical deformation of the anode plate. Based on the Fourier's Law, a coupled field equation of motion in bond-based PD is created with the help of PDO. Moreover, a FEM model is also built by ANSYS as a comparison to the PD.

5.2 Background

Reversing water electrolysis process can be regarded as the basic principle of fuel cell, which is discovered by William Grove [88]. Based on his discovery, Grove developed an improved wet-cell battery, known as "Grove cell", in 1838 [89]. Electrolyte, as an ion conductor in the battery system, is under discussion in the past and the researches about the state of the electrolyte last around 100 years. In 1897, Nernst developed a thin rod shape solid electrolyte [90]. With the help of an auxiliary heating appliance, the ion transferring can be implemented in the solid state electrolyte by continuously glowing the device. He pointed out that mixture oxides have enormous high conductivity as compare with pure oxides under elevated temperatures. The solid state electrolyte was applied on the Nernst lamp as the electric conductor. After verifying the experimental results and analytical results, Haber applied the first patent on fuel cell with solid electrolyte in 1905 [91]. The performance of the electrodes and electrolyte were under excessive investigation

after the invention of SOFC. Tradewell built up a fuel cell with silver/oxygen electrode and quartz/porcelain electrolyte in 1916 [92]. He found out the decomposition of the metal oxides on the electrode under 1000 ℃ operating temperature. However, massive efforts were conducted to find the suitable candidates for electrodes and electrolyte, but the outcome was far from satisfactory until 1950s [93]. Due to the development of photoacoustic technique, the investigation of SOFC becomes more meticulous and accurate. In late 1950s, many research activities were established around the world in solid state electrochemistry [94], [95]. In these researches, metal oxides (such as ZrO_2) based electrolyte became the popular candidate materials. Due to the exploration of outer space in 1960s, the SOFCs were widely applied in the spaceships [96]. In 1970s, numerous researches about the ion conductivity and stability of the electrolyte and electrodes were set up and it is difficult to cite all the achievements in this section.

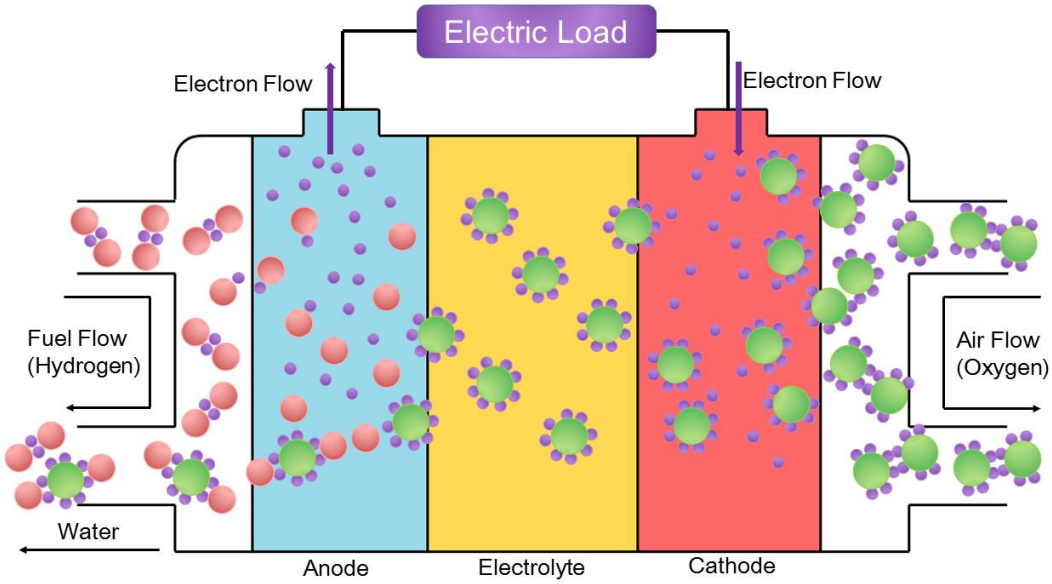

Figure 5.1. General Hydrogen Fuelled SOFC

Similar to other types of batteries, the main components of modern fuel cells are electrodes and electrolyte. Based on the chemical characteristics of electrolyte, the fuel cells can be classified as, alkaline (AFC), direct methanol (DMFC), phosphoric

acid (PAFC), sulfuric acid (SAFC), proton-exchange membrane (PEMFC), molten carbonate (MCFC), SOFC and protonic ceramic (PCFC) fuel cells [62]. The former five types of fuel cells are also known as low-temperature fuel cells, since their operating temperature varies from 50~210 ℃. The latter three types are known as high-temperature fuel cells since their operating temperature can reach 600 ℃ or even higher. High operating temperature provides the opportunities for the utilisation of methane which can be derived from fossil fuels directly and the inherent generation efficiency can reach up to 60% [97]. In this chapter, in consideration of the application in marine industry, the SOFC, as an example of high-temperature fuel cell is commonly used in marine propulsion systems, is selected for the fracture analysis during normal battery operation.

The operating principle of SOFC is shown in Fig. 5.1. The redox reaction in SOFC generates large amount of heat which raise the operating temperature up to around 800 ℃. High temperature not only provides a suitable environment for ion transportation through ceramic electrolyte materials, but also catalysis side reactions in SOFC. Moreover, the electrode and electrolyte layer will deform under large thermal loading. Since the electrolyte material is added inside the electrode layer, the mechanical properties in each layer are not homogenous. Besides, due to different material properties of electrodes and electrolyte, differences in mechanical deformation are observed at different parts of SOFC [12]. Hence, degradation of SOFC may occur which may cause negative influence on fuel cell performance and even failure.

Fracture and fatigue analysis of SOFC is important in battery design. The numerical studies of fracture in SOFC is very limited in the literature. Laurencin et al. [60] utilized a combined finite element and statistical approach of Weibull to predict cell fracture. Although FEM is well-established technique for determination of stresses, its capability is relatively limited in failure prediction as discussed in chapter 3. In this chapter, fracture analysis of SOFC is under investigation by using bond-based PD.

5.3 Thermomechanical analysis of porous electrode plate

5.3.1 Numerical model and loading condition for SOFC plate specimen

Generally, the SOFC unit is a multilayer structure which is composed of ceramic and metallic materials [98]. Electrode layers and electrolyte layers are stacked in a certain sequence. Besides, part of electrolyte materials are inserted into the electrode layers to increase the efficiency of the electrochemical reaction. In order to obtain detailed visualization of particle distribution in electrode layers, various advanced technologies such as scanning electron microscopy and X-ray computed tomography have been applied [12], [99]. An anode layer (Ni-YSZ) is considered and a colour image is shown in Fig. 5.2.

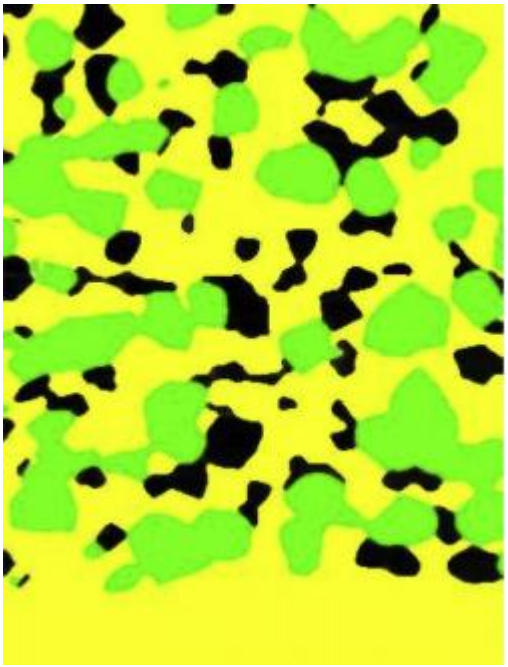

Figure 5.2. Nickel-YSZ anode layer [12]

In Fig. 5.2, the yellow colour represents the electrolyte (YSZ) material and the green colour represents the electrode (Ni) material. Black colour in this figure represents pore. Based on this information, the anode layer can be uniformly discretised into finite number of points with a certain volume as shown Fig. 5.3. The dimensions of

the anode layer are given as $12\mu\text{m}\times15.9\mu m\times0.12\mu m$. Since the thickness is relatively small as compared to the length and width scales, the plane stress assumption is utilised. The whole anode plate is uniformly discretised by 11473 material points. 3853 of them is electrode points and 7620 of them is electrolyte points. The operating temperature of SOFC varies from 800℃ to 1000℃ and multiple cases with different thermal loading conditions are considered in order to evaluate the stress evolution and fracture occurrence.

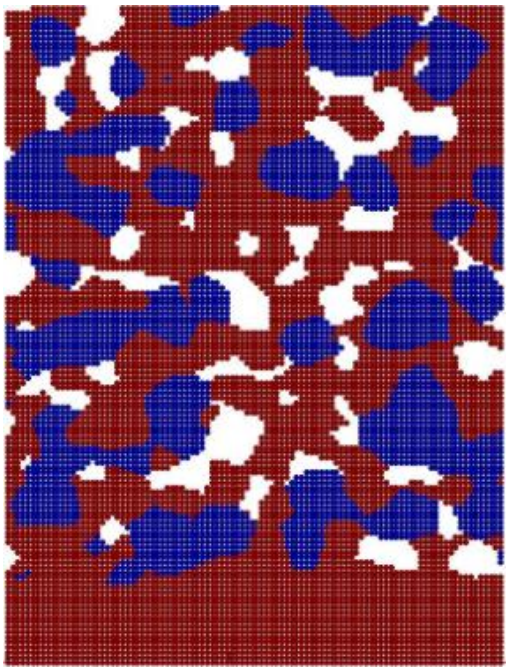

Figure 5.3. Discretisation of Nickel-YSZ anode layer: electrolyte particles are marked in red and electrode particles are marked in blue

5.3.2 Numerical Results

In this chapter, we first performed thermomechanical analysis of SOFC layer without considering failure to obtain displacement and von Mises stress distributions to compare the PD results against FEM results. Then, the crack evolution is under investigation. Three different bond strength configurations for the electrode-electrolyte interface (weak interface, uniform interface and strong interface) were

considered. Dimensions of the electrode plate specimen are specified as $12\mu m \times 15.9\mu m$. Top edge of the plate is free whereas the left and right edges of the plate are constrained in horizontal direction. Bottom edge is fully constrained. Due to small plate dimensions and high operating temperature, it is assumed that the temperature is uniform throughout the plate. Moreover, the influence on temperature by mechanical deformation is weak that can be ignored. Recalling the coupled field equation of motion in Chapter 3 (Eq. (3.2)) and Fourier's Law, the governing equation of this simulation can be expressed as:

$$\rho \frac{\partial^2 \vec{u}\left(\vec{x},t\right)}{\partial t^2} = \int_H \mathrm{f}\left(\vec{u}\left(\vec{x}',t\right) - u\left(\vec{x},t\right), \vec{x}' - \vec{x}\right) dV_{\vec{x}'} + \vec{b}\left(\vec{x},t\right) \tag{5.1a}$$

$$\rho c_v \dot{T} = k\nabla^2 T = k\left(\frac{\partial^2 T}{\partial x^2} + \frac{\partial^2 T}{\partial y^2}\right) \tag{5.1b}$$

With the PDO, the numerical expression of Eqs. (5.1) can be expressed as:

$$\rho \ddot{\vec{u}}\left(\vec{x},t\right) = \sum_{j=1}^{n} c\left(s - \alpha T_{avg}\right) V_j + \vec{b}\left(\vec{x},t\right) \tag{5.2a}$$

$$\rho c_v \dot{T} = k\left(\sum_{j=1}^{n}\left(T_j - T_i\right) g_2^{20}\left(\vec{\xi}\right) V_j + \sum_{j=1}^{n}\left(T_j - T_i\right) g_2^{02}\left(\vec{\xi}\right) V_j\right) \tag{5.2b}$$

where ***c*** is the two dimensional bond constant as shown in Table 3.1 in Chapter 3. *s* refers to the bond stretch. α represents the coefficient of thermal expansion. T_{avg} shows the average temperature. $\vec{b}$ is the body force and *k* represents the thermal conductivity. Material properties of electrode and electrolyte are given in Table 5.1.

Table 5.1. Material properties of anode layer

Material	Unit	Nickel	8YSZ
Temperature	℃	800	800
Elastic modulus	GPa	207	157
Poisson's Ratio	N/A	0.31	0.313
Specific heat capacity	J/kgK	450	460
Density	kg/m^3	8500	5200
Thermal conductivity	W/m ℃	60.7	2.1
Thermal expansion coefficient	$\alpha \times 10^{-6}$	13.5	10.5
Yield strength	MPa	59	N/A
Tensile strength	MPa	317	N/A
Material Toughness	$MPa\sqrt{m}$	125	3.5

5.3.2.1 Thermomechanical deformation without failure

Normal operating temperature of SOFC varies from 800 ℃ to 1000 ℃. High temperature may cause degradation of the electrode plate. In this case, thermomechanical analysis was performed by disregarding failure. Under uniform temperature loading at 800 ℃, operating condition of the electrode and origin of the damage can be investigated. Displacement and von Mises stress distributions based on PD are shown in Fig. 5.4 and Fig. 5.5. Besides, results are also obtained by using FEM for comparison.

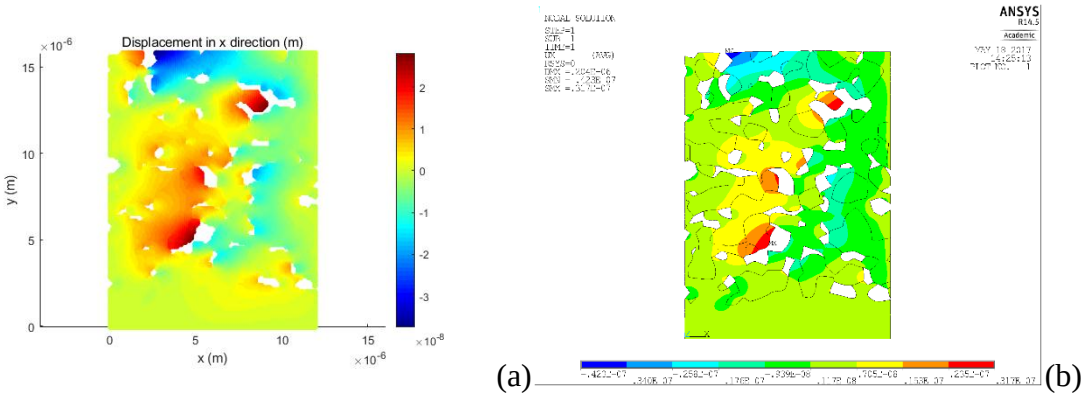

(a) (b)

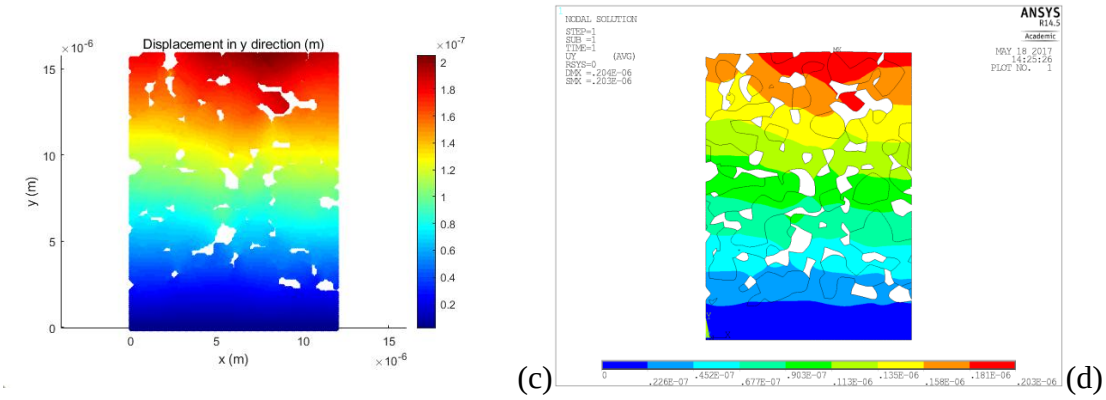

(c) (d)

Figure 5.4. Comparison between PD and FEM: (a) Displacement in horizontal direction by PD (b) Displacement in horizontal direction by FEM (c) Displacement in vertical direction by PD (d) Displacement in vertical direction by FEM.

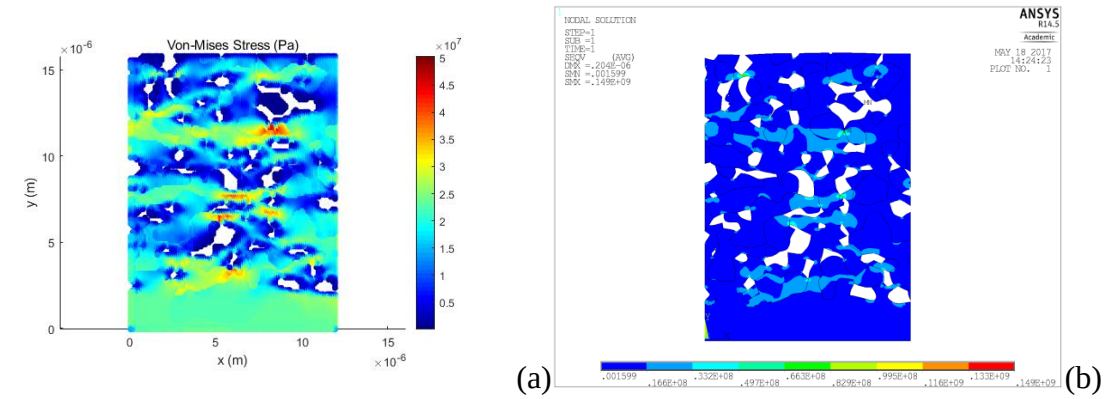

(a) (b)

Figure 5.5. Comparison between PD and FEM: (a) von-Mises Stress by PD (b) von-Mises Stress by FEM

Table 5.2. Comparison of maximum deformation and von-Mises stress

	Ux(*nm*)	Uy(*nm*)	vM stress(*MPa*)
FEM	31.7	203	49.7
PD	28	207	50

According to Table 5.2, Fig. 5.4 and Fig. 5.5, the results from PD and FEM have reached an agreement for von-Mises stress and displacements in both horizontal and vertical directions. Due to the heterogeneous discretisation scheme applied in FEM, more detailed stress (149*MPa*) value can be captured in high geometrical singularity regions. However, uniform discretisation scheme is applied in bond-based PD which

can only capture the stress roughly. The stress value around these regions boundary are similar to each other which shows a good reliability of bond-based PD in stress calculation. Since some of the boundaries of the plate specimen are constrained, the pores tend to shrink. Hence, high stresses will concentrate around pore regions especially those with sharp tips. Fig. 5.5 shows the distribution of von-Mises stress and they indicate the possible positions that cracks may form. The results have overall agreement between PD and FEM and they validate the capability and reliability of the peridynamic theory.

5.3.2.2 Thermomechanical simulation with crack propagation

According to Fig. 5.5, the maximum von-Mises stress inside the anode plate is around 150MPa under 800 ℃ thermal loading. As a result, the stretch of bonds around this region can exceed a critical value. Since, the interaction strength between electrode and electrolyte particles is unknown, three cases were considered to demonstrate damage formation and evolution based on the strength of electrode-electrolyte interface, i.e. weak interface, uniform interface and strong interface. Critical stretch values for the bonds crossing electrode-electrolyte interface are assumed to be $0.5s_c$ as weak interface, s_c as uniform interface and $2s_c$ as strong interface. Thermal loading gradually increases from 0 ℃ to 1000 ℃ in 10000 steps.

Damage states for the three different interface strength cases in one single charging process are shown in Fig. 5.6 ~ Fig. 5.8. The formation and evolution of cracks differ in all three cases. Damage initiates at high hydrostatic stress regions of the plate， such as pore regions with sharp geometry. As the temperature increases, the amount of damage increases. Maximum damage at 1000 ℃ reaches 16%, 3.1% and 2.5% for weak, uniform and strong interface configurations, respectively. For the weak interface case, due to low critical stretch value, damage prefers to evolve and propagate along the electrode-electrolyte interface. This will lead to the separation between electrode particles and electrolyte particles. However, for uniform and strong interface cases, the separation of electrode and electrolyte is not obvious.

Most of the damages form at electrolyte regions and pore boundaries where high hydrostatic stresses are located. Since the fracture toughness of the YSZ is much weaker as compared to Ni, electrolyte particles damage much easier than electrode particles. Moreover, the damage starts at lower temperatures for the weak interface case.

According to the simulations described above, damage evolution depends on electrode and electrolyte interface configuration and SOFC electrode plate geometry. By applying PD, the damage situation, probable position of fracture and probable direction of fracture evolution of the plate can be predicted in a single charging process. During frequent cycling operations, cracks may form and propagate due to the increase of damage. Electron flow from high electric potential region to low electric potential region through electrolyte particles. However, once the electrolyte particles are damaged, electron diffusion path may be blocked by these cracks and damages. Therefore, electron may have to find alternative paths to diffuse into a low electric potential region. This may cause an increase of inner resistance and reduction of electrical capacity and thermal stability, which will lead to performance degradation and even failure of the fuel cell.

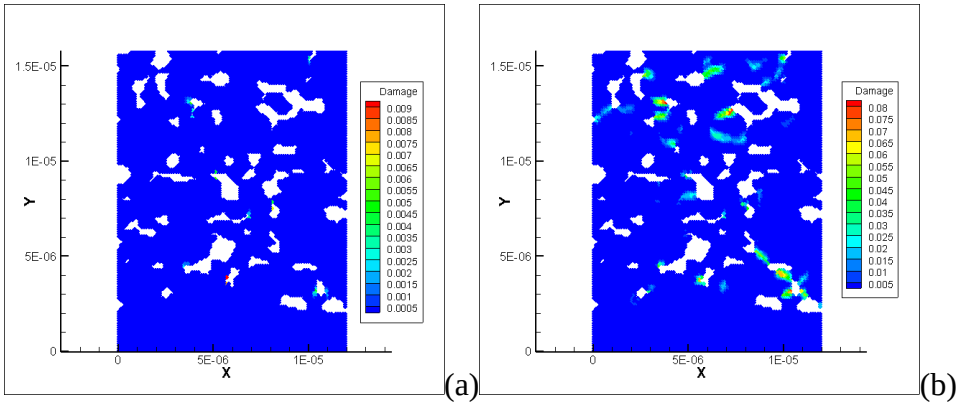

(a) (b)

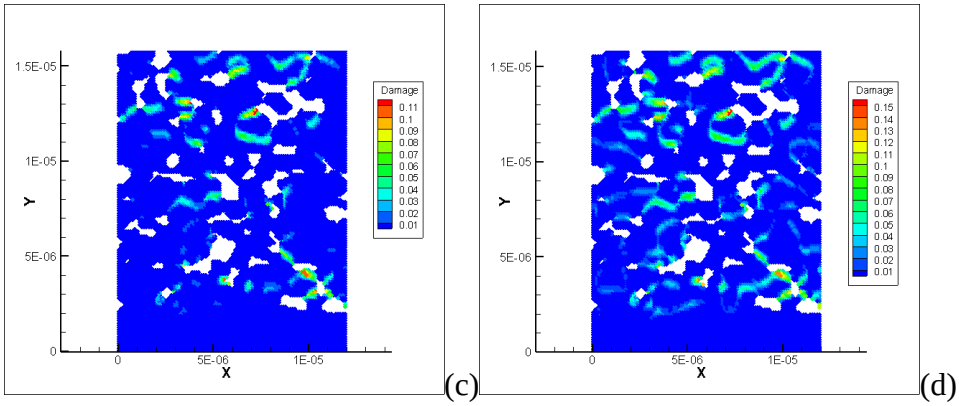

(c) (d)

Figure 5.6. Damage state for the weak interface configuration: (a) 600 ℃ (b) 800 ℃ (c) 900 ℃ (d) 1000 ℃

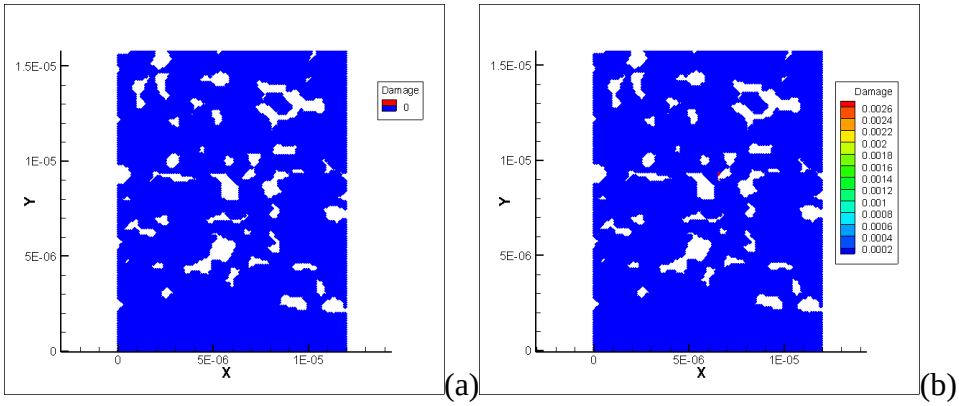

(a) (b)

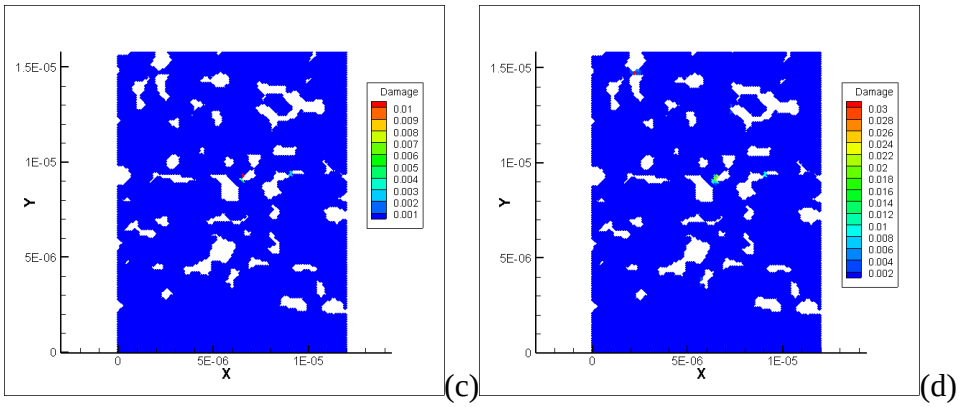

(c) (d)

Figure 5.7. Damage state for the uniform interface configuration: (a) 600 ℃ (b) 800 ℃ (c) 900 ℃ (d) 1000 ℃

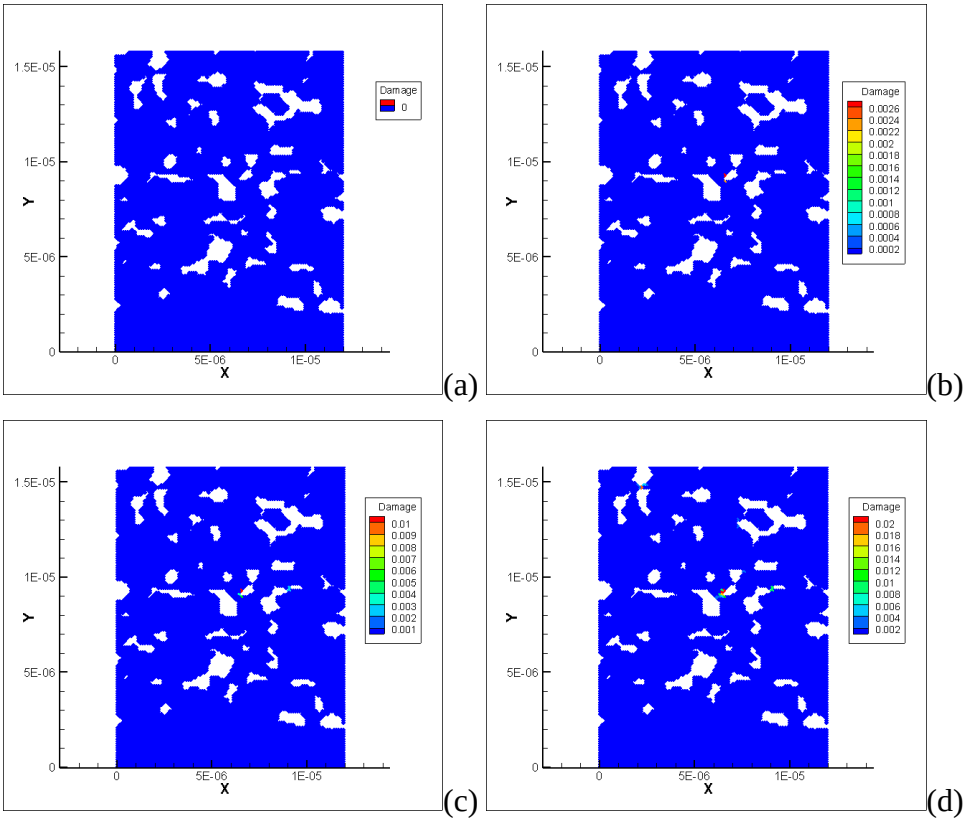

Figure 5.8. Damage state for the strong interface configuration: (a) 600 ℃ (b) 800 ℃ (c) 900 ℃ (d) 1000 ℃

5.4 Summary

SOFC, as one of the most popular power storage equipment, has relatively high power output, excellent emission control and wide fuel suitability. In order to increase efficiency of electrolchemical reaction in fuel cells, electrolyte materials are mixed with electrode material. Since the operating termperature varies from 800 ℃ to 1000 ℃, fuel cell may be damaged due to different material properties of electrode and electrolyte. Under high temperature loading, electrode plate deforms and stresses concentrate at some of the pore boundaries, especially those with sharp tips. Hence, damage may occur at these regions. Damage may also evolve along electrode-electrolyte interfaces especially if the interface strength is weaker. This may degrade the cell performance and even cause the failure of the fuel cell.

Therefore, fracture analysis of SOFC is essential and peridynamics as a new computational technique is used for the first time in the literature for this purpose. First, the capability of peridynamics is validated by considering a simple square plate specimen under uniform loading condition. Peridynamic results show a good aggreement with FEM. Then, damage evolution in a porous electrode plate under uniform temperature loading is investigated. Three different cases with different strengths of electorde and electrolyte interfaces are discussed in this study. For the weaker interface case, damage starts at lower temperature than the stronger interface cases. Moreover, since the fracture toughtness of electrolyte material (YSZ) is weaker than electrode material (Ni), electrolyte is damaged earlier while electrode remains undamaged.

Due to the high complexity of three dimensional SOFC model and the limitation of computer performance in the university, the three dimensional study will be finished in my future research. The three dimensional fracture of SOFC will be extended to a whole SOFC unit, which contains anode, electrolyte and cathode, to obtain a more realistic model. Besides, the influence of temperature on material properties should also be taken into consideration. Due to only a single charging process is under consideration, damage results may not be obvious in uniform and strong interface cases. Hence, research with multiple cycling process is necessary as a future study.

6 DIFFUSION INDUCED FRACTURE

6.1 Introduction

In this chapter, the fracture analysis of two dimensional lithium ion battery is under investigation. Since Si experiences large volumetric change during battery cycling, fracture analysis or pulverization may occur inside the electrodes. In order to investigate the evolution of damage inside lithium ion battery electrode, the battery plate with various damage cases are selected. Based on these models, the relationship among fracture evolution, deformation, lithium ion concentration and hydrostatic stress is investigated. The background knowledge and previous works are presented in section 6.2. The lithiation induced deformation during charging process is described by coupled field equations which are presented in section 6.3. Numerical models of the electrode plate and the detailed material properties are shown in section 6.4. The fracture analysis of simple single crack cases is presented in section 6.5 while more complex cases are presented in section 6.6. Section 6.7 gives a brief summary of the numerical results in this chapter.

6.2 Background

Lithium-ion (Li-ion) battery is one of the most promising energy storage systems due to its high energy density, high operating voltage, low self-discharge and low maintenance requirements [100]. Performance of Li-ion batteries mainly depends on material properties of anode, cathode and electrolyte. Several metals and compounds are selected as anode material such as Co, Ni, Mn and iron phosphate due to their performance in terms of thermal stability, capacity, conductivity and safety [8]. One of the anode materials, Si, is under investigation for more than 30 years due to its high theoretical charging capacity (3600~4200mAHg^{-1}) [66], [67] [101]. However, as lithium ions diffuse into Si particles, the Si particles experience large volume

expansion up to around 400% [66], [68]. Frequent cycling of the lithium ion battery leads to stress misdistribution, degradation and delamination of the battery components which can significantly affect the battery performance.

The lithiation process depends on the molecular structure of Si [102]. For crystalline Si, the Si molecules will turn into amorphous lithiated silicon (Li_xSi) at the initial stage of lithiation. As the lithiation proceeds, the amorphous Li_xSi will transform further into crystalline lithiated silicon ($Li_{15}Si_4$) due to the increase of lithium concentration. There will be a thin reaction layer lies between crystalline $Li_{15}Si_4$ and Si with a sharp gradient of lithium concentration. The moving speed of the reaction layer slows as the lithiation proceeds. For amorphous Si, pure Si will turn into amorphous lithiated silicon Li_xSi. The Li_xSi has two stages: $x = 2.5$ for early lithiation and $x = 3.5$ for fully lithiation. However, the reaction layer moves at a constant speed as the lithiation proceeds.

Many research on lithium-ion battery can be found in section 2.4. In this study, as an alternative approach, PD is utilized to investigate the fracture evolution in electrode plates of lithium ion batteries by considering pressure gradient and material phase change factors. PDO is also applied in building up the numerical expression of coupled field equations to describe the relationships among lithium ion concentration, hydrostatic stress and mechanical deformation.

The governing equation of diffusion induced deformation and the model are provided in sections 6.2 and 6.3, respectively. The results in single crack case and multiple crack cases are described in section 6.4 and section 6.5, respectively. Besides, the results with and without considering material phase change is also discussed in these sections. Finally, a short summary will be presented in section 6.6.

6.3 Coupled diffusion-mechanical deformation mechanism

The general lithium diffusion phenomenon can be represented by using Fick's Second Law [103]. Since Si is selected as anode material for lithium-ion battery in this study, there is a large amount of volume change during lithiation and delithiation as discussed above. Therefore, the stress induced by volume change during battery cycling should not be ignored. The stress components, σ_{ij}, can be expressed as [71]:

$$\sigma_{xx} = \frac{E}{1-\nu^2}\left(\frac{\partial u}{\partial x} + \nu\frac{\partial v}{\partial y}\right) - \frac{E\Omega C_{\max}}{3(1-\nu)}C \tag{6.1a}$$

$$\sigma_{yy} = \frac{E}{1-\nu^2}\left(\frac{\partial v}{\partial y} + \nu\frac{\partial u}{\partial x}\right) - \frac{E\Omega C_{\max}}{3(1-\nu)}C \tag{6.1b}$$

$$\sigma_{xy} = \sigma_{yx} = \frac{E}{2(1+\nu)}\left(\frac{\partial u}{\partial y} + \frac{\partial v}{\partial x}\right) \tag{6.1c}$$

where Ω is the partial molar volume of Si. u and v is the displacements in x and y directions, respectively. C_{max} is the maximum lithium concentration in the plate and C is the current normalized concentration. As lithiation proceeds in the electrode, local stresses will increase at high geometrical singularity regions such as crack tips. Due to the pressure-gradient, large amount of lithium ions move into these regions which will lead to relatively large volume expansion and increase of lithium ion concentration. By considering these factors, the general Fick's Second Law should be modified as [71]:

$$\frac{\partial C}{\partial t} = Mk_BT\left(\frac{\partial^2 C}{\partial x^2} + \frac{\partial^2 C}{\partial y^2}\right) - \frac{MC\Omega}{N_A}\left(\frac{\partial^2 \tilde{\sigma}}{\partial x^2} + \frac{\partial^2 \tilde{\sigma}}{\partial y^2}\right) - \frac{MC\Omega}{N_A}\left(\frac{\partial C}{\partial x}\frac{\partial \tilde{\sigma}}{\partial x} + \frac{\partial C}{\partial y}\frac{\partial \tilde{\sigma}}{\partial y}\right) \tag{6.2}$$

where M is molecular mobility, k_B is Boltzmann constant, T is absolute temperature, N_A is Avogadro's constant and $\tilde{\sigma}$ is the hydrostatic stress.

Once the lithium ions diffuse into the anode plate, the anode material transforms from pure Si to Li_xSi. Normally, the material properties of the anode plate, such as elastic modulus and fracture toughness, will decrease depending on the state of lithiation. Hence, the Si lithiation process is also known as material softening process [104]. As described in last section, Si experiences partial and fully lithiation process. However, in this study, since the thickness of the reaction layer is very thin compared to the anode geometry [102], this interface layer is not taken into consideration.

6.4 Numerical studies

In this study, a square Si plate is selected to represent the anode plate of the lithium ion battery. Both pure Si and lithiated Si are regarded as brittle materials. Concentration values are normalized by maximum concentration. The square specimen with pre-existing crack is free from lithium-ions and mechanical constraints at its initial state (as shown in Fig. 6.1). Then the Si specimen is subjected to maximum lithium ion concentration on all of its boundaries. The thickness of the specimen plate is negligible compared with the boundary length. Therefore, plane stress assumption is utilized in order to simplify the numerical simulations. The square plate is uniformly discretised by 100×100 particles. Geometrical and material information are summarized in Table 6.1.

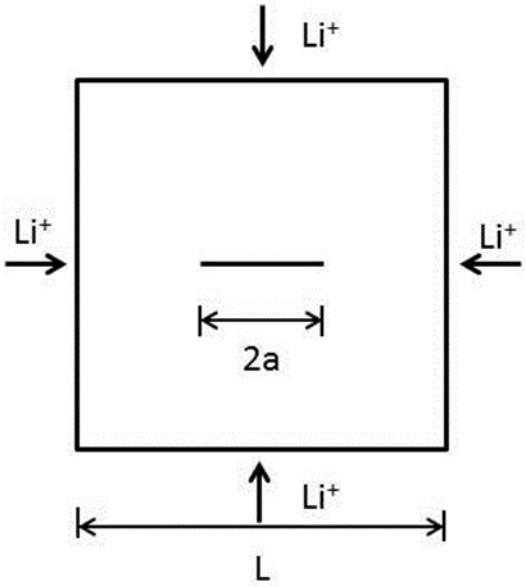

Figure 6.1. Pre-cracked square electrode plate specimen

Table 6.1. Geometrical and material parameters in numerical simulations

Description	Parameter	Value	unit
Length of the specimen	L	1	μm
Elastic constant of silicon	E_{Si}	80	GPa
Elastic constant of amorphous $Li_{15}Si_4$	$E_{Li_{15}Si_4}$	41	GPa
Poisson's ratio of silicon	v_{Si}	0.22	N/A
Poisson's ratio of silicon	$v_{Li_{15}Si_4}$	0.24	N/A
Partial molar volume	Ω	8.5×10^{-6}	m^3mol^{-1}
Molecular mobility	M	500	$m^2J^{-1}s^{-1}$
Boltzmann constant	k_B	1.38×10^{-23}	$J\cdot K^{-1}$
Absolute temperature	T	300	K
Avogadro's constant	N_A	6.02×10^{23}	mol^{-1}
Critical strain for silicon	s_{c_Si}	0.04	N/A
Critical strain for amorphous $Li_{15}Si_4$	$s_{c\_Li_{15}Si_4}$	0.035	N/A
Maximum concentration	C_{max}	1.18×10^{4}	$mol\cdot m^{-3}$

Although the Poisson's ratio of amorphous Si and lithiated Si are 0.22 and 0.24 respectively, it has to be strictly set as 1/3 in the following simulations due to the limitation of two-dimensional bond-based peridynamics [31]. In this study, entire

solution process of coupled peridynamic equation of motion is summarised by a flow chart as shown in Fig. 6.2.

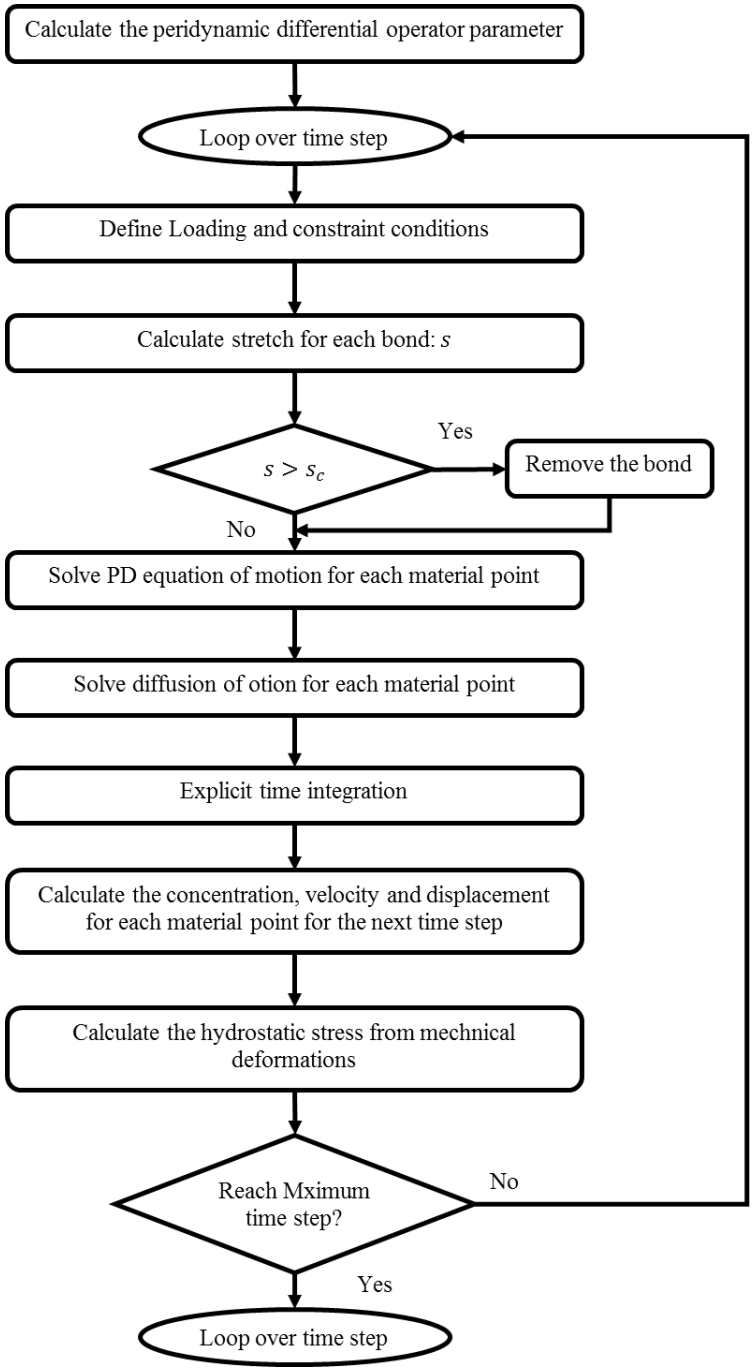

Figure 6.2. Flow chart of solution process

6.5 Coupled analysis for a single crack

In this case study, an initial crack, which has a length equivalent to 20% of the length of the specimen plate, lies horizontally in the central region. Initial damage is shown in Fig. 6.3a. The whole specimen plate is regarded as pure Si plate during charging process. As the lithiation progresses, the boundary region of the plate expands first (Fig. 6.3b and Fig. 6.3c). Due to the deformation, the boundary region is subjected to compression loading and then the centre region is subjected to tension loading. Since crack is located at the centre of the plate, the stress concentrates at the two crack tip regions and the maximum tension stress reached around 420MPa (Fig. 6.3.d). According to Eq. 6.3, the high pressure gradient at the crack tip regions is the main motivation of lithium ion enrichment, and therefore "two dots" can be observed in Fig. 6.3e which represents higher concentration around crack tip area.

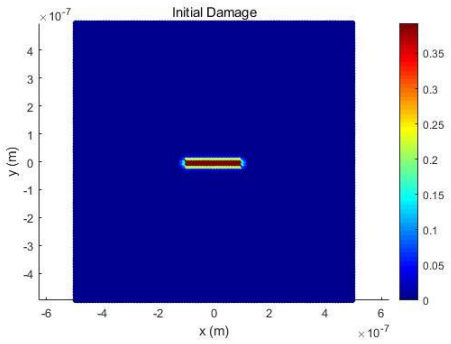

(a)

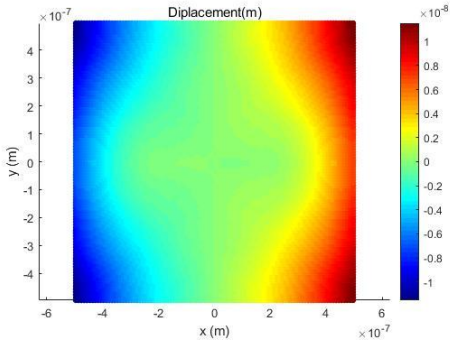

(b)

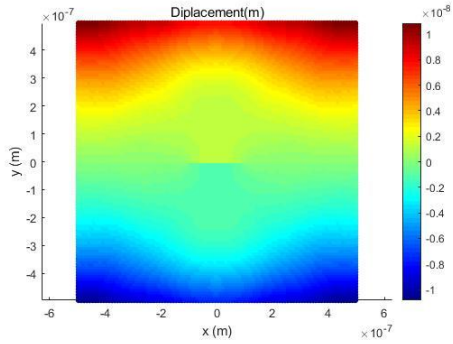

(c)

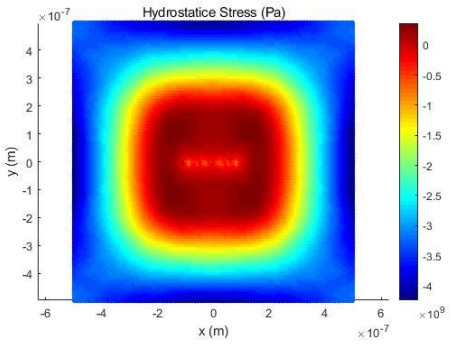

(d)

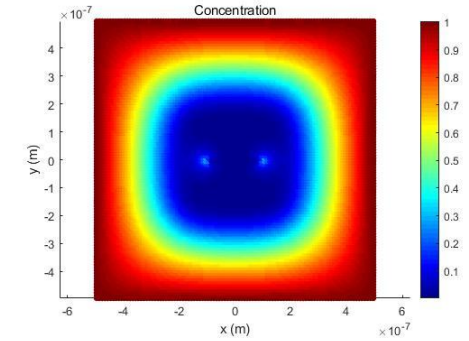

(e)

Figure 6.3. Results of electrode plate with stationary crack: (a) Initial damage (b) Displacement in *x* direction (c) Displacement in *y* direction (d) Hydrostatic stress (e) Lithium ion concentration

The electrode material in this simulation is not strong enough to withstand high hydrostatic stress (420*MPa*). Therefore the crack should propagate to release the accumulated energy. As a result, strain energy release rate will decrease and crack surface energy will increase. In PD, according to Eq. (3.7) and Eq. (3.8) in chapter 3, the crack growth is reflected on large amount of bond breakage. The critical stretch for electrode material is 0.04 (Table 6.1). Once the bond stretch exceeds this value, it should break and then crack will propagate. The high lithium concentration region at the crack tips is moving as the crack propagates (Fig. 6.4).

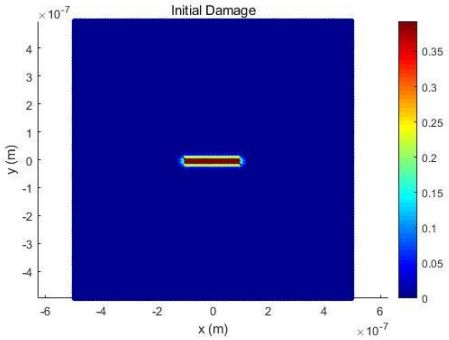

(a)

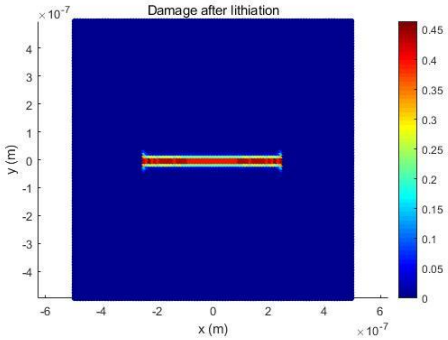

(b)

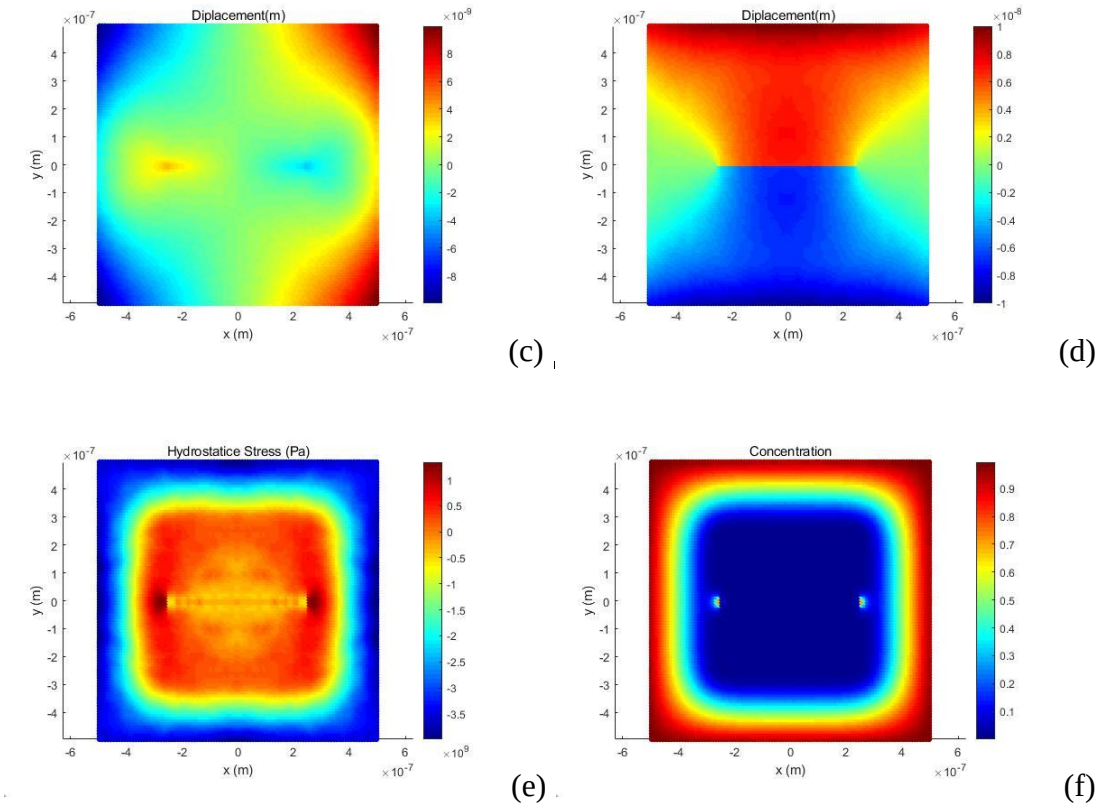

Figure 6.4. Results of electrode plate without considering material phase change: (a) Initial damage (b) Damage after deformation (c) Displacement in *x* direction (d) Displacement in *y* direction (e) Hydrostatic stress (f) Lithium ion concentration

By considering the material phase change, the elastic modulus of the material particle drops from 80 *GPa* to 41 *GPa* after lithiation. The critical strain of material particle drops from 0.04 to 0.035. Therefore, material particle is "softened" after lithiation. Hence, the damage and hydrostatic pressure results are provided in Fig. 6.5.

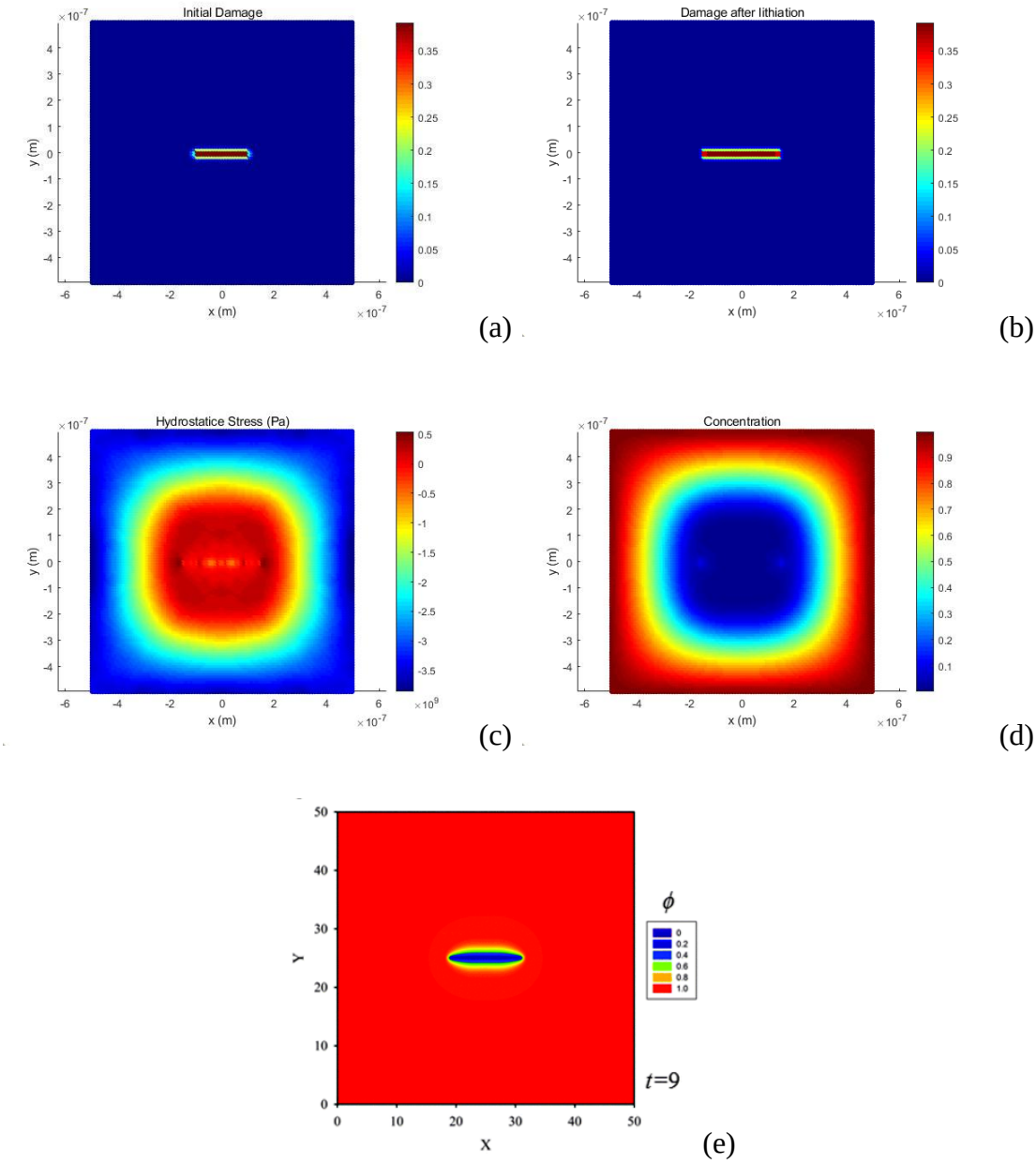

Figure 6.5. Result of electrode plate by considering material phase change: (a) Initial damage (b) Damage after deformation (c) Hydrostatic stress (d) Lithium ion concentration (e) Damage after deformation in the literature[71]

Results provided in Figs. 6.5 are the dynamic results of a single crack propagation by considering material phase change. During lithiation progresses, the amorphous silicon will transformed into fully lithiated silicon. However, by comparing the

results in the case without material phase change, the crack length after lithiation process is shorter than the case that does not consider the material phase change during the same lithiation period. Hence, the speed of crack propagation is dramatically reduced as shown in Fig. 6.5b. Since the crack tips are far from regions with high lithium ion concentration, the lithium ion concentration on crack tips is not as clear as Fig. 6.4f. By considering the material phase change, the hydrostatic stress around crack tip drops from 1.1GPa in Fig. 6.4e to 0.5GPa in Fig. 6.5d. Therefore, even though the critical bond stretch drops, the structure is stronger to withstand higher loading by considering the factor of material phase change. Fig. 6.5e shows the crack propagation in the literature[71]. However, Zuo and Zhao have applied a different damage scheme. Red colour refers to undamaged situation while bule colour refers to fully damaged situation. Results of crack propagation with considering material phase change are matched well with each other.

Single crack cases can not describe the influence of material phase change and lithium ion concentration on crack propagation in detail. More complex configurations are provided in following sections to illustrate this phenomenon.

6.6 Coupled analysis for multiple crack cases

Due to unexpected factors such as manufacturing quality and damage during transportation, electrodes may have multiple initial damages. Hence, single crack may not be sufficient for describing the conditions of damage in a battery electrode. In these case studies, electrode plates with multiple cracks with different orientation are investigated.

6.6.1 Twin cracks

A pair of cracks which are parallel to each other lie horizontally at the center of a plate as shown in Fig. 6.6. These cracks have the same length equivalent to 10% of the length of the specimen plate. Distance between these two cracks is 5% of the

plate width. As lithiation progresses, the hydrostatic stress and lithium ion concentration increase at the crack tips. Once peridynamic bonds reach the critical stretch value, they will break and crack will propagate. Similar to single crack case, the cases with and without material phase change are under investigation in this section.

For the analysis without considering the material phase change, the material of specimen plate is strictly set as Si. Hence, the damage evolution is not affected by the decrease of critical bond stretch by material phase change. In this case, the crack formation and propagation depends on the stretch of each material bond. In other words, it also depends on the hydrostatic stress. The results of parallel twin cracks can be seen in Figs. 6.6. Hydrostatic stress rises both at crack tips and region between twin cracks as shown in Fig. 6.6c. Since the distance between these cracks is relatively small, material particles in this region have less horizon members with respect to other particles inside the plate. Therefore, the cracks prefer to merge into one large crack first as shown in Fig. 6.6b and the propagation at crack tips is not obvious. Once the cracks merge into one large crack, the hydrostatic stress between the twin cracks releases. The hydrostatic stress at the outer crack tip regions is relatively larger, and the newly formed crack starts to propagate at these regions. According to Eq. (6.2), in low concentration region, hydrostatic stress is the major motivation in the increase of lithium ion concentration. Hence, the lithium ion concentration on crack tips is relatively higher than that on the surrounding region as shown in Fig. 6.6d.

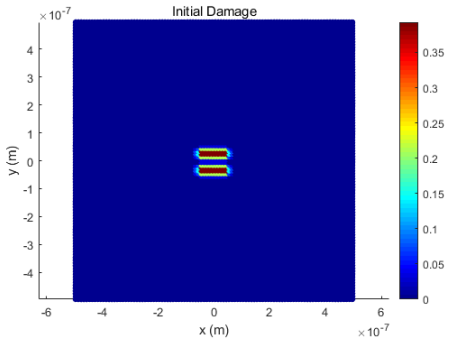

(a)

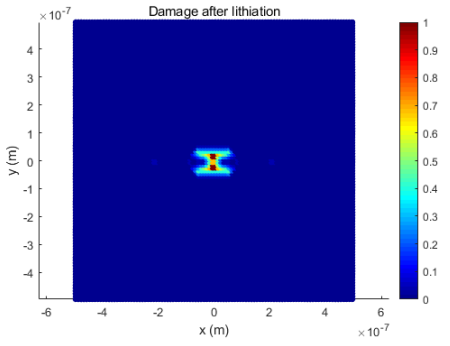

(b)

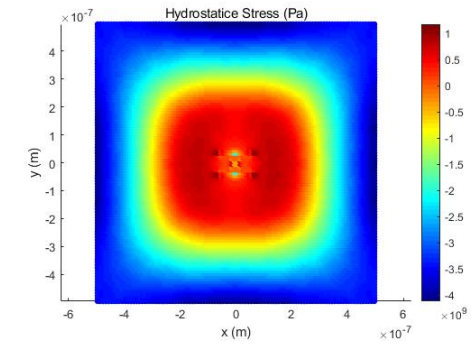

(c)

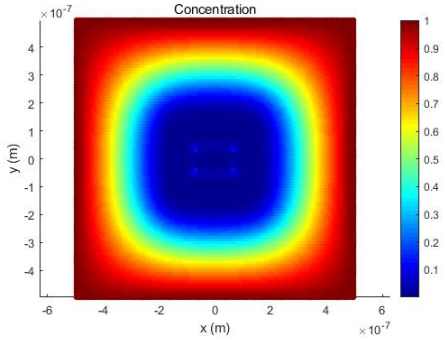

(d)

Figure 6.6. Result of plate with twin parallel cracks by considering material phase change: (a) Initial damage (b) Damage after deformation (c) Hydrostatic stress (d) Lithium ion concentration

For the analysis by considering material phase change, material of the specimen plate will be transformed from Si to lithiated Si after charging. Hence, hydrostatic pressure is not the only criterion in the prediction of crack propagation, but the reduction of critical stretch can also lead to fracture and damage inside the plate. As shown in Fig. 6.7b, upper crack propagates in upward direction and lower crack propagates in downward direction. Besides, according to Fig. 6.6b, high hydrostatic stress also exists for particles between the twin cracks, which means two cracks have a potential to merge into one large crack.

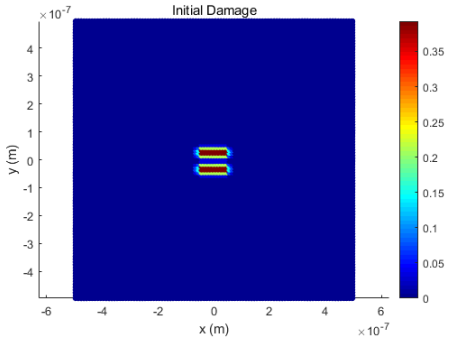

(a)

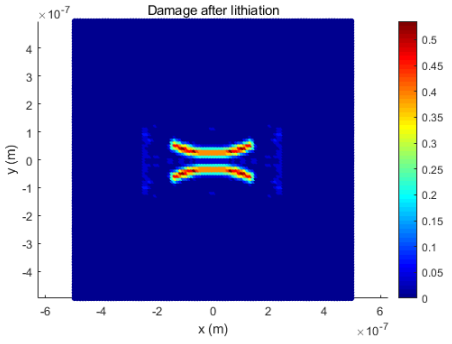

(b)

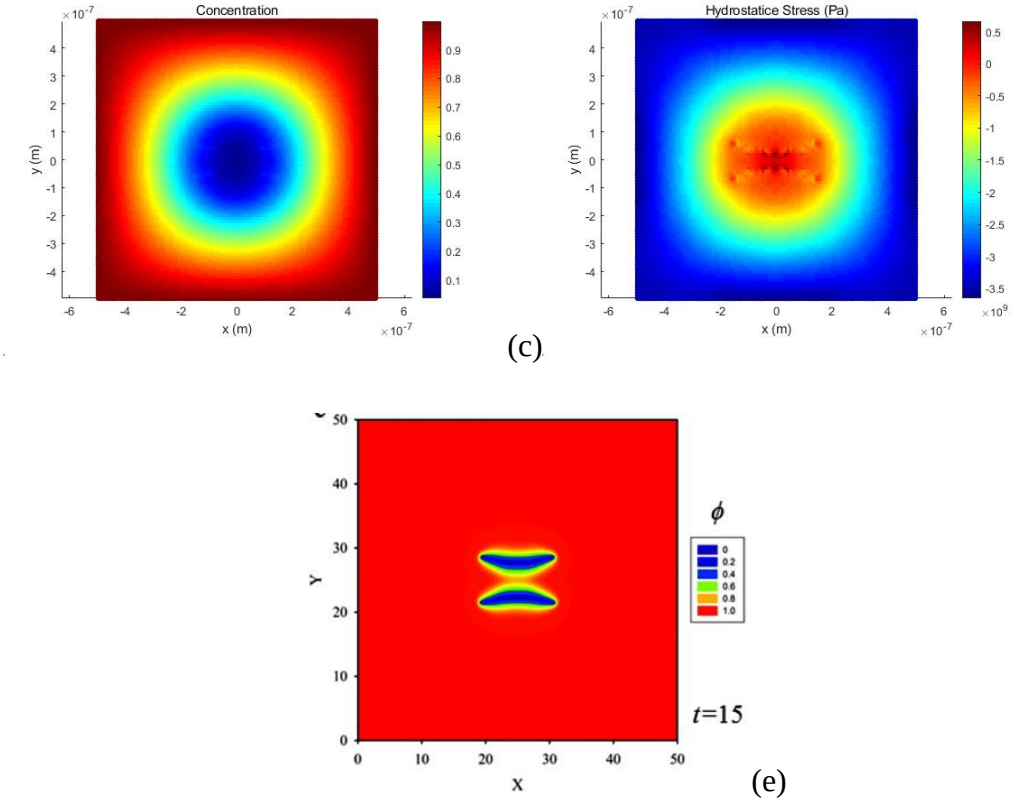

Figure 6.7. Result of plate with twin parallel cracks by considering material phase change: (a) Initial damage (b) Damage after deformation (c) Lithium ion concentration (d) Hydrostatic stress (e) Damage after deformation in the literature[71]

Twin cracks can also be arranged in other styles. In the following simulations, two cracks are arranged in right angle or oblique angle as shown in Fig 6.8a and Fig 6.9a. The size of the upper crack is 12% of the plate length and the size of the vertical crack is 10% of the plate length. The distance between these cracks is 10% of the plate length. Since the central region of the plate lies between these cracks, particles on central region can not build enough interactions with horizon members with respect to material particle in other regions. Hence, hydrostatic stress will concentrate at this region.

For cases without considering material phase change, crack propagation depends on high hydrostatic stress only. Since one of the crack tip of lower crack lies near central region, the hydrostatic stress will increase even higher. Therefore, cracks prefer to merge into a larger crack as shown in Fig. 6.8b and Fig. 6.9b. Then the hydrostatic stress in central plate releases. The newly formed crack propagates from outer crack tips toward high hydrostatic stress regions as shown in Fig. 6.8c and Fig. 6.9c. Lithium ion concentration at outer crack tip regions is relative larger than surrounding region as shown in Fig. 6.8d and Fig. 6.9d. Crack repulsion shown in Fig. 6.8b has a good agreement with the result in literature as shown in Fig. 6.8e.

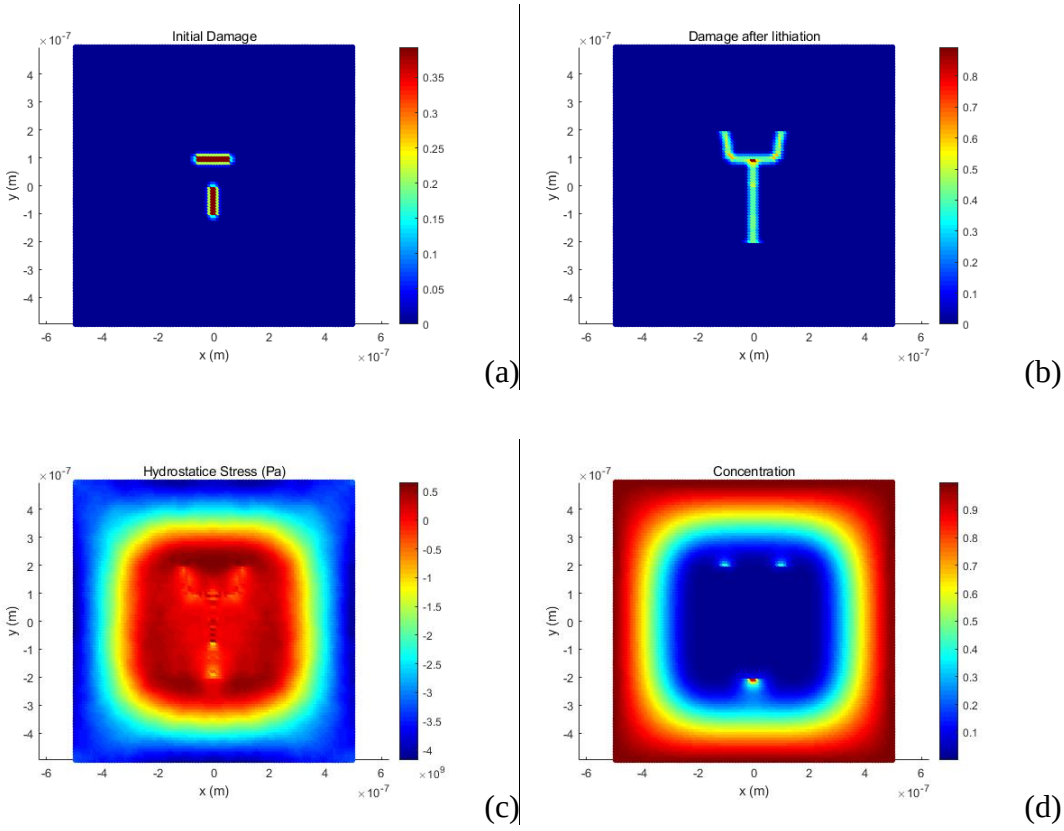

Figure 6.8. Results of plate with twin perpendicular cracks without considering material phase change: (a) Initial damage (b) Damage after deformation (c) Hydrostatic stress (d) Lithium ion concentration

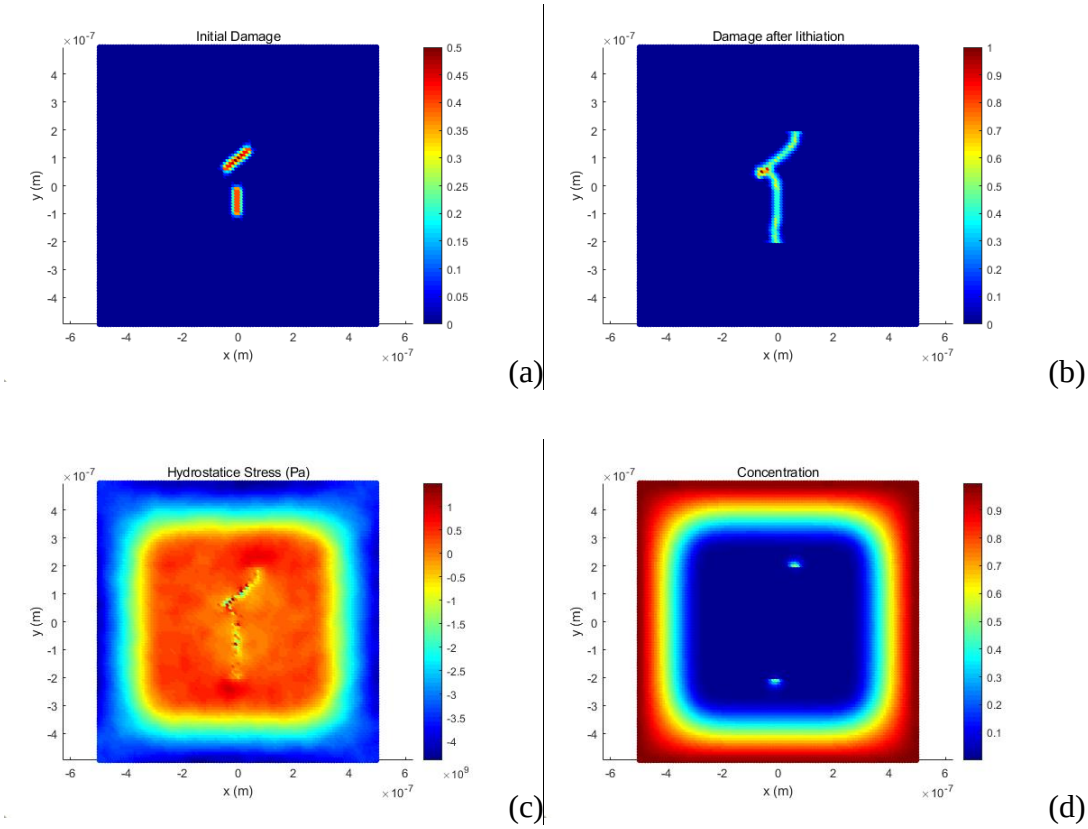

Figure 6.9. Results of plate with twin perpendicular cracks without considering material phase change: (a) Initial damage (b) Damage after deformation (c) Hydrostatic stress (d) Lithium ion concentration

For the analysis by considering material phase change, the structural stiffness will be affected by material phase change. Since the lithium ion concentration at the crack tip regions is higher than surround regions, the critical strain value in these regions will drop from 0.04 to 0.035 as material changing from Si to lithiated Si. Even though central plate has largest hydrostatic stress, the crack prefers to propagate at crack tip regions since material bonds reach critical strain. Hence, the damage after deformation can be shown as Fig. 6.10b and Fig. 6.11b. Crack propagates from outer crack tips toward high hydrostatic stress regions. At the same time, cracks will also propagate at central regions of the plate. The twin cracks tries to merge each other into one large crack. Regions with high hydrostatic stress have higher lithium ion concentration as compared with surrounding regions as shown in Fig. 6.10d and Fig.

6.11d. Similar with the result in the literature [71], the PD method can also capture the same trend in crack merge and propagation as shown in Fig. 6.10e and Fig. 6.11e.

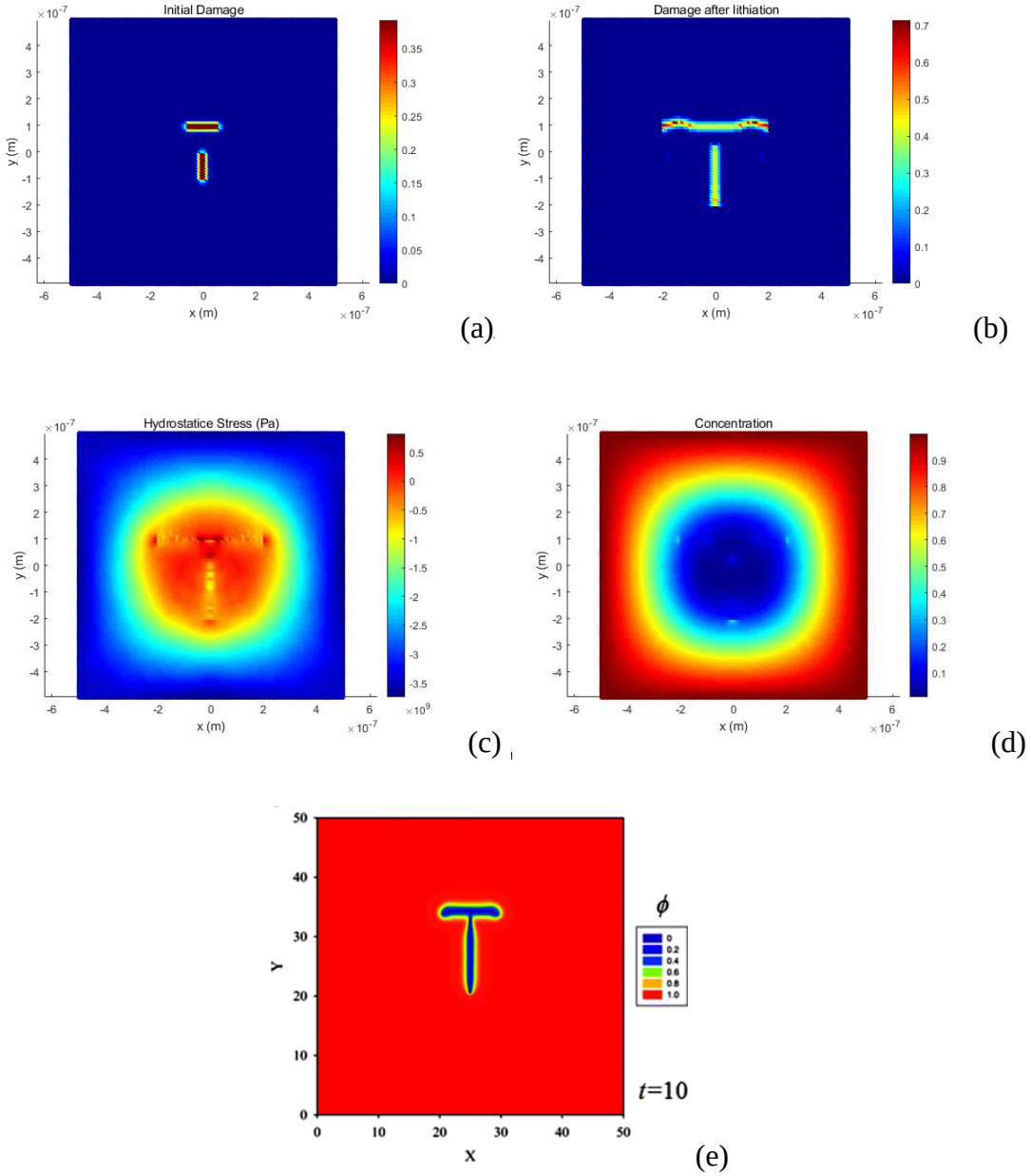

Figure 6.10. Results for plate with twin perpendicular cracks by considering material phase change: (a) Initial damage (b) Damage after deformation (c) Hydrostatic stress (d) Lithium ion concentration (e) Damage after deformation in the literature[71]

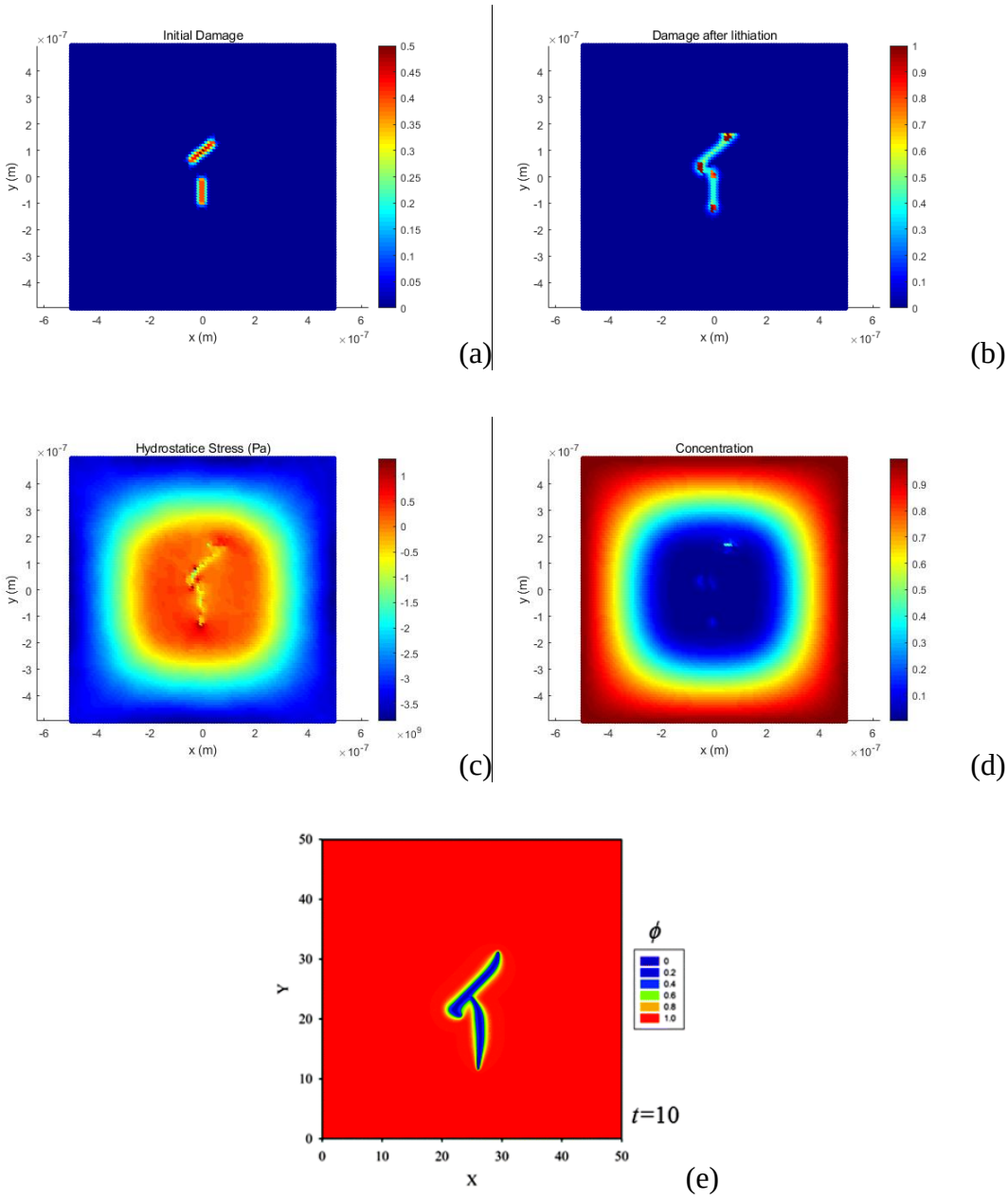

Figure 6.11. Results for plate with twin oblique cracks plate by considering material phase change: (a) Initial damage (b) Damage after deformation (c) Hydrostatic stress (d) Lithium ion concentration (e) Damage after deformation in the literature[71]

6.6.2 Multiple randomly arranged crack cases

Cracks in a battery electrode may have arbitrary arrangements in terms of crack number and crack orientations. In this study, triple horizontal crack case, six disorder crack case and eleven disorder crack case are under investigation.

6.6.2.1 Triple horizontal crack analysis

Cracks with the same length equivalent to 10% of the plate length located at the central plate region are shown in Fig. 6.12a. All of the cracks are horizontally oriented with spaces of 5% plate length in both horizontal and vertical directions. Since cracks are located close to each other, particles between cracks have fewer interactions with neighbouring particles within their horizons. Therefore, the stiffness of these particles are relatively weaker. Central crack propagates towards to neighbouring cracks from both crack tips and merges all three cracks into one crack as shown in Fig. 6.12b. It has make a good agreement with the result provided in the literature [71]. Then the propagation of outer crack tips continue horizontally along its initial crack path. High hydrostatic stresses exist at outer crack tips and the pressure at inner crack tips reduce since cracks already merge with each other as shown in Fig. 6.12c. Damage evolution of the plate with and without considering material phase change are similar with each other for this case as shown in Figs. 6.13.

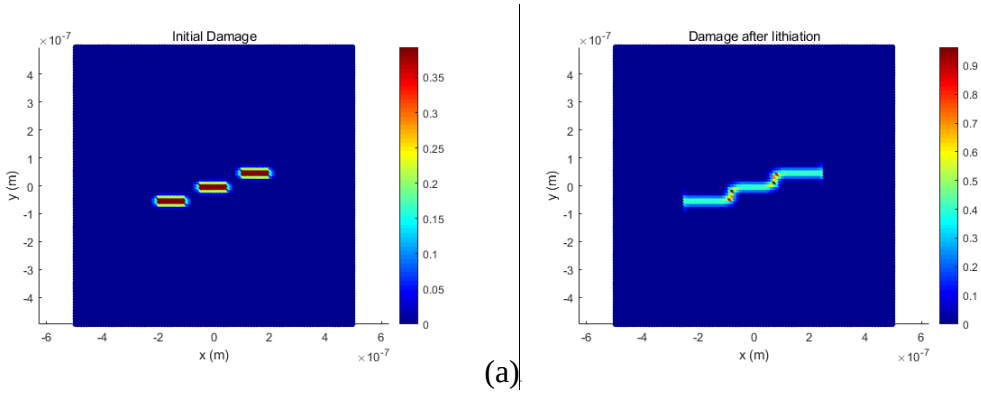

(a) (b)

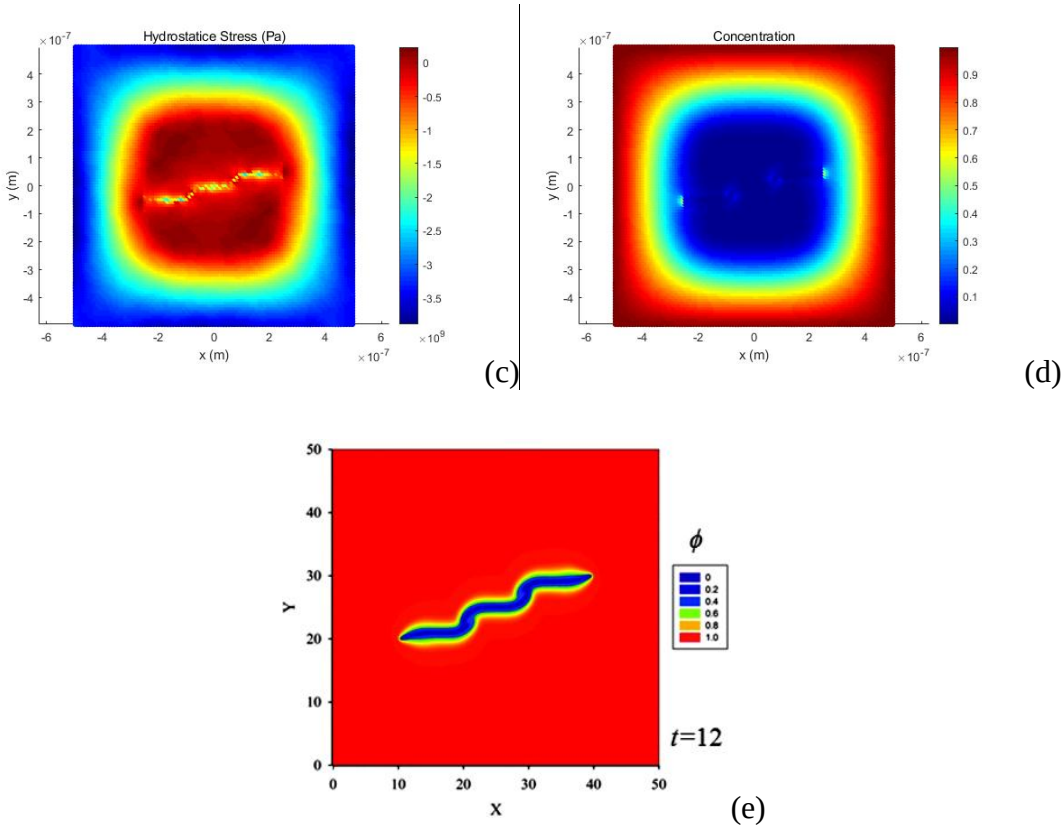

Figure 6.12. Results of plate with triple cracks electrode by considering material phase change: (a) Initial damage (b) Damage after deformation (c) Hydrostatic stress (d) Lithium ion concentration (e) Damage after deformation in the literature[71]

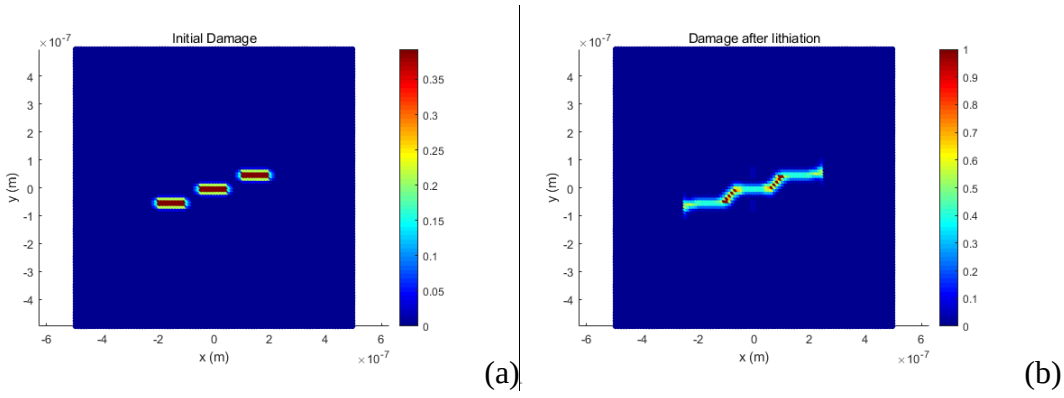

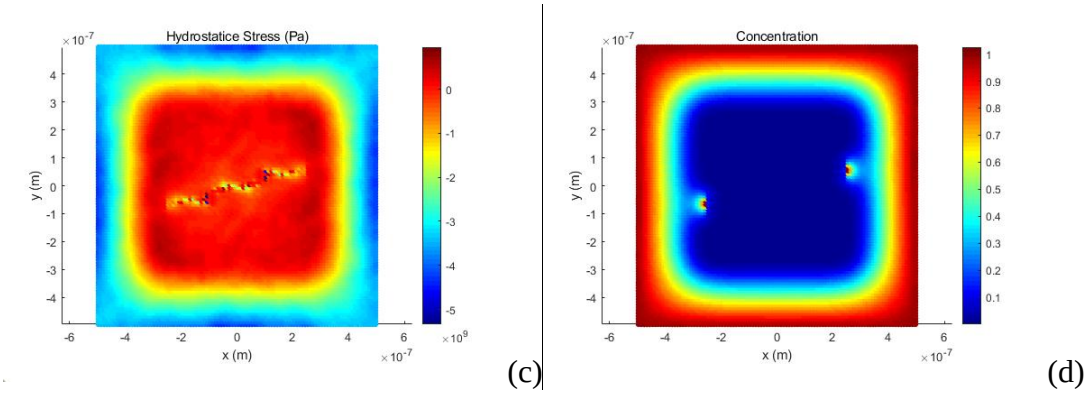

(c) (d)

Figure 6.13. Results of plate with triple cracks electrode plate without considering material phase change: (a) Initial damage (b) Damage after deformation (c) Hydrostatic stress (d) Lithium ion concentration

6.6.2.2 Disordered crack analysis

After certain amount cycling process, lithium ion battery electrodes may accumulate large amount of cracks. The shape and propagation direction of these cracks depend on the design of the battery electrode plate [105]. In order to simulate the damage in electrode plate after several cycling process, coupled field diffusion on battery electrode with multiple random cracks are under investigation in this section. Since the thickness of specimen plate is much smaller than its length, plane stress assumption is applied as in previous cases to increase calculation efficiency.

Two different battery plate specimens with multiple cracks (six cracks and eleven cracks) were considered to represent two different damage situations after several battery cycling processes. Each crack with 10% of specimen length is randomly positioned inside the plate. As lithium ion diffuses into crack tip regions, hydrostatic stress increases dramatically at the crack tips. Hence, some cracks merged into a large crack from inner crack tips where high hydrostatic stress exist. After cracks merge into larger cracks, local stress releases. Hence, some cracks which is surrounded by these larger cracks will not propagate. The newly formed larger cracks are “preventing” the small cracks to propagate. On the other hand, outer crack

tips will not be affected by other cracks and propagate toward high hydrostatic stress region.

By considering material phase change, crack propagation may not be always different from that without considering material phase change. For crack tips close to material phase boundary, the lithium ion concentration close to crack tip region is relatively higher than surrounding regions according to Eq. (6.2). Then, Si will transform into lithiated Si and the critical stretch drops. Cracks will also propagate from outer crack tips where material bonds reach critical value.

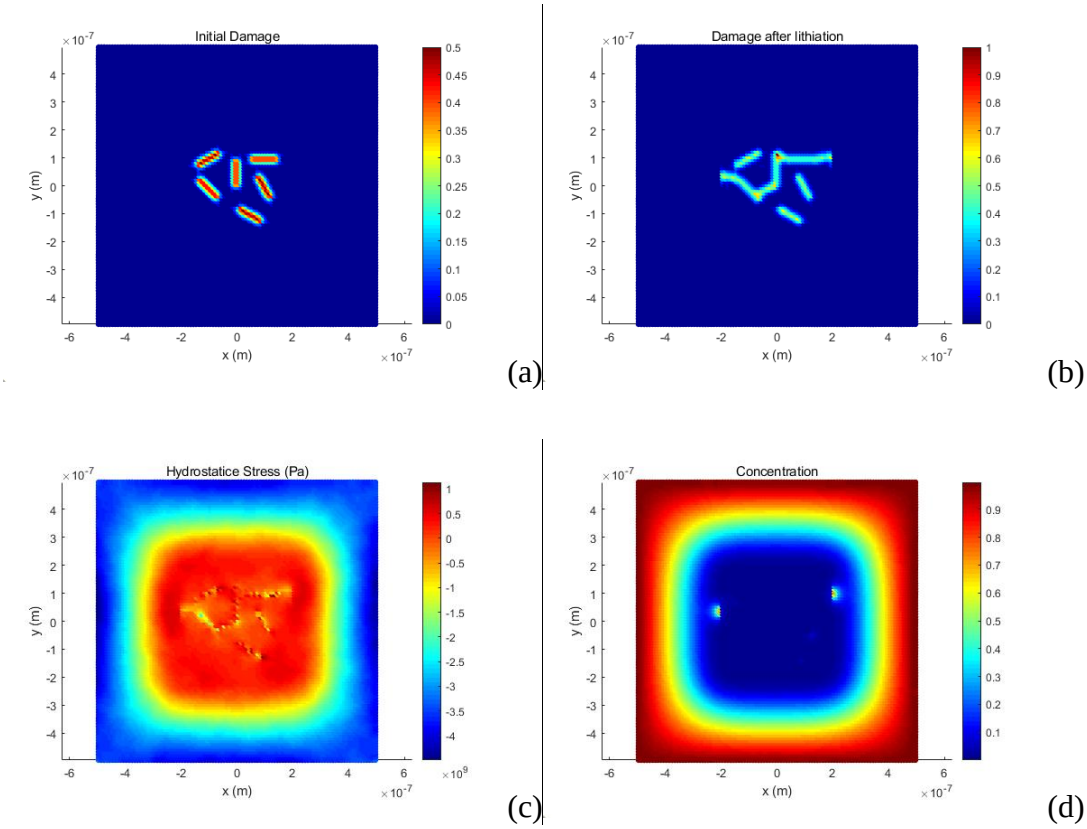

Figure 6.14. Results of plate with six cracks without considering material phase change: (a) Initial damage (b) Damage after deformation (c) Hydrostatic stress (d) Lithium ion concentration

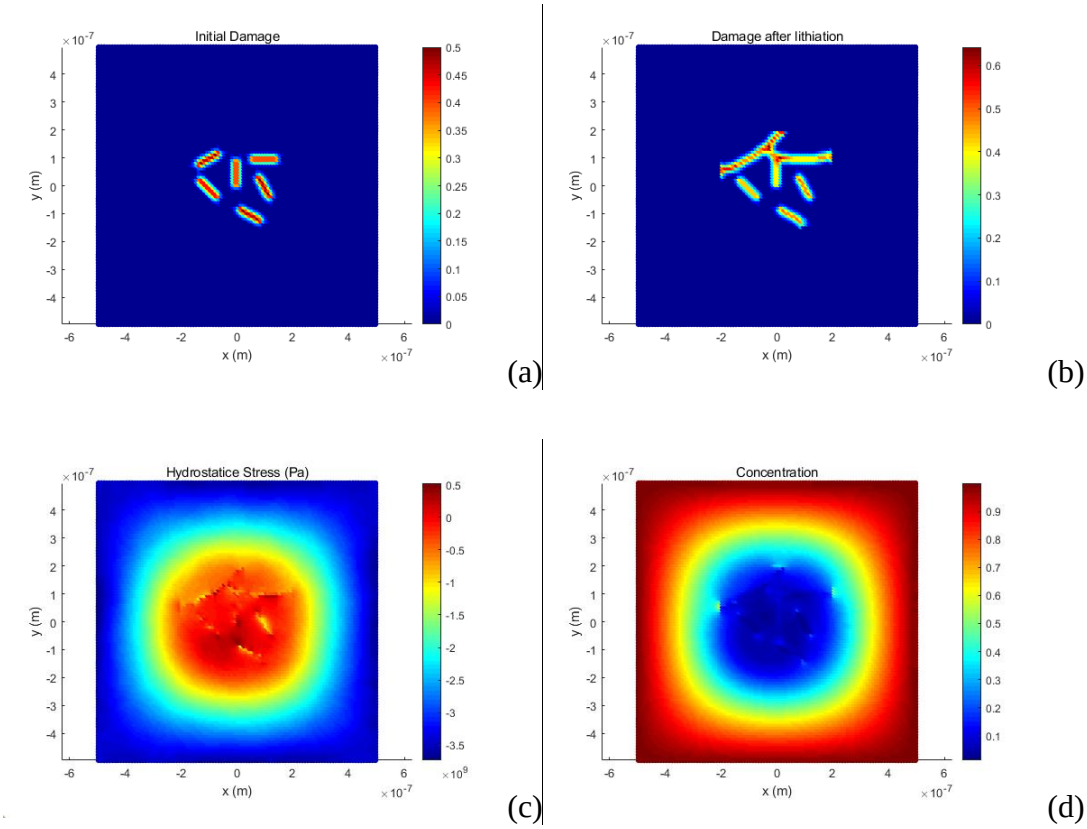

Figure 6.15. Results of plate with six cracks by considering material phase change: (a) Initial damage (b) Damage after deformation (c) Hydrostatic stress (d) Lithium ion concentration

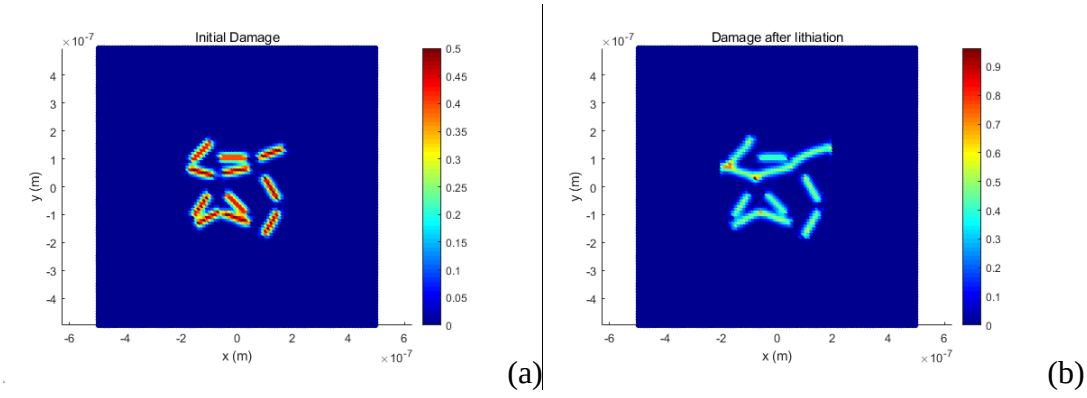

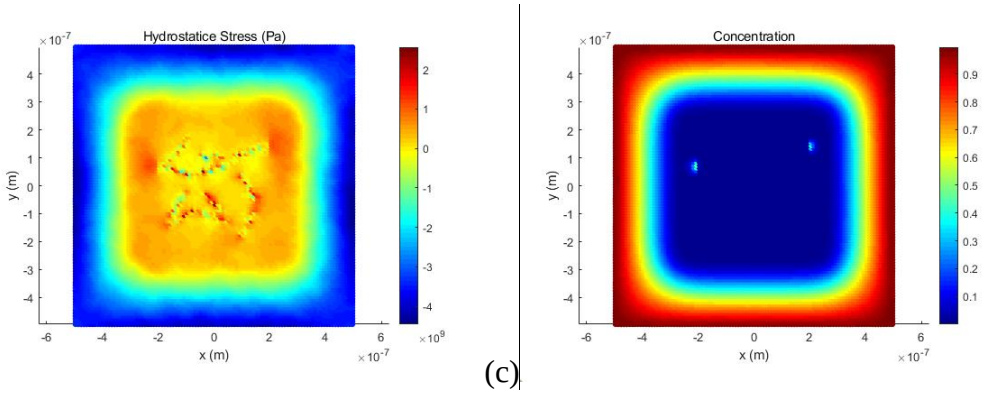

Figure 6.16. Results of plate with eleven cracks without considering material phase change: (a) Initial damage (b) Damage after deformation (c) Hydrostatic stress (d) lithium ion concentration

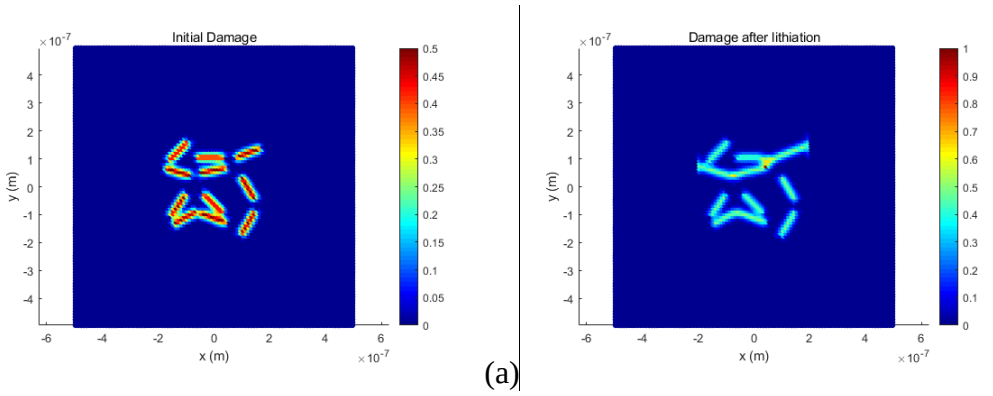

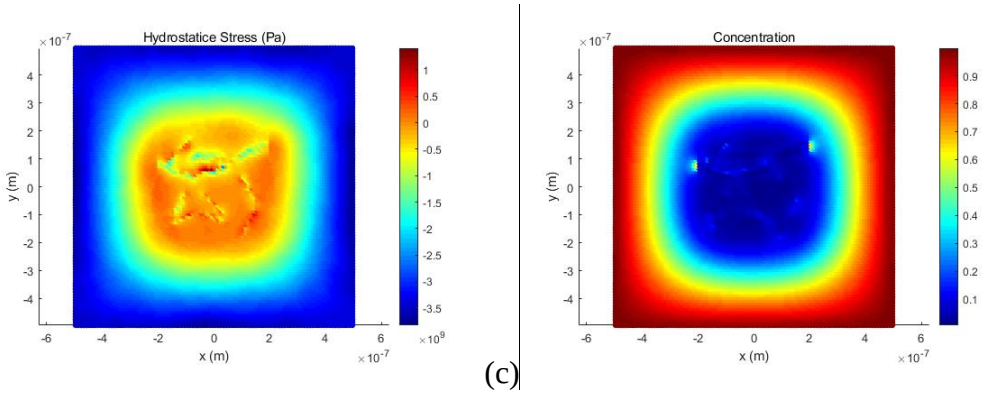

Figure 6.17. Results of plate with eleven cracks by considering material phase change: (a) Initial damage (b) Damage after deformation (c) Hydrostatic stress (d) Lithium ion concentration

6.7 Summary

The crack evolution inside the pre-damaged anode plate of lithium ion battery during one single charging process is provided in this chapter. Several cases in considering the material phase change during lithiation are investigated. In this study, the nonlocal numerical simulation method, peridynamics and the method for solving PDE, PDO, are introduced to the fracture analysis.

In PD, crack propagation depends on the condition of bond stretch. As discussed in chapter 3, once a bond exceeds the critical value, the bond will break and can not re-build the interaction. Damage is the percentage of "broken" bonds associated with a material particle. For cases without considering material phase change, crack propagates along high hydrostatic stress regions. However, for cases by considering material phase change, the hydrostatic stress is not the only criterion in damage evolution. Since Si transforms into lithiated Si during charging process, the critical stretch drops from 0.04 to 0.035. Hence, the material bonds of lithiated Si may reach critical value earlier as compared with material bonds of pure Si in high hydrostatic stress region. Therefore, for single material cases, cracks prefer to merge themselves first and then propagate from outer crack tips. For multi-material cases, crack merging and propagation at outer crack tips happen synchronously, which may lead to a different damage situation of the electrode plate. For multiple-cracks situation, since there is a stress reduction after merging of cracks, some small cracks that are surrounded by merged crack may not propagate.

Part of the electrode plate models in this study is provided by Zuo and Zhao in [71]. They applied the phase filed model to simulate crack evolution during lithiation process. Results of the cases by considering the factor of material phase change provided in this chapter reach a good agreement as compared with results produced by Zuo and Zhao.

Overall, PD provides a good estimation of damage evolution in lithium ion battery plates. It is possible to obtain information about crack propagation without

remeshing process and using sophisticated damage criteria. By applying this method, we can have a better understanding on failure mechanisms in lithium ion batteries.

7 FRACTURE ANALYSIS OF THREE DIMENSIONAL ELECTRODE STRUCTURE

7.1 Introduction

In order to avoid the fracture and failure of lithium ion batteries, some special structures, such as nano-sphere or nanowires, are applied on the surface of the electrode plate. However, these nanostructures may eventually be shattered and crushed after many battery cycling processes. In this chapter, the fracture evolution on the nanostructures of battery electrodes is under investigation. The background information about nanostructure of battery electrodes are provided in section 7.2. The mechanics of diffusion induced fracture and the governing equations to describe this phenomenon are provided in section 7.3. Fracture analyses of spherical energy storage particle and cylindrical nanowire are given in section 7.4 and 7.5, respectively. The discussion of the results is provided in section 7.6. Chapter summary is given in section 7.7.

7.2 Background

Performance of lithium-ion batteries mainly depends on material properties of anode, cathode and electrolyte. The carbon group elements: graphite (C), Si, germanium (Ge), tin (Sn) and their alloys, can be used as anode material of lithium ion batteries [106], [107]. In many commercial grade lithium-ion batteries, graphitic carbon is the main component of the anode material due to its low expansion induced by lithiation during battery charging [106]. However, the major limitation of the graphite carbon is its low electric capacity (372 $mAhg^{-1}$) by storing the lithium ions inside graphite sheets as (LiC_6) [62], [96], [97], which can not satisfy the demand of high electric capacity for marine batteries. Si and Ge, on the other hand, have relatively high theoretical capacities as compared to graphite carbon (3579 $mAhg^{-1}$ and 1625 $mAhg^{-1}$) [108], which seems to be the suitable candidates for anode materials in lithium-ion

batteries. However, both Si anode and Ge anode experience large volumetric change during battery cycling. Si anode is observed to have large volume expansion up to around 400% during charging process [66], [68]. Similar to Si anode, Ge anode also expands at around 370% in volume during lithitaion process [109]. Frequent cycling of the lithium-ion battery may lead to stress misdistribution, degradation and delamination of the battery components. It may lead to failure, or even pulverization, of structural integrity of battery anode.

Many efforts have been conducted to increase the electric capacity and avoid the defection of the electrode of lithium-ion batteries. Winter et al. pointed out that some metals, such as aluminum (Al), tin (Sn) and antimony (Sb) can store more lithium-ion than graphite carbon by forming alloys with lithium ion [106]. However, the newly formed alloyed anode will experience 500% volumetric expansion, which is the major barrier in the application of anode material of rechargeable lithium-ion battery. Gao et al. suggested a carbon nanotubes as anode material. Carbon nanotube is a tubular structure of graphite sheet with high conductivity, high tensile strength, high rigidity and low density. It increases the electric capacity up to around 600 $mAhg^{-1}$ without damage or pulverization. [110] Metal or their alloys can also be added into the nanotube in the composite form. Hence, the advantage of the high electric capacity in metal alloys and low volumetric change in graphite carbon can be applied in anode materials [111], [112]. However, carbon nanotubes experience lithium-ion capacity loss during cycling and linear voltage drop during discharging processes [106].

As compared with graphite carbon or carbon nanotube anode, Si shows superior performance in electrical capacity but suffer from pulverization due to large volumetric change during battery cycling. The fracture mechanic of Si anode is under frequent investigation in recent years. Liu et al. performed a thin Si film model to investigate the lithiation induced tensile stress and surface cracking by analytical method and FEM [69]. A compression-traction transition zone is observed which lies along the interface of electrode and electrolyte. The transition zone

mainly depends on the large volumetric change, plastic deformation and slow charging rate. Crack formation and propagation is led by the location of transition zone. The magnitude and profiles of tensile stress at the surface of lithiated Si zone depends on volumetric misfit strain, yield stress and modulus of unlithiated Si. Ryu et al. found that the large volume change during normal cycling process is always accompanied with pressure gradient [68]. High hydrostatic stress will affect the lithium-ion diffusion and fracture propagation in anode of the battery. Grantab and Shenoy provided a detailed investigation about pressure gradient factor on crack propagation in Si nanowires [9]. The cohesive zone method is applied to model fracture mechanics in Si nanowires. Since localized stress around the crack tip is higher than surrounding nanowire surface region, large amount of lithium-ion rush into crack tip region which causes relatively large volume expansion. Therefore, the hydrostatic stress around crack tip reduces. Zuo and Zhao used phase field method to study the stress evolution and crack propagation [71]. Several damaged anode models with different crack number and different crack orientations were considered to illustrate fracture mechanics in the battery anode. The pressure gradient depends on elastic modulus, partial molar volume, concentration, Poisson's ratio and the localized lithium-ion concentration. Gao and Zhou, on the other hand, applied the FEM and J-integral method to study the softening effect during lithiation process [72]. They also captured the high lithium-ion concentration at crack tip regions during charging process which lead to relaxation of hydrostatic stress in later diffusion process. The fracture evolution in Si nanowires also depends on the geometry of the structure. Ryu et al. also conclude that for Si nanowires with diameter smaller than 300nm will not fail during battery cycling, even for pre-damaged nanowires [68]. Due to large pressure gradient and large volume expansion, lithium ions can diffuse into Si nanowires rapidly and minor stress evolves during this process.

In this chapter, a three-dimensional cylindrical Si anode is selected as the configuration of the numerical simulation. The PD, as an alternative approach to FEM, is applied to investigate the fracture mechanics of the cylindrical anode of the

lithium-ion battery. The factors of pressure gradient and material phase change during lithiation (from Si to Li_xSi) are taken into consideration. Coupled field equations are applied to describe the charging process with the help of PDO.

7.3 Coupled diffusion-mechanical analysis formulation

Fick's Second Law indicates the basic principle of ion diffusion [103]. Since the anode material is Si, large volume expansion happens as lithium ions diffuse into the anode. Hence, the diffusion induced stress during battery cycling should be taken into account in Fick's Second Law. The strain component, ε_{ij}^{E}, by considering the influence of lithium-ion diffusion can be expressed as [9], [71]:

$$\varepsilon_{ij}^{E} = \varepsilon_{ij} - \alpha C_{avg}\delta_{ij} \tag{7.1}$$

where ε_{ij}^{E} refers to mechanical strain component as compared with total strain, ε_{ij}. α represents coefficient of diffusive expansion and C_{avg} represents current average concentration value of material points *i* and *j*. δ_{ij} is the Kronecker Delta. Recalling the three-dimensional stress-strain constitutive equation:

$$\begin{Bmatrix} \sigma_{xx} \\ \sigma_{yy} \\ \sigma_{zz} \\ \sigma_{xy} \\ \sigma_{xz} \\ \sigma_{yz} \end{Bmatrix} = \frac{E}{(1+\nu)(1-2\nu)} \begin{bmatrix} 1-\nu & \nu & \nu & 0 & 0 & 0 \\ \nu & 1-\nu & \nu & 0 & 0 & 0 \\ \nu & \nu & 1-\nu & 0 & 0 & 0 \\ 0 & 0 & 0 & \frac{1-2\nu}{2} & 0 & 0 \\ 0 & 0 & 0 & 0 & \frac{1-2\nu}{2} & 0 \\ 0 & 0 & 0 & 0 & 0 & \frac{1-2\nu}{2} \end{bmatrix} \begin{Bmatrix} \varepsilon_{xx} \\ \varepsilon_{yy} \\ \varepsilon_{zz} \\ 2\varepsilon_{xy} \\ 2\varepsilon_{xz} \\ 2\varepsilon_{yz} \end{Bmatrix} \tag{7.2}$$

and substituting Eq. (7.2) into Eq. (7.1), the coupled field normal stresses can be expressed as:

$$\sigma_{xx} = \frac{E}{(1+\nu)(1-2\nu)}\left[(1-\nu)\varepsilon_{xx} + \nu\varepsilon_{yy} + \nu\varepsilon_{zz}\right] - \frac{E}{(1-2\nu)}\alpha C_{\max} C \tag{7.3a}$$

$$\sigma_{xx} = \frac{E}{(1+\nu)(1-2\nu)}\left[\nu\varepsilon_{xx} + (1-\nu)\varepsilon_{yy} + \nu\varepsilon_{zz}\right] - \frac{E}{(1-2\nu)}\alpha C_{\max} C \tag{7.3b}$$

$$\sigma_{xx} = \frac{E}{(1+\nu)(1-2\nu)}\left[\nu\varepsilon_{xx} + \nu\varepsilon_{yy} + (1-\nu)\varepsilon_{zz}\right] - \frac{E}{(1-2\nu)}\alpha C_{\max} C \tag{7.3c}$$

where C is the current value of normalized lithium-ion concentration while $C_{\max}$ is the maximum value of lithium-ion concentration. The total normal strain in both three dimensions can be expressed in terms of displacement as:

$$\varepsilon_{xx} = \frac{\partial u}{\partial x} \tag{7.4a}$$

$$\varepsilon_{yy} = \frac{\partial v}{\partial y} \tag{7.4b}$$

$$\varepsilon_{zz} = \frac{\partial w}{\partial z} \tag{7.4c}$$

Local stresses rise along with lithium-ion diffusion at regions with high geometrical singularity. High pressure-gradients lead large amount of lithium-ion movement into these regions which increases the lithium ion concentration. As a result, stress releases as volume expands. Hence, the general Fick's Second Law should be reconstructed in consideration of pressure-gradient as:

$$\begin{aligned}\frac{\partial C}{\partial t} = {} & Mk_B T\left(\frac{\partial^2 C}{\partial x^2} + \frac{\partial^2 C}{\partial y^2} + \frac{\partial^2 C}{\partial z^2}\right) - \frac{MC\Omega}{N_A}\left(\frac{\partial^2 \tilde{\sigma}}{\partial x^2} + \frac{\partial^2 \tilde{\sigma}}{\partial y^2} + \frac{\partial^2 \tilde{\sigma}}{\partial z^2}\right) \\ & - \frac{MC\Omega}{N_A}\left(\frac{\partial C}{\partial x}\frac{\partial \tilde{\sigma}}{\partial x} + \frac{\partial C}{\partial y}\frac{\partial \tilde{\sigma}}{\partial y} + \frac{\partial C}{\partial z}\frac{\partial \tilde{\sigma}}{\partial z}\right)\end{aligned} \tag{7.5}$$

where M is molecular mobility, k_B is Boltzmann constant, T is absolute temperature, N_A is Avogadro's constant and $\tilde{\sigma}$ is the hydrostatic stress.

As described in chapter 6, anode will experience a material phase change during charging process. Zhang et al. pointed out that Si has different lithiated stages during charging process [102]. In the early stages, since lithium-ion concentration is low, Si will transform into partial Li_xSi. As the lithium-ion concentration increases, the partially lithiated Si will further transform into $Li_{15}Si_4$. Moreover, since some

material properties of lithiated Si, such as elastic modulus and fracture toughness, are lower as compared with pure Si, the lithiation process can also be regarded as a material softening process [104]. However, the size of partially lithiated Si region in battery anode is too small as compared with the anode geometry [102]. Therefore, in this study, only fully lithiated Si is considered

7.4 Fracture analysis of spherical energy storage particle

In this study, a spherical structure is selected to represent the energy storage particle with pre-existing penny shape crack. The materials of this particle, including pure Si and lithiated Si, are regarded as brittle material. Besides, the concentration values are normalized by maximum concentration as shown in Table 7.1. Before charging, the anode material remains pure Si. During charging process, maximum concentration of lithium ions will be subjected on all of the outer surface. Since the particle structure is free from any displacement constraints, it will experience a free expansion during the charging process. For three–dimensional bond-based PD, the Poisson's ratio is forced to be 1/4. Even though the real Poisson's ratio is provided in Tab. 7.1 below, the Poisson's ratio for both lithiated Si and pure Si in this study are kept as 1/4. For the cases which are considered in this study, the Poisson's ratio has limited influence on the fracture pattern. However, the actual Poisson's ratio can be applied by using ordinary state based peridynamic formulation for the equation of motion [113]. The total number of material points that applied in spherical model is 65752. Since the geometry of spherical energy storage particle is symmetric and the penny shape crack is horizontally oriented, the sample planes are selected along the longitude and latitude of the sphere as shown in red and black respectively in Fig. 7.1 to capture the lithium ion concentration and mechanical deformation.

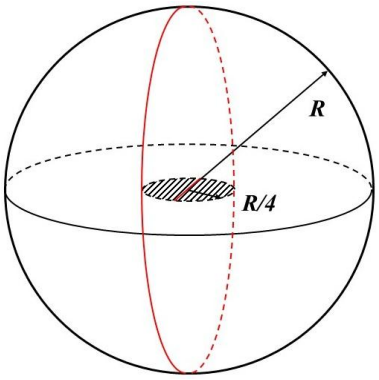

Figure 7.1. Spherical energy storage particle with pre-existing penny shape crack

Table 7.1. Geometrical parameters and material properties of energy storage models

Description	Parameter	Value	unit
Longitudinal length of cylindrical nanowire	L	0.5	μm
Diameter of cross section area of cylindrical nanowire	L	0.5	μm
Radius of spherical particle	R	0.5	μm
Elastic constant of silicon	E_{Si}	80	GPa
Elastic constant of amorphous $Li_{15}Si_4$	$E_{Li_{15}Si_4}$	41	GPa
Poisson's ratio of silicon	v_{Si}	0.22	N/A
Poisson's ratio of silicon	$v_{Li_{15}Si_4}$	0.24	N/A
Partial molar volume	Ω	8.5×10^{-6}	m^3mol^{-1}
Molecular mobility	M	500	$m^2J^{-1}s^{-1}$
Boltzmann constant	k_B	1.38×10^{-23}	$J\cdot K^{-1}$
Absolute temperature	T	300	K
Avogadro's constant	N_A	6.02×10^{23}	mol^{-1}
Critical strain for silicon	s_{c_Si}	0.04	N/A
Critical strain for amorphous $Li_{15}Si_4$	$s_{c\_Li_{15}Si_4}$	0.035	N/A
Maximum concentration	C_{max}	1.18×10^{4}	$mol\cdot m^{-3}$

A penny shape crack is located in the central region of the anode structure. The diameter of penny shape crack is half of the diameter of anode and the crack is horizontally oriented as shown in Fig. 7.1. As lithiation progresses, material at the anode surface region will become $Li_{15}Si_4$ first. Hence, surface region will experience relatively large deformation while the central region remains undeformed. Due to

this mechanical deformation, compressive stresses emerge on the particle surface regions, while tension stresses form in the particle central region especially at crack edge regions. Hence, according to Eq. (7.5), high hydrostatic stresses will affect the lithium ion distribution inside the spherical structure.

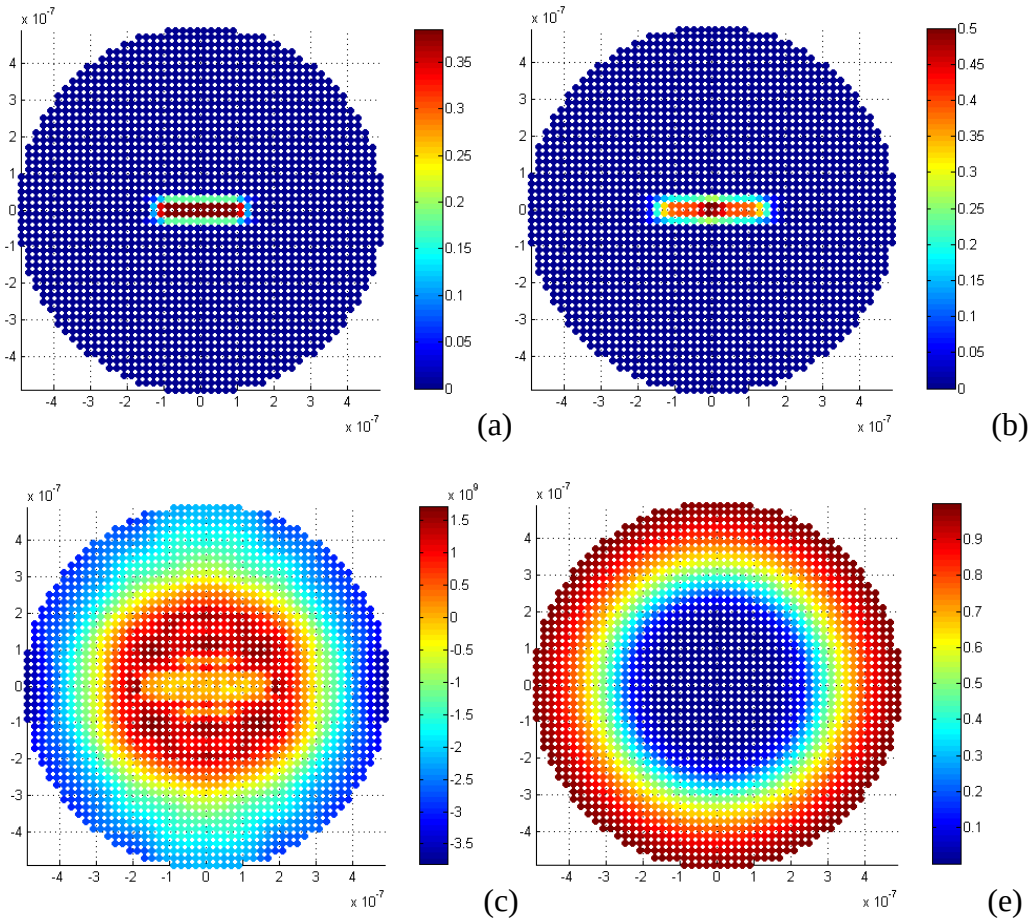

Figure 7.2. Results for penny shape cracked anode in *x-z* mid-plane: (a) Initial damage (b) Damage after deformation (c) Hydrostatic stress (*Pa*) (d) Lithium ion concentration

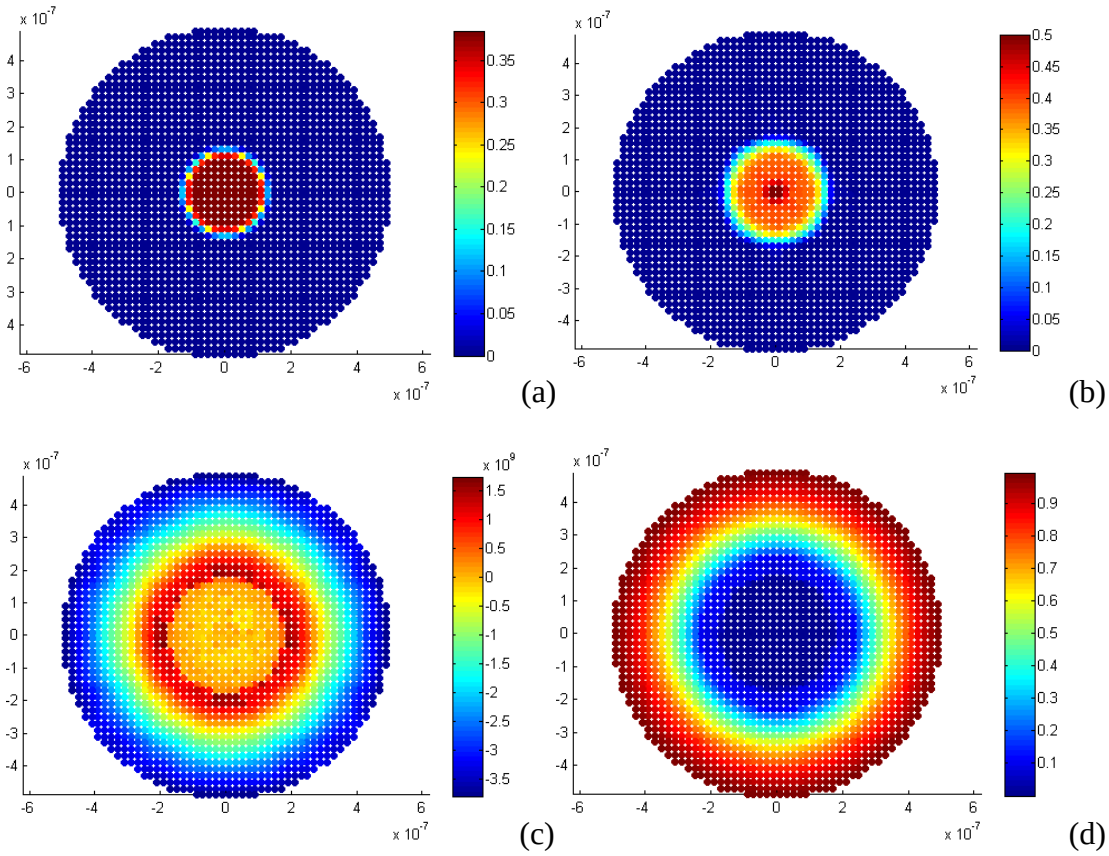

Figure 7.3. Results for penny shape cracked anode in *x-y* mid-plane (crack surface plane): (a) Initial damage (b) Damage after deformation (c) Hydrostatic stress (*Pa*) (d) Lithium ion concentration

The results of lithium ion diffusion and diffusion induced deformation during charging process are shown in Fig. 7.2 and Fig. 7.3. In order to have a clear understanding of the lithiation induced damage in three-dimensional structure, results are shown in both *x-z* plane and *x-y* plane (crack surface plane). Due to the heterogeneous distribution of deformations inside the spherical structure, high hydrostatic stresses rise at the edge of penny shape crack where high geometrical singularity lies as shown in Fig. 7.2c and Fig. 7.3c. As lithium ions keep diffusing into the spherical structure, the lithium ion concentration at the crack edge regions starts to rise as compared with surrounding regions. However, since the penny shape crack just starts to propagate as shown in Fig. 7.2b and Fig. 7.3b, the change of lithium-ion concentration may not be clear from the concentration plot. The

hydrostatic stress value around crack edge region is around 1.5GPa, which leads to the bond stretch far beyond the critical stress [114]. Hence the penny shape crack will continue to propagate unit the bond at the crack tip regions reduce below the critical stretch value shown in Table 7.1.

7.5 Fracture analysis of cylindrical silicon nanowire

As discussed in the literature [9], [68], special Si structures, such as Si nanowire, are produced in order to avoid the fracture formation and propagation of the battery anode. Hence, in this section, several different pre-damaged models are provided to investigate the fracture evolution in the Si nanowire. The Si nanowire is represented by a cylindrical shape structure. However, different from the spherical model in section 7.4, the cylindrical structure is not symmetric in all orientations. Hence, the fracture analysis of cases with different crack orientations are separately discussed in the following sections. The total number of material points in cylindrical Si nanowire mode is 98800.

7.5.1 Single penny shape crack along horizontal axis

A cylindrical shape structure with diameter L as shown in Fig. 7.4 is selected to represent a Si nanowire. A penny shape crack (marked as shadow lines in Fig. 6) with $L/4$ in diameter is horizontally oriented at the center of the cylindrical structure. Material properties of the cylindrical anode is the same as the spherical model in Table 7.1. Before charging the battery, the cylindrical material is pure amorphous Si. During charging process, lithium ion with maximum concentration is applied to the outer surface of the cylinder structure. As a result, the material properties will change and the cylindrical structure will deform. Similar to spherical model, the results are shown in two plane views in order to capture the detailed fracture information.

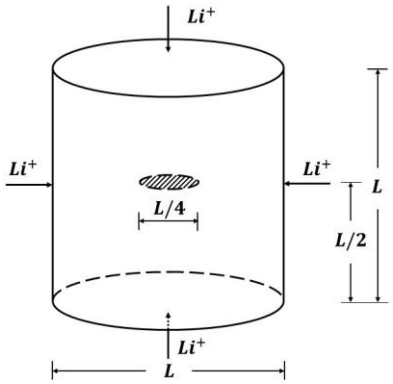

Figure 7.4. Cylindrical anode structure with pre-existing horizontal crack

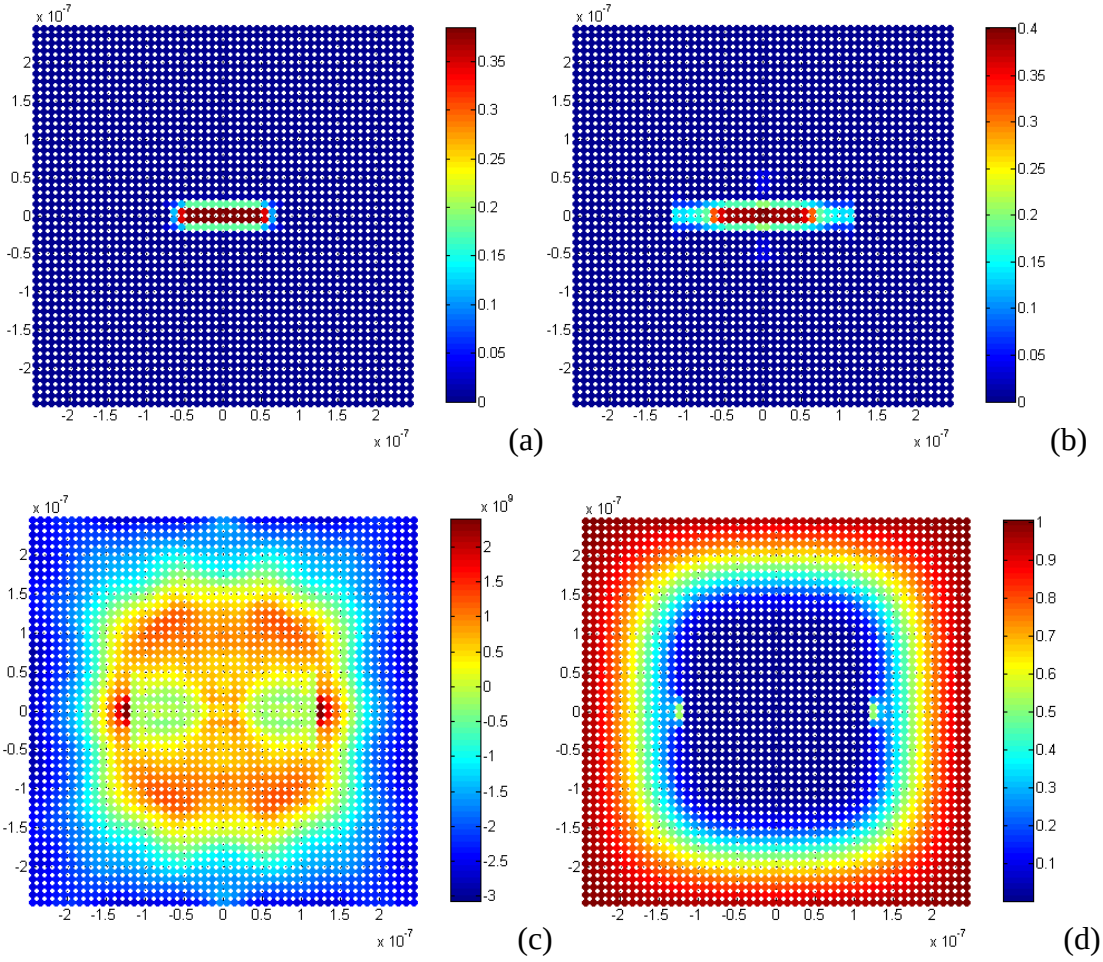

Figure 7.5. Result plots of a cylinder with a single horizontal crack in *x*-*z* mid-plane: (a) Initial damage (b) Damage after deformation (c) Hydrostatic stress (*Pa*) (d) Lithium ion concentration

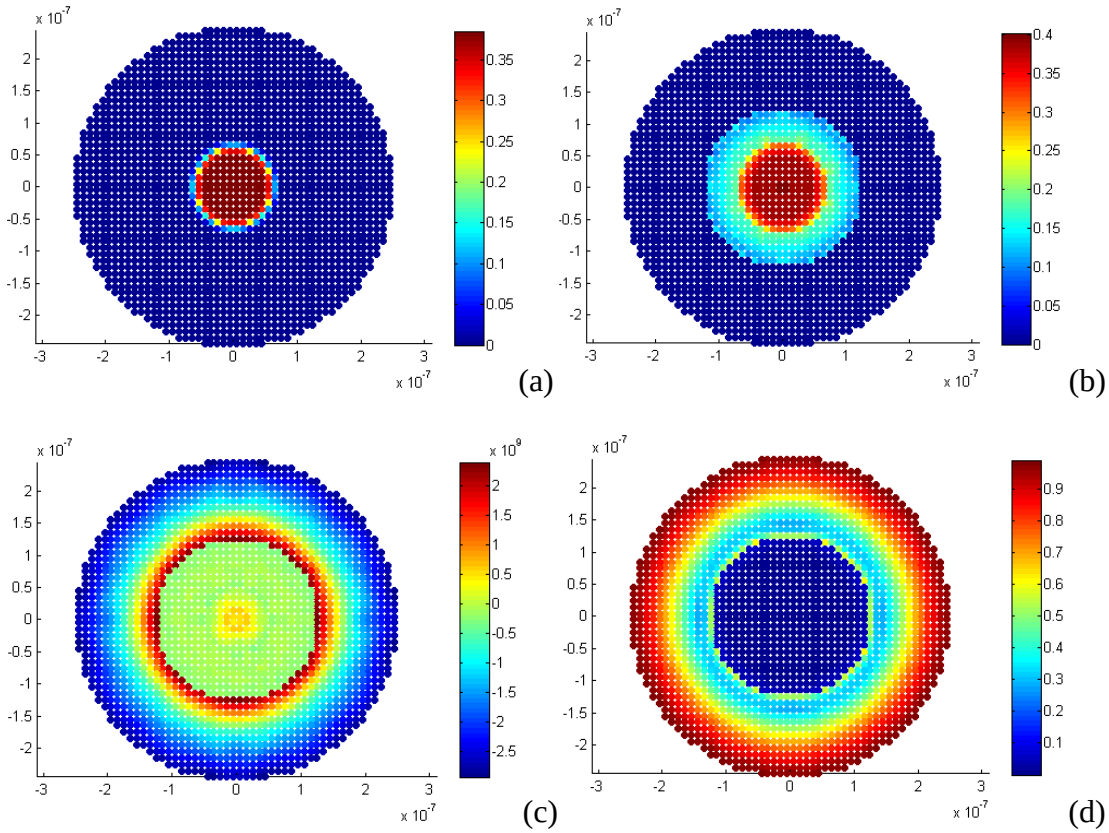

Figure 7.6. Result plots of a cylinder with a single horizontal crack in *x*-*y* mid plane (crack surface plane): (a) Initial damage (b) Damage after deformation (c) Hydrostatic stress (*Pa*) (d) Lithium ion concentration

Due to material phase change during charging process, material points on the surface regions will expand as amorphous Si turns into lithiated Si while material points in the central regions remain undeformed. Therefore, the hydrostatic stress in outer surface is shown as compression stress which is marked as blue in Fig. 7.5c and Fig. 7.6c. For hydrostatic stress in inner cylinder is shown as tensile stress which is marked as red, especially at the crack tip region. In this case, the crack propagation is evident. The penny shape crack edge lies close to the material phase boundary as shown Fig. 7.5b and Fig. 7.6b. Hence, according to Eq. (7.5), lithium ion concentration of crack edge regions is relatively higher than surrounding regions as shown in Fig. 7.5d and Fig. 7.6d. Since the hydrostatic stress at the crack tip region is around 2.3GPa, the bond stretch calculated by relative position of associated

material points will exceed the critical value. Hence, the crack propagation will not stop until the stretch value of the bonds at this crack edge regions reduces below the critical value shown in Table 7.1.

7.5.2 Single penny shape crack along vertical axis

Different from spherical energy storage particle model as described above, the cylindrical Si nanowire model may have different fracture results in radial direction and longitudinal direction. Hence, in this case study, the penny shape crack along longitudinal (z-direction) is under investigation. A penny shape crack with $L/4$ in diameter is located at the central position of the cylindrical model as shown in Fig. 7.7. However, different from the case study in section 7.5.1, the crack is vertically oriented (or along the x-z mid-plane). Before charging the lithium ion battery, the cylinder is composed of pure amorphous Si and the lithium ion concentration is zero throughout the whole structure. During charging process, lithium ion concentration with maximum value is applied to all the outer surfaces of the cylinder. As the lithium ion concentration increases, pure Si will transform into fully lithiated Si, which leads to volume expansion. Stress and damage induced by this volume expansion are shown in Fig. 7.8 and Fig. 7.9.

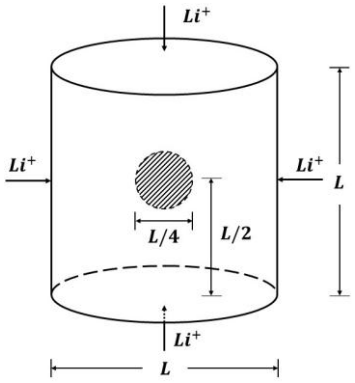

Figure 7.7. Cylindrical anode structure with a pre-existing vertical crack

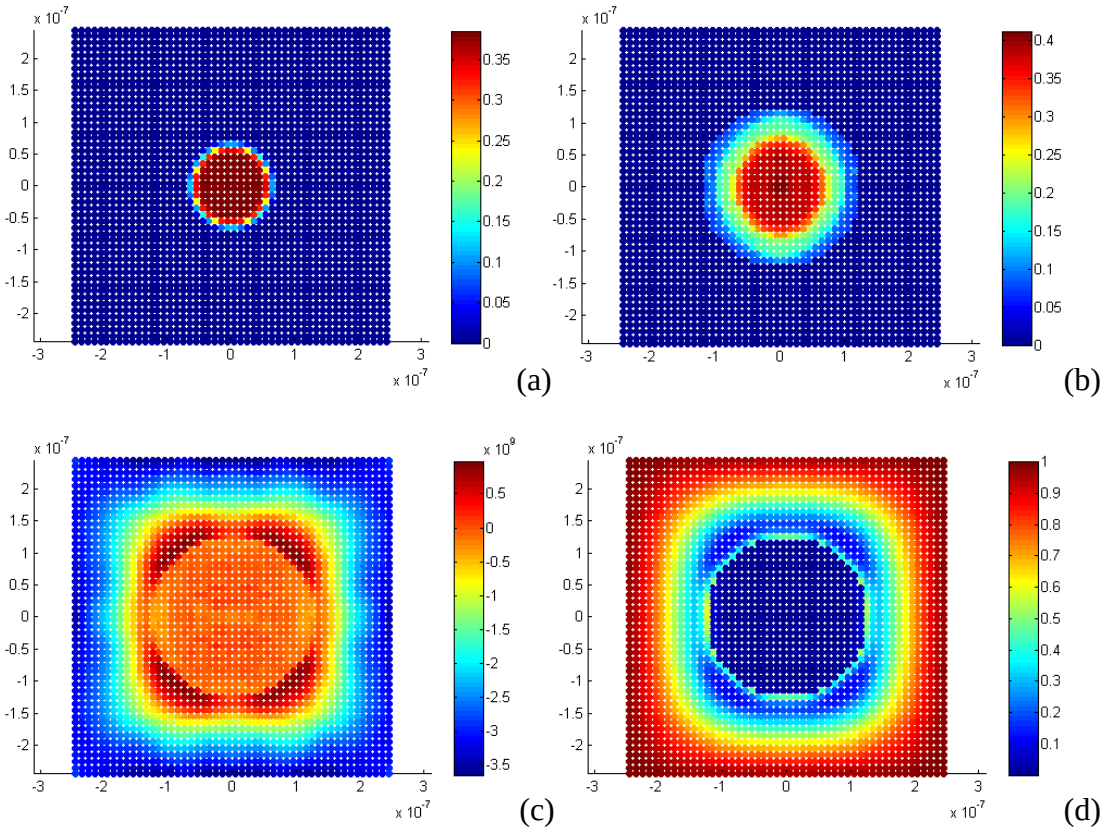

Figure 7.8. Result plots of a cylinder with a single vertical crack in *y*-*z* mid-plane: (a) Initial damage (b) Damage after deformation (c) Hydrostatic stress (*Pa*) (d) Lithium ion concentration

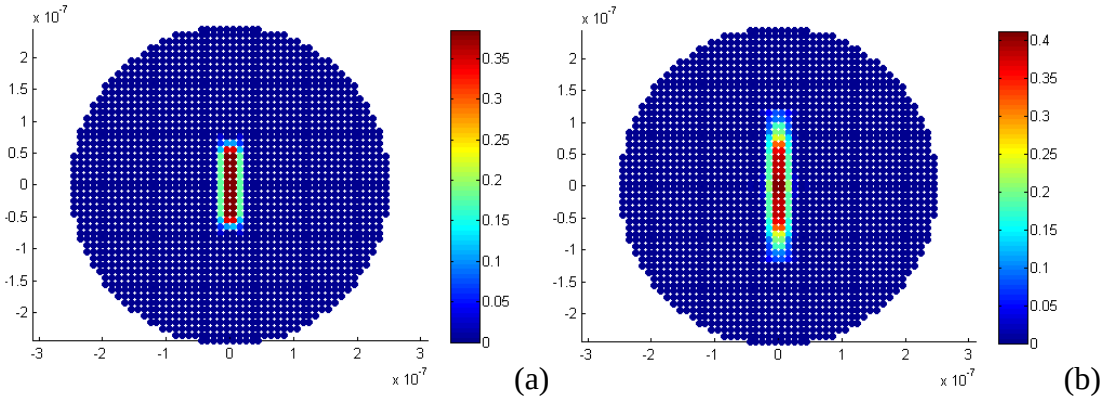

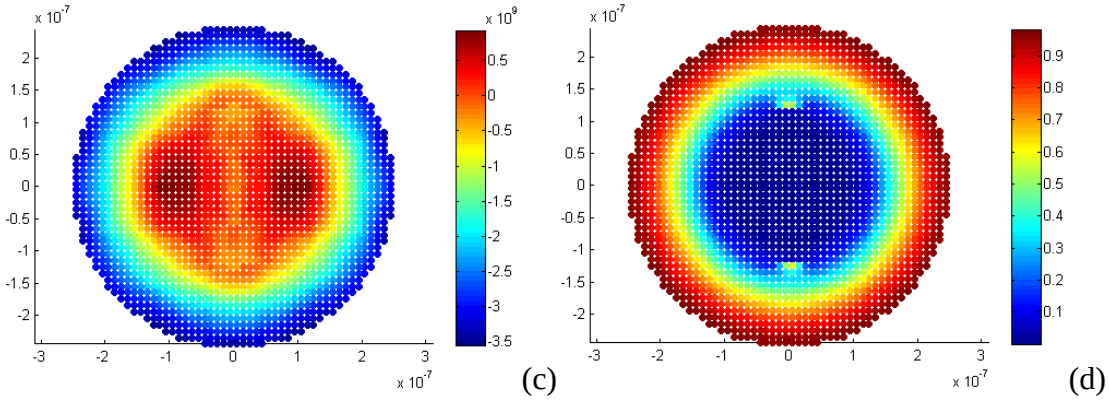

Figure 7.9. Result plots of a cylinder with a single vertical crack in *x*-*y* mid plane: (a) Initial damage (b) Damage after deformation (c) Hydrostatic stress (*Pa*) (d) Lithium ion concentration

The results were plotted in *x*-*z* mid-plane view (Fig. 7.8) and *x*-*y* mid-plane view (Fig. 7.9). During the charging process, the material points in outer surface regions get lithiated first and expand, while material points in the central region remain undeformed. As a result, a deformation gradient from outer surface to central cylinder is produced and hydrostatic stresses increase especially at crack edge regions according to Eq. (3.11~3.18). In Fig. 7.8c and Fig. 7.9c, compression stress appears at the outer surface region, which is represented as blue color in the figure. Tensile stresses exist at the central cylinder region especially at crack edge regions where geometrical singularity locates, which is represented as red color in the figure. As crack propagates, the crack will open which causes relatively high tension stress near crack surface. Since the crack propagates close to material phase boundary, the lithium ion concentration will be relatively higher than surrounding regions according to Eq. (7.5) as shown in Fig. 7.8d and Fig. 7.9d.

7.5.3 Twin penny shape cracks along horizontal axis

The case studies in section 7.5.1 and 7.5.2 focused on the fracture analysis of single crack which lies on the symmetrical plane of the cylindrical structure. Hence, due to the symmetric geometry and loading, the penny shape crack propagates along the crack surface plane. However, in reality, the crack can locate at any position inside

the battery electrode. Hence, in this case study, the Si cylinder with cracks which do not lie on the symmetric plane is under investigation. As shown in figure below, twin cracks are located in the central region with a diameter equals to $L/4$ and the distance between these cracks is also $L/4$. Both of the cracks are horizontally oriented. Before charging the battery, the cylindrical nanowire is composed of pure amorphous Si only. During charging process, lithium ion with maximum concentration is applied on all the outer surface of the cylinder. As a result, the material points on the surface get lithiated and expand while the material points in central region remain undeformed. The heterogeneous deformation lead to the increase of hydrostatic stress in regions with geometrical singularity and speed up the diffusion as shown in Fig. 7.11.

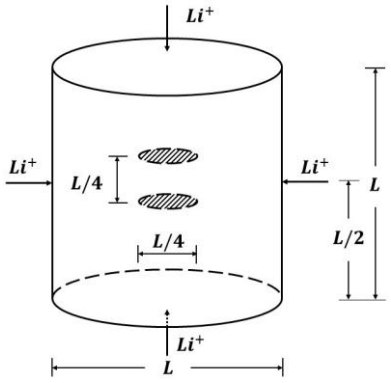

Figure 7.10. Cylindrical anode structure with pre-existing twin horizontal cracks

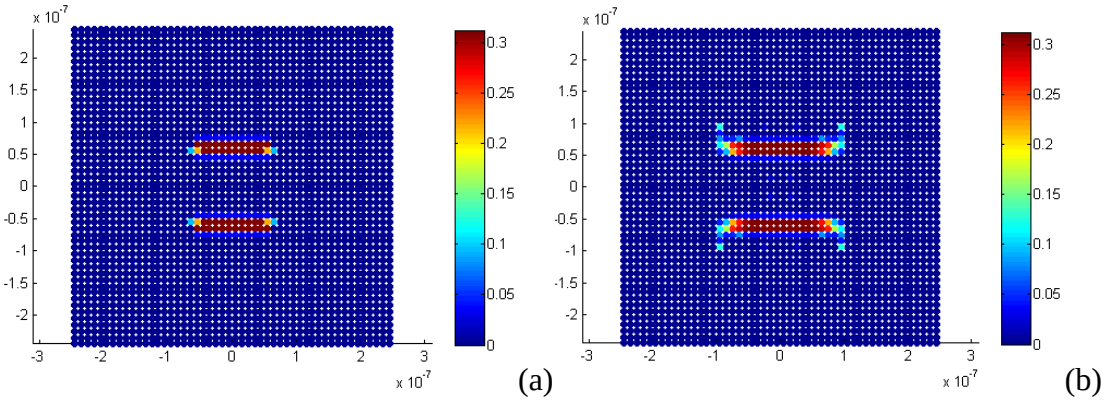

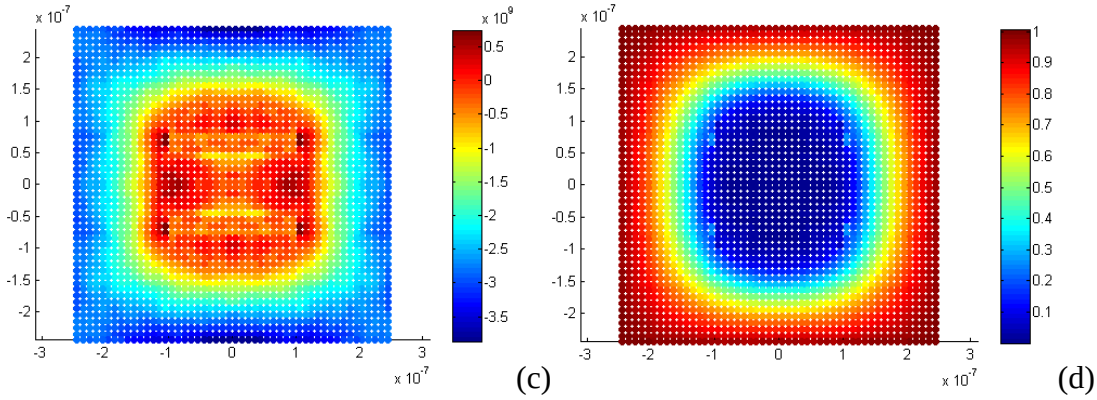

Figure 7.11. Result plots of silicon cylinder with twin horizontal cracks in *x*-*z* mid-plane: (a) Initial damage (b) Damage after deformation (c) Hydrostatic stress (*Pa*) (d) Lithium ion concentration

By comparing with the case in section 7.5.1, the crack propagation is different. At initial charging process, both cracks propagate along the crack surface plane. However, as the charging process continues, the upper crack propagates upward from the edge and the lower crack propagates downward from the edge. These cracks repel from each other as shown in Fig. 7.11b. Due to the heterogeneous volume expansion inside the cylinder, a deformation gradient forms from surface of the cylinder to center of the cylinder. As a result, the hydrostatic stress increases especially at the crack edge regions according to Eq. (3.11~3.18). Since material points at the surface region experiences expansion during charging process, the material points located in central region will suffer from compression stress which is represented in Fig. 7.11c. The expansion of these material points introduces a tension stress for the material points in central region especially around the crack edge region as shown in Fig. 7.11c. Since the crack edge is closer to the material phase boundary, lithium ions will diffuse into regions around the crack edge with higher priority according to Eq. (7.5). Hence, the lithium ion concentration is relatively higher than surrounding regions as shown in Fig. 7.11d.

7.5.4 Twin penny shape cracks along vertical axis

After the analysis of twin cracks along radial direction, the case with twin cracks along longitudinal direction is also considered. In this section, twin vertically oriented cracks are arranged at the center region of the Si cylinder as shown in Fig. 7.12. The diameter of both cracks is $L/4$ and the distance between these cracks is also $L/4$. Before charging the battery, the Si cylinder is made of pure amorphous Si. During charging process, lithium ion with maximum concentration is applied on all the outer surfaces of the cylinder. Hence, the material particles on the outer surface region get lithiated and expand. Then, it will influences the lithium ion diffusion and hydrostatic stress inside the cylinder which is shown in Fig. 7.13.

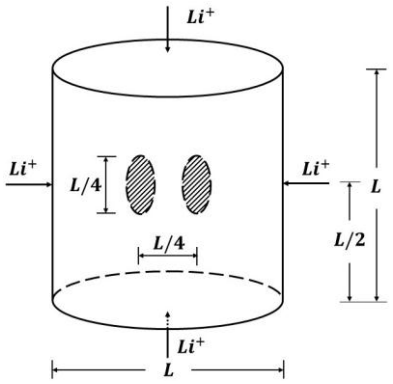

Figure 7.12. Cylindrical anode structure with pre-existing twin vertical cracks

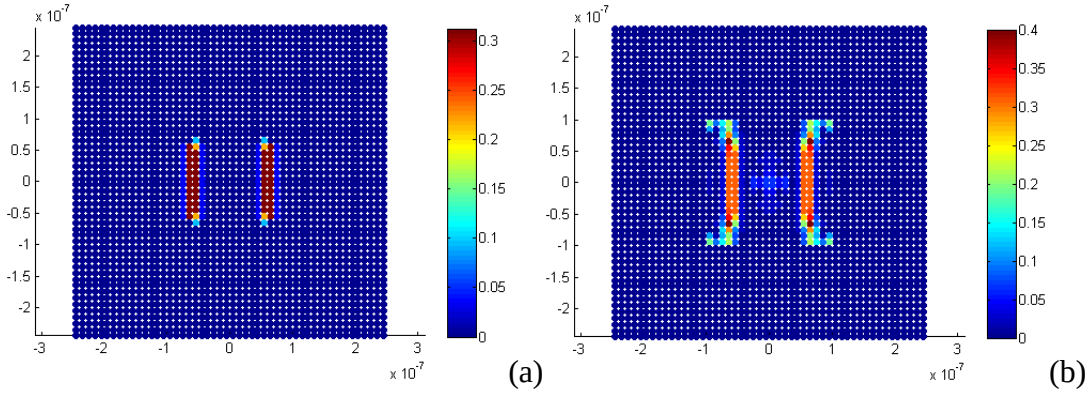

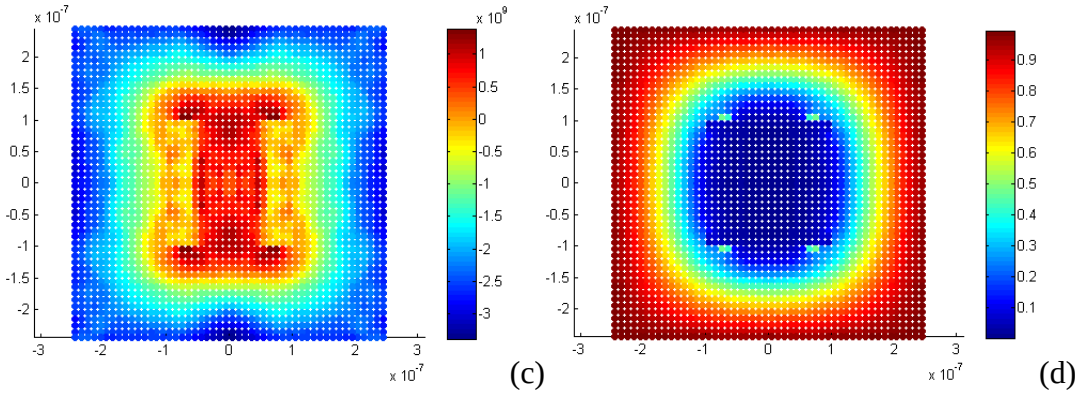

Figure 7.13. Result plots of a cylinder with twin vertical cracks in *x*-*z* mid-plane: (a) Initial damage (b) Damage after deformation (c) Hydrostatic stress (*Pa*) (d) Lithium ion concentration

Fig. 7.13a shows the initial damage in the view of *x*-*z* mid-plane. During early charging process, penny shape cracks propagate along their crack surfaces. However, as charging process continues, the left crack propagates towards left and the right crack propagates towards right. Generally, these cracks repel each other as shown in Fig. 7.13b. Heterogeneous volume expansion leads to the formation of deformation gradient from surface region to central region. Therefore, hydrostatic stress increases inside the cylinder according to Eq. (3.11~3.18). The heterogeneous expansion introduces lithiation bring compression stress on material points at cylinder's surface region which is marked in blue as shown in Fig. 7.13c. As a consequence, the material points at central cylinder region suffers from the tension stress which is marked in red. Since crack edge reaches the material phase boundary, the lithium ion diffuses into material points at the crack edge region first. Hence, a relatively high lithium ion concentration at the crack edge region as compared with its surrounding region can be observed in Fig. 7.13d.

7.6 Discussion

From the results shown above, the lithiation can influence the fracture behaviour of the battery electrode. In the perspective of PD, crack propagation is calculated based

on the bond stretch which depends on the deformation of the structure. Hence, the crack propagation generally depends on deformation which is induced by lithiation during battery charging. Since the amorphous Si transforms into lithiated Si, the material properties also changes which leads to changes of critical bond stretch. The comparison of fracture analysis with and without material phase change is discussed in chapter 6 and the previous works [113], [115]. In this chapter, since the material phase change during charging process is also under consideration, the critical bond stretch is also influenced by the material properties.

For some electrode structures with a symmetric geometry, the way of crack propagation is different by considering the position of the initial crack. If the initial cracks lie on the symmetric plane, cracks will propagate along the crack surface plane since the geometry and loading are symmetric. However, if the initial cracks does not lie on the symmetric plane, the newly formed cracks may not align with initial crack. In the twin cracks cases, the two dimensional penny shape cracks turn into three dimensional bowl shape cracks after charging the battery. This is because of the material softening phenomenon during lithation as described in [104]. Due to the increase of lithium ion concentration, amorphous Si at crack edge regions will be transformed into $Li_{15}Si_4$. As a consequence, the critical bond stretch reduces as shown in Table 7.1. Hence, the bonds at crack edge region reaches critical values earlier which leads the crack edge propagation towards high lithium ion concentration region. High hydrostatic stress exists between the twin cracks as shown in Fig. 7.11c and Fig. 7.13c and the bonds located in these regions may not reach critical value. However, high hydrostatic stress shows a potential to merge these two cracks into one larger crack as shown in Fig. 7.13b.

7.7 Summary

In this chapter, PD in conjunction with the three dimensional PDO approach are introduced as the numerical method in fracture mechanics of lithium ion batteries. Two models, spherical energy storage particle and cylindrical nanowire, with

different pre-existing cracks are considered. According to numerical results, the crack propagation is usually led by high hydrostatic stress which reflects on bond breakage in PD. Besides, the material phase change from amorphous Si to lithiated Si also influences the crack propagation. Since the model geometry and loading are symmetric, the direction of crack propagation also depends on the initial crack position. High hydrostatic stress also lies between the cracks in twin crack cases, which means twin cracks have a potential to merge into one larger crack.

As a summary, PD has a capability for the estimation of three dimensional damage evolution in lithium ion battery electrodes. In PD, the damage formation and evolution can be simplified without remeshing or applying sophisticated damage criteria. By using peridynamics, we can have a better understanding of the failure mechanisms during the cycling operation of lithium ion batteries.

8 Conclusions

8.1 Summary of peridynamic theory

The PD provides an alternative method in the studies of solid mechanics especially the fracture analysis. Different from methods that are based on CCM, PD uses spatial integral equations to describe the motion of the material body. This brings a great advantage for the analysis of material structure with discontinuities such as cracks and kinks. Generally, in PD, material structure is uniformly discretised by finite amount of material points with certain amount of volume, instead of elements that are used in FEM. Material points can build up interactions with surrounding particles through bonds within the horizon. Based on this model, the damage definition can be reflected on "bond breakage", i.e. the invalidation of bonds. For prototype microelastic brittle material, once the material loses the interaction with the member point within its horizon, damage or fracture occurs and the interactions can not recover by themselves. Therefore, without pre-defined crack propagation path or pre-defined cohesive zone element, damage can be automatically calculated during structural deformation. Moreover, the speed, direction and branching of the crack can also be captured easily.

PD can also be applied in multi-field physics. In this thesis, the PD has shown its capability in describing the thermal conduction and ion diffusion. For more complicated systems, such as coupled thermomechanical deformation and lithiation induced fracture, PD also have a good estimation as discussed in chapters 5, 6 and 7. In these problems, we may encounter several PDEs with different orders. This may cause difficulties in numerical simulation especially around crack region and boundaries. By applying the PDO, these PDEs can be transformed into spatial integral equations. This can overcame the problem that PDEs do not have definition over discontinuous regions, such as cracks and boundaries.

Overall, PD is an alternative approach for the numerical simulation of marine battery electrodes. In this thesis, from pure mechanical deformation to fully coupled diffusion induced fracture, we can have a better understanding of the failure mechanisms during the cycling operation of marine batteries. It can contribute significantly to the design, manufacture and maintenance of battery in marine industry.

8.2 Achievements against the objectives

The main objective of this thesis is build up PD models and framework to investigate the fracture evolution in the marine batteries as presented in section 1.2. From two dimensional cases to three dimensional cases and from partially coupled problems to fully coupled problems, the researches gradually becomes complicated and more representative of the situations in real life. The major achievements of the thesis against the research objectives are listed below:

- Based on PDO, the PDEs were transformed into spatial integral equations. Hence, the coupled field equations can be significantly simplified by these PD functions and they have been applied into the fracture analysis of SOFC and lithium-ion batteries in chapters 5, 6 and 7.

- A two dimensional PD model for thermomechanical analysis of SOFC was introduced. Since the normal operational temperature of SOFC is very high, the influence of deformation on temperature is negligible. Hence, this model can be regarded as a partially coupled model. In order to validate the PD model, results generated by PD are compared with those obtained by FEM and they have excellent agreement in both displacement and hydrostatic fields. The fracture analysis of the SOFC plate is split into several cases according to the strength of interaction between electrode particles and electrolyte particles. For different interaction strengths, the position and speed of crack formation and evolution may be different.

- A two dimensional PD model for describing lithiation induced fracture in lithium ion battery electrode plates was developed. From single crack case to multiple randomly oriented cracks cases, several damage situations that may occur inside the electrode plates are numerically simulated. Cases that considered the material phase change during charging process are also compared with those without material phase change. As a result, the fracture evolution of these two situations may not always the same and It depends on both material properties and hydrostatic stress.

- Two three dimensional PD models: spherical energy storage particle and cylindrical Si nanowire, were developed to represent the special energy storage structures embedded on the electrode surface. The single and twin penny shape cracks in different orientations are investigated. Moreover, the material phase change factor was also considered. Results shows the PD has a very good capabilities in three dimensional fully coupled fracture analysis.

8.3 Gaps and recommended future work

In this thesis, the electrode material in the simulations is regarded as isotropic elastic material for simplicity. However, some of the material properties of the electrode and electrolyte, such as elastic modulus and coefficient of expansion, may be influenced by the operating temperature and lithium ion concentration in reality. Besides, electrode and electrolyte may experience plastic deformation, especially at regions with high geometrical singularity such as cracks and boundaries.

Since the SOFC electrode plate is a porous electrode plate, it just shows the fracture situation in current electrode layer. Since the geometry of neighbouring layers might not always be the same as the current electrode layer, it is necessary to take into account the influence of different layers on current electrode layer for more accurate fracture analysis.

In this thesis, the PD particularly refers to bond-based PD. As a special case of ordinary state-based PD, the Poisson's ratio is strictly limited at 1/3 for two dimensional model and 1/4 for three dimensional model. Although it may not influence the fracture formation and evolution dramatically, it can cause difference in structural deformation and stress fields. Moreover, bond-based PD can not deal with problem with plastic deformation. As a result, the material of electrode has to assume to be elastic material.

In consideration of these gaps in my study, some future research plan are list below:

- Continue to study the PD especially the ordinary state-based PD and non-ordinary state-based PD, so that we can use this theory to describe the plastic deformation. Moreover, more realistic material properties can be applied into the research which increase the accuracy of the numerical simulation.

- Create a three dimensional PD model of SOFC. In this model, the structure of anode (Ni), cathode (LSM) and electrolyte (YSZ) are defined, so that a small SOFC unit is created. Material properties that depend on operating temperature should also be taken into consideration. Similar with the current study, the difference of material failure induced by different interaction strength between electrode and electrolyte particles should also be under investigation.

- Continue to study the lithiation induced fracture in lithium ion batteries. Based on three dimensional cylindrical Si nanowire model, develop an axisymmetric model. Hence, the three-dimensional cylindrical model will be simplified into a two dimensional model, which can reduce the computation time significantly. On the other hand, try to optimise the coupled field equations and main parameters, such as normalisation of the equation. Therefore, the large difference on critical time step size between mechanical deformation and lithium ion diffusion can be overcome.

- Try to apply the PD into realistic engineering programs, especially in fracture analysis. Moreover, I need to seek more opportunities to make real fracture experiments to validate the PD and numerical simulations.

8.4 Novelty and contribution to the field

Traditional numerical simulation methods that are based on CCM, such as FEM, FVM and CZM, have applied a local interaction framework. Material structure is meshed by using elements and PDEs are applied to describe the motion of nodes on the elements. However, PDE does not have definition on non-continuous regions such as cracks and kinks, which brings limitations for fracture analysis. PD, on the other hand, has built up a framework by nonlocal interactions. Without meshing, material structure is discretised by finite number elements. The motion of material points are described by spatial integral equations. Interactions between material points are represented by bonds which have simplified damage definition. Hence, PD has advantages in fracture analysis with respect to classical methods. Within the framework of PD, the PDO is studied in detail. Based on nonlocal property of the framework, the PDEs can be transformed into spatial integral equations within the horizon. Therefore, the gradient of deformation, hydrostatic pressure, temperature and concentration can be directly represented by PD which make the numerical simulation more convenient and efficient.

Many of efforts have been devoted to the fracture analysis of SOFC. However, the researches that concentrate on fracture analysis of SOFC can rarely be found in the literature. In this thesis, the PD model of two dimensional electrode plate is considered for fracture analysis of SOFC for the first time in the literature. Different from numerical analysis methods in CCM, damage formation and propagation depends on the relationship between bond stretch and critical bond stretch. Hence, the damage can be automatically captured without pre-defined crack propagation path or cohesive elements as described in the literature. As a result, the accuracy and efficiency of the numerical simulation have been improved by using PD which will

contribute to the design, manufacture, failure detection and life span prediction of the SOFC.

Lithiation induced fracture during normal battery cycling in lithium ion batteries is under excessive investigation with various numerical simulation methods based on CCM. However, in view of PD, this study is a pioneering work in this area. In this thesis, several PD models either two-dimensional or three-dimensional are established to investigate the fracture evolution inside the pre-damaged electrode. In these researches, the relationship between lithium ion concentration and hydrostatic stress is presented in PD. The cases with single and multiple cracks and the influence among the cracks during charging process are discussed within the framework of PD. With the help of PD, the degradation of lithium ion batteries during charging process is shown in detail. This study contributes to the performance development of marine lithium ion batteries.

8.5 Research outputs

- **Published journal papers**

  Vazic, B., **Wang, H.**, Diyaroglu, C., Oterkus, S. and Oterkus, E., 2017. Dynamic propagation of a macrocrack interacting with parallel small cracks. *AIMS Materials Science*, *4*(1), pp.118-136.

  Wang, H., Oterkus, E., Celik, S. and Toros, S., 2017. Thermomechanical analysis of porous solid oxide fuel cell by using peridynamics. *AIMS Energy*, *5*(4), pp.585-600.

  Wang, H., Oterkus, E. and Oterkus, S., 2018. Peridynamic modelling of fracture in marine lithium-ion batteries.*Ocean Engineering*, *151*, pp.257-267.

Wang, H., Oterkus, E. and Oterkus, S., 2018. Predicting fracture evolution during lithiation process using peridynamics. *Engineering Fracture Mechanics*, *192*, pp.176-191.

Wang, H., Oterkus, E. and Oterkus, S., 2018. Three-Dimensional Peridynamic Model for Predicting Fracture Evolution during the Lithiation Process. *Energies*, *11*(6), pp.1-22.

- **Presentations and other publications**

Wang, H. and Oterkus, E., 2015, Failure Analysis of Marine Lithium-Ion Batteries by Using Peridynamics, *Shipping in Changing Climates Conference*, Glasgow, UK.

Wang, H., Oterkus, E. and Oterkus, S., 2016, Fracture Modelling of Marine Lithium-Ion Batteries by Using Peridynamics, *ASME 2016 International Mechanical Engineering Congress & Exposition*, Phoenix, AZ, USA.

Wang, H. and Oterkus, E., 2017, Failure Analysis of Porous Solid Oxide Fuel Cells by Using Peridynamics, *ASME 2017 International Mechanical Engineering Congress & Exposition*, Tampa, FL, USA.

8.6 Final remarks

The nonlocal spatial integral equations of PD have brought significant advantages in fracture analysis as compared with conventional methods in fracture analysis. With these advantages, PD can be applied in the numerical simulation of marine batteries. The numerical results shown in this thesis have supported and validated the accuracy,

capability and reliability of PD. It has also shown the efficiency of PD in fracture analysis. Therefore the numerical models in this thesis can be helpful in the fracture analysis of both single field and coupled field problems.

9 References

[1] J. Herdzik, “Emissions from marine engines versus IMO certification and requirements of tier 3.,” *J. KONES*, vol. 18, pp. 161–167, 2011.

[2] C. Rayment and S. Sherwin, *Introduction to fuel cell technology*. 2003.

[3] A. K. & ASSOCIATES, “Marine Power: XeroPoint Hybrid Propulsion.” [Online]. Available: http://www.aka-group.com/marine-power/xeropoint-hybrid-propulsion. [Accessed: 21-Jul-2018].

[4] T. J. Dougherty, W. P. Segall, and M. E. Iverson, “Battery System,” 6452361, 2002.

[5] C. Rosenkranz, “Deep-cycle batteries for plug-in hybrid application.,” in *EVS20 Plug-in Hybrid Vehicle Workshop*, 2003.

[6] S. Y. Chung, J. T. Bloking, and Y. M. Chiang, “Electronically conductive phospho-olivines as lithium storage electrodes,” *Nat. Mater.*, vol. 1, no. 2, pp. 123–128, 2002.

[7] Z. Zhou, M. Benbouzid, J. F. Charpentier, F. Scuiller, and T. Tang, “A review of energy storage technologies for marine current energy systems.,” *Renew. Sustain. Energy Rev.*, vol. 18, pp. 390–400, 2013.

[8] C. Daniel, “Materials and processing for lithium-ion batteries.,” *JOM*, vol. 60, no. 9, pp. 43–48, 2008.

[9] R. Grantab and V. B. Shenoy, “Pressure-gradient dependent diffusion and crack propagation in lithiated silicon nanowires.,” *J. Electrochem. Soc.*, vol. 159, no. 5, pp. A584–A591, 2012.

[10] N. Laosiripojana, W. Wiyaratn, W. Kiatkittipong, A. Arpornwichanop, A. Soottitantawat, and S. Assabumrungrat, “Reviews on solid oxide fuel cell technology.,” *Eng. J. (Eng. J.)*, vol. 13, no. 1, pp. 65–84, 2009.

[11] V. Dusastre and J. A. Kilner, “Optimisation of composite cathodes for intermediate temperature SOFC applications.,” *Solid State Ionics*, vol. 126, no. 1–2, pp. 163–174, 1999.

[12] S. Celik, B. Ibrahimoglu, M. D. Mat, Y. Kaplan, and T. N. Veziroglu, “Micro level two dimensional stress and thermal analysis anode/electrolyte interface of a solid oxide fuel cell.,” *Int. J. Hydrogen Energy*, vol. 40, no. 24, pp. 7895–7902, 2015.

[13] D. Papurello, A. Lanzini, D. Drago, P. Leone, and M. Santarelli, “Limiting factors for planar solid oxide fuel cells under different trace compound concentrations.,” *Energy*, vol. 95, pp. 67–78, 2016.

[14] P. Aguiar, N. Lapena-Rey, D. Chadwick, and L. Kershenbaum, “Improving catalyst structures and reactor configurations for autothermal reaction systems: application to solid oxide fuel cells.,” *Chem. Eng. Sci.*, vol. 56, no. 2, pp. 651–658, 2001.

[15] D. Papurello, A. Lanzini, S. Fiorilli, F. Smeacetto, R. Singh, and M. Santarelli, “Sulfur poisoning in Ni-anode solid oxide fuel cells (SOFCs): deactivation in single cells and a stack.,” *Chem. Eng. J.*, vol. 283, pp. 1224–1233, 2016.

[16] D. Papurello, A. Lanzini, P. Leone, and M. Santarelli, “The effect of heavy tars (toluene and naphthalene) on the electrochemical performance of an anode-supported SOFC running on bio-syngas.,” *Renew. Energy*, vol. 99, pp. 747–753, 2016.

[17] H. Madi, A. Lanzini, D. Papurello, S. Diethelm, C. Ludwig, and M. Santarelli, “Solid oxide fuel cell anode degradation by the effect of hydrogen chloride in stack and single cell environments.,” *J. Power Sources*, vol. 326, pp. 349–356, 2016.

[18] H. Wang, E. Oterkus, S. Celik, and S. Toros, “Thermomechanical analysis of porous solid oxide fuel cell by using peridynamics.,” *AIMS Energy*, vol. 5, no. 4, pp. 585–600, 2017.

[19] S. A. Silling and E. Askari, “A meshfree method based on the peridynamic model of solid mechanics,” *Comput. Struct.*, vol. 83, no. 17, pp. 1526–1535, 2005.

[20] J. R. Rice, *Solid Mechanics*. Cambridge: Harvard University, 2010.

[21] H. M. Westergaard, “Bearing pressures and cracks,” *J. Appl. Mech.*, vol. 6, no. 2, pp. A49–A53, 1939.

[22] M. L. Williams, “On the stress distribution at the base of a stationary crack,” *J. Appl. Mech.*, vol. 24, no. 1, pp. 109–114, 1956.

[23] R. D. Cook, D. S. Malkus, and M. E. Plesha, *Concepts and applications of finite element method*. New York: John Willey and Sons, 1989.

[24] T. L. Anderson, *Fracture mechanics: fundamentals and applications*. CRC press, 2017.

[25] A. Hillerborg, M. Modéer, and P. E. Petersson, “Analysis of crack formation and crack growth in concrete by means of fracture mechanics and finite elements.,” *Cem. Concr. Res.*, vol. 6, no. 6, pp. 773–781, 1976.

[26] C. E. Inglis, “Stresses in a plate due to the presence of cracks and sharp corners.,” *Spie Milestone Ser. MS*, vol. 137, pp. 3–17, 1997.

[27] G. R. Irwin, “Analysis of stresses and strains near the end of a crack traversing a plate.,” *J. appl. Mech*, 1957.

[28] A. A. Griffith and M. Eng, “The phenomena of rupture and flow in solids.,” *Philos. Trans. R. Soc. London. Ser. A, Contain. Pap. a Math. or Phys. Character*, vol. 221, no. 582–593, pp. 163–198, 1921.

[29] R. J. Sanford, *Principles of fracture mechanics*. Upper Saddle River, NJ: Prentice Hall., 2003.

[30] J. R. Rice, “A path independent integral and the approximate analysis of strain concentration by notches and cracks.,” *J. Appl. Mech.*, vol. 35, no. 2, pp. 379–386, 1968.

[31] E. Madenci and E. Oterkus, *Peridynamic theory and its applications*. Springer, 2016.

[32] A. Trädegård, F. Nilsson, and S. Östlund, "FEM-remeshing technique applied to crack growth problems.," *Comput. Methods Appl. Mech. Eng.*, vol. 160, no. 1–2, pp. 115–131, 1998.

[33] J. M. Melenk and I. Babuška, "The partition of unity finite element method: basic theory and applications.," *Comput. Methods Appl. Mech. Eng.*, vol. 139, no. 1–4, pp. 289–314, 1996.

[34] T. P. Fries and A. Zilian, "On time integration in the XFEM.," *Int. J. Numer. Methods Eng.*, vol. 79, no. 1, pp. 69–93, 2009.

[35] T. Belytschko, H. Chen, J. Xu, and G. Zi, "Dynamic crack propagation based on loss of hyperbolicity and a new discontinuous enrichment.," *Int. J. Numer. Methods Eng.*, vol. 58, no. 12, pp. 1873–1905, 2003.

[36] M. H. Aliabadi and D. P. Rooke, *Numerical fracture mechanics (Vol. 8)*. Springer Science & Business Media, 1991.

[37] F. J. Rizzo, "An integral equation approach to boundary value problems of classical elastostatics," *Q. Appl. Math.*, vol. 25, no. 1, pp. 83–95, 1967.

[38] A. Bobet, "Numerical methods in geomechanics," *Arab. J. Sci. Eng.*, vol. 35, no. 1B, pp. 27–48, 2010.

[39] H. Antes, "A Short Course on Boundary Element Methods." [Online]. Available: http://www.sci.utah.edu/~macleod/links/bem-shortcourse.pdf. [Accessed: 07-May-2018].

[40] O. Von Estorff and M. Firuziaan, "Coupled BEM/FEM approach for nonlinear soil/structure interaction.," *Eng. Anal. Bound. Elem.*, vol. 24, no. 10, pp. 715–725, 2000.

[41] D. S. Jr, O. V. Estorff, and W. J. Mansur, "Interative coupling of BEM and FEM for nonlinear dynamic analyses.," *Comput. Mech.*, vol. 34, no. 1, pp. 67–73, 2004.

[42] W. M. Elleithy and M. Tanaka, “Interface relaxation algorithms for BEM-BEM coupling and FEM-BEM coupling.,” *Comput. Methods Appl. Mech. Eng.*, vol. 192, no. 26, pp. 2977–2992, 2003.

[43] M. H. Aliabadi, “Boundary element formulations in fracture mechanics.,” *Appl. Mech. Rev.*, vol. 50, pp. 83–96, 1997.

[44] G. I. Barenblatt, “The mathematical theory of equilibrium cracks in brittle fracture,” *Adv. Appl. Mech.*, vol. 7, pp. 55–129, 1962.

[45] G. I. Barenblatt, “The formation of equilibrium cracks during brittle fracture. General ideas and hypotheses. Axially-symmetirc cracks,” *J. Appl. Math. Mech.*, vol. 23, no. 3, pp. 622–636, 1959.

[46] D. S. Dugdale, “Yielding of steel sheets containing slits,” *J. Mech. Phys. Solids*, vol. 8, no. 2, pp. 100–104, 1960.

[47] J. G. Williams and H. Hadavinia, “Analytical solutions for cohesive zone models,” *J. Mech. Phys. Solids*, vol. 50, no. 4, pp. 809–825, 2002.

[48] Z. H. Jin and C. T. Sun, “A comparison of cohesive zone modelling and classical fracture mechanics based on near tip stress field,” *Int. J. Solids Struct.*, vol. 43, no. 5, pp. 1047–1060, 2006.

[49] X. P. Xu and A. Needleman, “Numerical simulations of fast crack growth in brittle solids,” *J. Mech. Phys. Solids*, vol. 42, no. 9, pp. 1397–1434, 1994.

[50] P. A. Klein, J. W. Foulk, E. P. Chen, S. A. Wimmer, and H. J. Gao, “Physics-based modeling of brittle fracture: cohesive formulations and the application of meshfree methods,” *Theor. Appl. Fract. Mech.*, vol. 37, no. 1, pp. 99–166, 2001.

[51] S. Oterkus, E. Madenci, and A. Agwai, “Fully coupled peridynamic thermomechanics,” *J. Mech. Phys. Solids*, vol. 64, pp. 1–23, 2014.

[52] B. Kilic and E. Madenci, “Peridynamic theory for thermomechanical analysis,” *IEEE Trans. Adv. Packag.*, vol. 33, no. 1, pp. 97–105, 2010.

[53] Z. Chen and F. Bobaru, “Peridynamic modelling of pitting corrosion damage,” *J. Mech. Phys. Solids*, vol. 78, pp. 352–381, 2015.

[54] F. Bobaru and M. Duangpanya, “The peridynamic formulation for transient heat conduction,” *Int. J. Heat Mass Transf.*, vol. 53, no. 19, pp. 4047–4059, 2010.

[55] S. Toros, “Microstructural finite element modeling of redox behavior of Ni–YSZ based ceramic SOFC anodes,” *Ceram. Int.*, vol. 42, no. 7, pp. 8915–8924, 2016.

[56] S. Celik, B. Ibrahimoglu, S. Toros, and M. D. Mat, “Three dimensional stress analysis of solid oxide fuel cell anode micro structure,” *Int. J. Hydrogen Energy*, vol. 39, no. 33, pp. 19119–19131, 2014.

[57] B. Timurkutluk and M. D. Mat, “Effects of anode fabrication parameters on the performance and redox behaviour of solid oxide fuel cells,” *J. Power Sources*, vol. 258, pp. 108–116, 2014.

[58] B. Timurkutluk and M. D. Mat, “A Performance Prediction Tool for Solid Oxide Fuel Cells after Single Redox Cycle,” *Fuel Cells*, vol. 15, no. 1, pp. 71–89, 2015.

[59] D. Sarantaridis and A. Atkinson, “Redox Cycling of Ni‐Based Solid Oxide Fuel Cell Anodes: A Review,” *Fuel cells*, vol. 7, no. 3, pp. 246–258, 2007.

[60] J. Laurencin, G. Delette, M. Dupeux, and F. Lefebvre-Joud, “A numerical approach to predict the SOFC fracture: The case of an anode supported cell,” *ECS Trans.*, vol. 7, no. 1, pp. 677–686, 2007.

[61] J. Laurencin, G. Delette, F. Lefebvre-Joud, and M. Dupeux, “A numerical tool to estimate SOFC mechanical degradation: case of the planar cell configuration,” *J. Eur. Ceram. Soc.*, vol. 28, no. 9, pp. 1857–1869, 2008.

[62] A. B. Stambouli and E. Traversa, “Solid oxide fuel cells (SOFCs): a review of an environmentally clean and efficient source of energy,” *Renew. Sustain. energy Rev.*, vol. 6, no. 5, pp. 433–455, 2002.

[63] D. Papurello, A. Lanzini, L. Tognana, S. Silvestri, and M. Santarelli, “Waste to energy: Exploitation of biogas from organic waste in a 500 Wel solid oxide fuel cell (SOFC) stack,” *Energy*, vol. 85, pp. 145–158, 2015.

[64] S. Giraud and J. Canel, “Young’s modulus of some SOFCs materials as a function of temperature,” *J. Eur. Ceram. Soc.*, vol. 28, no. 1, pp. 77–83, 2008.

[65] M. Pihlatie, A. Kaiser, and M. Mogensen, “Mechanical properties of NiO/Ni–YSZ composites depending on temperature, porosity and redox cycling,” *J. Eur. Ceram. Soc.*, vol. 29, no. 9, pp. 1657–1664, 2009.

[66] C. K. Chan *et al.*, “High-performance lithium battery anodes using silicon nanowires,” *Nat. Nanotechnol.*, vol. 3, no. 1, pp. 31–35, 2008.

[67] J. P. Maranchi, A. F. Hepp, and P. N. Kumta, “High capacity, reversible silicon thin-film anodes for lithium-ion batteries,” *Electrochem. solid-state Lett.*, vol. 6, no. 9, pp. A198–A201, 2003.

[68] I. Ryu, J. W. Choi, Y. Cui, and W. D. Nix, “Size-dependent fracture of Si nanowire battery anodes,” *J. Mech. Phys. Solids*, vol. 59, no. 9, pp. 1717–1730, 2011.

[69] P. Liu, N. Sridhar, and Y. W. Zhang, “Lithiation-induced tensile stress and surface cracking in silicon thin film anode for rechargeable lithium battery,” *J. Appl. Phys.*, vol. 112, no. 9, p. 093507, 2012.

[70] M. A. Stamps and H. Y. S. Huang, “Mixed modes fracture and fatigue evaluation for lithium-ion batteries,” in *ASME 2012 International Mechanical Engineering Congress and Exposition*, 2012, pp. 97–103.

[71] P. Zuo and Y. P. Zhao, “A phase field model coupling lithium diffusion and stress evolution with crack propagation and application in lithium ion batteries,” *Phys. Chem. Chem. Phys.*, vol. 17, no. 1, pp. 287–297, 2015.

[72] Y. F. Gao and M. Zhou, “Coupled mechano-diffusional driving forces for fracture in electrode materials,” *J. Power Sources*, vol. 230, pp. 176–193, 2013.

[73] S. Gopalakrishnan and S. Narendar, “Wave propagation in nanostructures,” in *Nanoscience and technology*, 2013, pp. 59–70.

[74] J. N. Reddy, *An introduction to continuum mechanics*. Cambridge university press, 2013.

[75] A. C. Eringen and D. G. B. Edelen, “On nonlocal elasticity,” *Int. J. Eng. Sci.*, vol. 10, no. 3, pp. 233–248, 1972.

[76] A. C. Eringen, “Nonlocal polar elastic continua,” *Int. J. Eng. Sci.*, vol. 10, no. 1, pp. 1–16, 1972.

[77] A. C. Eringen, “Linear theory of nonlocal elasticity and dispersion of plane waves,” *Int. J. Eng. Sci.*, vol. 1, no. 4, pp. 425–435, 1972.

[78] A. C. Eringen and B. S. Kim, “Stress concentration at the tip of crack,” *Mech. Res. Commun.*, vol. 1, no. 4, pp. 233–237, 1974.

[79] G. R. Irwin, J. A. Kies, and H. L. Smith, “Fracture strengths relative to onset and arrest of crack propagation,” in *Proc. ASTM*, 1958, pp. 640–657.

[80] P. S. Valvo, “A revised virtual crack closure technique for physically consistent fracture mode partitioning,” *Int. J. Fract.*, vol. 173, no. 1, pp. 1–20, 2012.

[81] L. E. Malvern, *Introduction to the Mechanics of a Continuous Medium*, No. Monogr. 1969.

[82] E. Madenci, “Peridynamic integrals for strain invariants of homogeneous deformation,” *ZAMM - Journal Appl. Math. Mech. für Angew. Math. und Mech.*, vol. 97, no. 10, pp. 1236–1251, 2017.

[83] R. SS, *Mechanical vibrations*, 4th ed. Pearson Prentice Hall, Upper Saddle River, 2004.

[84] L. Lapidus and G. F. Pinder, *Numerical solution of partial differential equations in science and engineering*. John Willey and Sons, 2011.

[85] B. Kilic and E. Madenci, “An adaptive dynamic relaxation method for quasi-static simulations using the peridynamic theory,” *Theor. Appl. Fract. Mech.*, vol. 53, no. 194–204, 2010.

[86] P. Underwood, “Dynamic relaxation. Computational Methods for Transient Dynamic Analysis,” 1983.

[87] E. Madenci, A. Barut, and M. Futch, “Peridynamic differential operator and its applications,” *Comput. Methods Appl. Mech. Eng.*, vol. 304, pp. 408–451, 2016.

[88] L. J. Blomen and M. N. eds. Mugerwa, *Fuel cell systems*. Springer Science & Business Media, 2013.

[89] W. R. Grove, “On voltaic series and the combination of gases by platinum,” *Philos. Mag. Ser. 3*, vol. 14, no. 86–87, pp. 123–130, 1839.

[90] Nernst，W, “Verfahren zur Erzeugung von elektrischem Glühlicht,” *DRP*, vol. 104, p. 872, 1899.

[91] F. Haber, “Verfahren zur Erzeugung von elektrischer Energie aus Kohle und gasformigen Brennstoffen,” *OÈster Pat*, vol. 27, p. 743, 1907.

[92] H. A. Laitinen and B. B. Bhatia, “Electrochemical Study of Metallic Oxides in Fused Lithium Chloride‐Potassium Chloride Eutectic,” *J. Electrochem. Soc.*, vol. 107, no. 8, pp. 705–710, 1960.

[93] S. C. Singhal and K. eds Kendall, *High-temperature solid oxide fuel cells: fundamentals, design and applications*. Elsevier, 2003.

[94] K. Kiukkola and C. Wagner, “Measurements on galvanic cells involving solid electrolytes,” *J. Electrochem. Soc.*, vol. 104, no. 6, pp. 379–387, 1957.

[95] H. Peters and G. Mann, “Elektrochemische Untersuchung des Gleichgewichtes Fe+ CO2⇄ FeO+ CO,” *Zeitschrift für Elektrochemie, Berichte der Bunsengesellschaft für Phys. Chemie*, vol. 63, no. 2, pp. 244–248, 1959.

[96] H. H. Möbius, “On the history of solid electrolyte fuel cells,” *J. solid state Electrochem.*, vol. 1, no. 1, pp. 2–16, 1997.

[97] A. B. Stambouli and E. Traversa, “Fuel cells, an alternative to standard sources of energy,” *Renew. Sustain. Energy Rev.*, vol. 6, no. 3, pp. 295–304, 2002.

[98] E. Ivers-Tiffée, A. Weber, and D. Herbstritt, “Materials and technologies for SOFC-components,” *J. Eur. Ceram. Soc.*, vol. 21, no. 10, pp. 1905–1811, 2001.

[99] P. R. Shearing, J. Gelb, and N. P. Brandon, “X-ray nano computerised tomography of SOFC electrodes using a focused ion beam sample-preparation technique,” *J. Eur. Ceram. Soc.*, vol. 30, no. 8, pp. 1809–1814, 2010.

[100] U. Kasavajjula, C. Wang, and A. J. Appleby, “Nano-and bulk-silicon-based insertion anodes for lithium-ion secondary cells,” *J. Power Sources*, vol. 163, no. 2, pp. 1003–1039, 2007.

[101] R. A. Huggins, “Lithium alloy negative electrodes,” *J. Power Sources*, vol. 81, pp. 13–19, 1999.

[102] X. Zhang, S. W. Lee, H. W. Lee, Y. Cui, and C. Linder, “A reaction-controlled diffusion model for the lithiation of silicon in lithium-ion batteries,” *Extrem. Mech. Lett.*, vol. 4, pp. 61–75, 2015.

[103] A. Fick, “On liquid diffusion,” *J. Memb. Sci.*, vol. 100, no. 1, pp. 33–38, 1995.

[104] V. B. Shenoy, P. Johari, and Y. Qi, “Elastic softening of amorphous and crystalline Li–Si phases with increasing Li concentration: a first-principles study,” *J. Power Sources*, vol. 195, no. 19, pp. 6825–6830, 2010.

[105] J. Li, A. K. Dozier, Y. Li, F. Yang, and Y. T. Cheng, “Crack pattern formation in thin film lithium-ion battery electrodes,” *J. Electrochem. Soc.*, vol. 158, no. 6, pp. A689–A694, 2011.

[106] C. De las Casas and W. Li, “A review of application of carbon nanotubes for lithium ion battery anode material,” *J. Power Sources*, vol. 208, pp. 74–85, 2012.

[107] W. J. Zhang, “A review of the electrochemical performance of alloy anodes for lithium-ion batteries,” *J. Power Sources*, vol. 196, no. 1, pp. 13–24, 2011.

[108] S. P. Nadimpalli, R. Tripuraneni, and V. A. Sethuraman, “Real-time stress measurements in germanium thin film electrodes during electrochemical Lithiation/Delithiation cycling,” *J. Electrochem. Soc.*, vol. 162, no. 14, pp. A2840–A2846, 2015.

[109] J. G. Ren, Q. H. Wu, H. Tang, G. Hong, W. Zhang, and S. T. Lee, “Germanium–graphene composite anode for high-energy lithium batteries with long cycle life,” *J. Mater. Chem. A*, vol. 1, no. 5, pp. 1821–1826, 2013.

[110] B. Gao *et al.*, “Electrochemical intercalation of single-walled carbon nanotubes with lithium,” *Chem. Phys. Lett.*, vol. 307, no. 3–4, pp. 153–157, 1999.

[111] J. H. Lee, B. S. Kong, S. B. Yang, and H. T. Jung, “Fabrication of single-walled carbon nanotube/tin nanoparticle composites by electrochemical reduction combined with vacuum filtration and hybrid co-filtration for high-performance lithium battery electrodes,” *J. Power Sources*, vol. 194, no. 1, pp. 520–525, 2009.

[112] J. Yan, H. Song, S. Yang, J. Yan, and X. Chen, “Preparation and electrochemical properties of composites of carbon nanotubes loaded with Ag and TiO2 nanoparticle for use as anode material in lithium-ion batteries,” *Electrochim. Acta*, vol. 53, no. 22, pp. 6351–6355, 2008.

[113] H. Wang, E. Oterkus, and S. Oterkus, “Peridynamic modelling of fracture in marine lithium-ion batteries,” *Ocean Eng.*, vol. 151, pp. 257–267, 2018.

[114] A. F. Bower, P. R. Guduru, and V. A. Sethuraman, “A finite strain model of stress, diffusion, plastic flow, and electrochemical reactions in a lithium-ion half-cell,” *J. Mech. Phys. Solids*, vol. 59, no. 4, pp. 804–828, 2011.

[115] H. Wang, E. Oterkus, and S. Oterkus, “Predicting fracture evolution during lithiation process using peridynamics,” *Eng. Fract. Mech.*, vol. 192, pp. 176–191, 2018.